ANALYSIS AND CONTROL OF NONHOLONOMIC SYSTEMS UNDER DYNAMICAL CONSTRAINTS

動力学的束縛を受ける非ホロノミック系の解析と制御

TAKAHIRO SUZUKI

鈴木貴宏

Analysis and Control of Nonholonomic Systems under Dynamical Constraints

by

Takahiro Suzuki

A Dissertation Presented to the
GRADUATE SCHOOL
THE UNIVERSITY OF TOKYO
for the Degree of
Doctor of Enginnering
(Department of Mechano-Informatics)

December 19, 1997

Acknowledgments

This research started with the supervision of Professor Yoshihiko Nakamura as one of his farsighted research themes of nonholonomy in my preparation for undergraduate degree in 1992. He has been patiently succeeding kind-hearted guidance and detailed review for the whole of my researches, papers, and theses in his exceedingly busy days. I wouldn't have gone through this research without his support in the Yoshimoto-Nakamura Laboratory, Department of Mechano-Informatics, University of Tokyo. I would like to express my deepest gratitude to him.

I would also like to return my great thanks to Professor Ken'ichi Yoshimoto. His kind and considerable advice and stimulating discussions have provided me with many valuable suggestions. I was able to spend a comfortable research life in this laboratory by virtue of him.

I have to greatly thank Mr. Masabumi Koinuma. His deep insight of nonlinear dynamics and collaboration as a co-researcher and a co-author were indispensable to complete my work.

I wish to thank Mr. Woojin Chung. He always helped me by his opportune and advantageous discussions and friendship when I was driven into the corner. I also wish to thank Dr. Masafumi Okada for his helpful advice from control viewpoint, Mr. Ryuji Iwamoto for his pioneering work for control of free-joint manipulators and helpful development of the experimental prototype of 2R-FJM, and Mr. Wataru Miyoshi for his generous assistance in the experiments of 3R-FJM.

I would like to express my sincere thanks to my parents Hajime and Keiko Suzuki who gave me all support and opportunity in my life. Finally, I am especially grateful to my wife Yurika and my son Harutaka for their helps and encouragements. They have been a source of all my love and strength.

Contents

Abstract

Mechanical systems whose dynamical constraints are nonintegrable, thus, nonholonomic show strong nonlinearity. Such systems are difficult to control since linearization methods, such as feedback linearization, cannot be applied. Such nonlinearity often originates from underactuatedness and shows chaotic complexity and diversity. In this dissertation, nonlinear behaviors of such systems are to be analyzed. Control methods utilizing the nonlinearity are to be constructed. The fundamental motivation of thos work is a desire to define a new nonlinear mechanism with unprecedented characteristics such as underactuatedness, complexity and diversity.

There are two major classes of nonholonomic mechanisms under dynamical constraints. One is that of first-order nonholonomic systems whose dynamical constraints have the first integrals. The issues of space robots are to be discussed as problems of a first-order nonholonomic system. The rest of discussions in this dissertation is on second-order nonholonomic systems whose constraints have no integral. Analysis and control of free-joint manipulators are to be discussed as a second-order nonholonomic system.

The "spiral motion of space robots" is a method of motion planning which approximately realize an infeasible desired trajectory under nonholonomic constraints by a feasible spiral-like trajectory circulating around the desired trajectory. It simplifies motion planning of space nonholonomic systems. The validity of spiral motions is to be verified by computer simulations.

Free-joint manipulators have a potentiality to steer many joints only by one motor. The behaviors in response to a periodic input vary from a family of closed trajectories to chaotic motion depending upon the amplitude of the input. Methods of analysis and control of the systems are first heuristically investigated and constructed from observations of computer simulations. They are subsequently approximated and formulated by the averaging method for generalization to higher dimensional systems. The effectiveness of the proposed control methods is verified by simulations and experiments.

Chapter 1

Introduction

1.1 Motivation: Dynamical Nonlinearity and Minimalism of Mechanisms

There are kinds of mastery performances such as juggling, stunts, acrobatics, and so on. Such motions cannot be performed by ordinary people but can be achieved only by dexterous and experienced jugglers, acrobats and tumblers. What makes the acrobatic motions so difficult? The major reasons are dynamic nonlinearity of motions and limitation of manipulation or actuation where the performer requires to steer many objects or complex motions in a space of high dimensions. The motions involve rotations in three-dimensional space which contain topological and dynamical nonlinearity.

Topological nonlinearity is due to non-Euclidean coordinate space of three-dimensional rotations. It makes our insights of the motions difficult since we usually grasp natural phenomena in two dimensional Cartesian or Euclidean space on a paper, screen or blackboard. However, topological nonlinearity does not originate from dynamics but from static geometry. The issues of topological nonlinearity have been discussed by many researchers as kinematic nonholonomy. On the other hand, dynamical nonlinearity arises from nonholonomy of dynamics in conjunction with underactuatedness of mechanisms. Underactuatedness implies that fewer actuators drive larger numbers of coordinates. Underactuatedness makes it difficult to control motions but reduces the number of actuators and simplify the mechanism. Namely, dynamical nonlinearity is closely connected to minimalism of the mechanisms performing the motion. Dynamical nonlinearity is to be mainly focused on in this dissertation.

As the study of such nonlinearity, many researchers have investigated nonholonomic systems and underactuated mechanisms. Although many general theories and methods for nonholonomic systems were proposed and established by control

engineers, it is still difficult to deal with those kinds of nonlinearities. We will categorize the nonlinearities from a control viewpoint.

Holonomic robots are usually nonlinear but can be transformed into controllable linear systems by linearization methods, for instance, feedback linearization. Such a nonlinearity is exactly linearizable. This can be considered a "weak nonlinearity" since what appears as nonlinearity is essentially a linear phenomenon. First-order nonholonomic systems have a stronger nonlinearity which is not exactly linearizable but controllable. The controllability is theoretically proved from local controllability conditions. They are not stabilizable by a smooth time-invariant feedback control to an equilibrium point but are stabilizable by a discontinuous or time-variant feedback control. The nonlinearity of second-order nonholonomic systems is often much stronger since its controllability cannot be proved from local controllability conditions, such as Sussmann's conditions. They are neither stabilizable by smooth static feedback control. However, the conditions which they don't satisfy are just sufficient conditions. They usually have accessibility and are possible to be locally or globally controllable. In this sense, control theories and methods are useful for well-structured problem, but are unfortunately powerless for the systems with stronger nonlinearity. Dynamical nonlinear systems are often second-order nonholonomic and have higher underactuatedness. This dissertation aims to analyze the nonlinear behaviors of dynamical nonholonomic systems and to propose some approaches to control such strongly nonlinear systems from a viewpoint of nonlinear dynamics, and to define a minimal mechanism with potentiality to control many dimensions by less actuators.

The motivation of this research is triple-fold: The first is to device the analysis of nonlinear dynamic motions of nonholonomic mechanical systems. Formulation of variation of the satellite orientation with cyclic motions of the end-effector in Chap.3 and behavioral analysis of free-joint manipulators in response to a periodic input in Chaps.4, 5 and 6 are shown as the examples of nonlinear dynamical analysis in this dissertation. The second is to develop and formulate new methods to control dynamic motions of nonholonomic mechanical systems. The "spiral motion" in Chap.3 and "amplitude modulation of a periodic input" in Chaps.4, 5 and 6 are proposed as examples of the new control methods in this dissertation. The third is to define and construct new mechanisms through deep insights of nonlinearity in dynamics and control. Free-joint manipulators with only one motor in Chaps.5 and 6 are proposed as examples of the new mechanisms in this dissertation.

The characteristic of this dissertation is to deal with nonlinear problems of nonholonomy using various tools in nonlinear dynamics, kinematics and nonlinear control, such as quaternion kinematics, differential forms in Chap.3, phase space

analysis and Poincaré map analysis in Chap.4, averaging analysis and Hamiltonian analysis in Chaps.5 and 6, etc. are applied in this dissertation.

1.2 Chaos in Hamiltonian Systems

Chaos is attracting great interests of researchers in various fields, for instance, nonlinear dynamics, mathematics, neurophysiology, economics, and robotics. Especially, there were many researches on nonlinear dynamics and control of Hamiltonian conserved systems and perturbed systems [Tab89, KS92, Wig90, Far94, OGY90, SGOY93, LDG93, BKG+95, CD93b, CD93a, HJ93]. Hamiltonian systems generally include most of mechanical systems as an example of Hamiltonian conserved mechanical systems, motions of forced pendulums are often investigated. Free-joint manipulators are similar to pendulums except existence of the potential term and are also proved to be Hamiltonian conserved systems as in Chaps.4, 5 and 6. We take an advantage of the approaches and methods in nonlinear dynamics and chaos since there are a few theories or methods for second-order nonholonomic systems in the control literature. In Chaps.4, 5 and 6, the methods and theories in chaos and nonlinear dynamics, e.g. analysis in the phase space and the Poincaré map, averaging analysis and the Hamiltonian analysis, are applied. Furthermore, chaotic behaviors of free-joint manipulators under a sufficiently large perturbation are presented in Sec.4.3.3. It is a typical example that a simple mechanical system shows a complex behavior or, in other words, a nonholonomic mechanism becomes chaotic.

1.3 Goals of this Dissertation and the Composition of Chapters

This dissertation aims to attain three goals. The first goal is to clarify intricate and multifarious behaviors of simple nonlinear mechanical systems and to establish methods to analyze these nonlinear behaviors. The second goal is to construct simple path-planning and control strategies for robots with nonholonomic constraints. The final goal is to define a new advantageous mechanisms. The new mechanism is defined and developed based on the dynamical and control standpoints. In order to attain the purposes, various theories and methods in nonlinear dynamics and chaos are applied.

The rest of this dissertation is composed by six chapters. In Chap.2, definition of nonholonomy, history of nonholonomic research, and important theorems for nonholonomic systems are summarized.

In Chap.3, motion planning of free-flying space robots is to be discussed. Free-flying space robots are dynamical systems under first-order nonholonomic constraints of the angular momentum conservation. An arbitrary path of the end-effector and base-orientation is infeasible only by arm motions due to nonholonomic constraints. The *spiral motion* is the feasible motion which approximately achieves it. It consists of a nominal motion and a cyclic motion. A nominal motion follows the given end-effector path without considering the base-orientation. A cyclic motion compensates the deviation of base-orientation produced as a side effect of the nominal motion. The cyclic motion acts as a perturbation and can restrict its magnitude within an arbitrary desired limit. The effect of a cyclic motion is formulated and computation algorithm to obtain an optimal spiral motion is presented. Computer simulations verify the effectiveness of the proposed methods. One of the merits of this strategy is that the resultant motion follows the nominal motion with a given bound of approximation. The other merit is that holonomic path-planning strategies can be applied to design the nominal motion, which makes nonholonomic path-planning simpler and easier.

In Chap.4, nonlinear dynamical analysis of 2R free-joint manipulator (2R-FJM) is to be investigated and its control strategy is to be developed. The 2R-FJM is a simplest example of second-order nonholonomic systems. Its nonlinear behavior with periodic input is investigated on the Poincaré map. Chaotic behavior is revealed when being subjected by a sufficiently large input-amplitude. Control methods of the 2R-FJM are discussed in the subsequent sections. After explaining difficulty to prove its controllability and stabilizability by conventional control theories, a control strategy of simultaneous positioning of the both joints by periodic perturbation to the first joint is proposed. The control method proposed in the chapter is heuristically constructed from analysis of its nonlinear behavior. In order to verify the effectiveness of the method, simulations and experiments are carried out.

Subsequently to Chap.4, mathematical analysis of 2R-FJM via the averaging method is to be investigated in Chap.5. The averaging method is an analytical approximation which guarantees the error boundedness by the order of input-amplitude. The averaging analysis shows that the averaged system is confined onto an invariant torus manifold in the phase space. The invariant manifold is identified by a Hamiltonian and, thus, the averaged dynamics is shown to be a conserved system. Two control methods to steer the system to a desired invariant manifold using the Hamiltonian are developed. A termination control at the destination are also developed from second-order averaging. The effectiveness of the proposed control methods is verified by simulations and experiments.

			exact linearization	local controllability	accessibility	example	In this dissertation
holonomic			OK	OK	OK	"ordinary" robot	
nonholonomic	1st-order	kinematic	NO	OK	OK	car-like robot	
		dynamic				space robot	Chap.3
	2nd-order		NO	NO	OK	free-joint manipulator	Chap.4-6

Figure 1.1: Categorization of systems by nonholonomy

In Chap.6, nonlinear behavior of 3R-FJM with one motor is to be analyzed via the averaging method. The averaged behavior with a constant input-amplitude is shown to be confined onto a two-dimensional torus invariant manifold and, then, the system has two conserved quantities. One is found to be a Hamiltonian defined from the Lagrangian of the averaged system via similar consideration for 2R-FJM. Although the other hasn't been found yet and the corresponding manifold to a destination cannot be identified, the amplitude modulation control is applied to stabilize the Hamiltonian to a desired value. When the Hamiltonian is stabilized to a desired value, the input-amplitude becomes constant and the system is stabilized onto a two-dimensional invariant manifold. Experiments for 3R-FJM are also carried out to show the practical behavior and to verify the effectiveness of the proposed method.

Chapter 7 concludes the whole discussions made in this dissertation and provides some remarks and prospects. Figure 1.1 illustrates the categorization of systems by nonholonomy, the relations to control properties, and the correspondences with the chapters in this dissertation.

Chapter 2

Nonholonomic Systems

2.1 Underactuated Systems and Nonholonomic Systems

Underactuated mechanisms have been attracting a great deal of research interests in robotics and control as a field with many new possibilities [BG+96]. *Underactuatedness* means that a system is driven or steered by less number of actuators than the dimension of configuration space of the system. Underactuatedness is strongly related to *nonholonomy*.

The constraints of a system are called *holonomic* [Gol80] if they can be represented by equations only of generalized coordinates* and a time as:

$$\boldsymbol{h}(\boldsymbol{q}, t) = \mathbf{o} \tag{2.1}$$

where $\boldsymbol{q}$ denote generalized coordinates. The *degree-of-freedom* (DOF) is defined as difference of the number of constraints and the number of generalized coordinates, and denotes the number of independent or non-redundant actuators. If a system is *holonomic*, we can eliminate dependent coordinates and reduce the number of generalized coordinates to the DOF. The number of reduced coordinates implies the original sense of "degree of freedom" when all the constraints are holonomic. An "ordinary" robot which is fully-actuated without passivity and redundancy is a holonomic system since its motors can be driven independently and its constraints can be represented only by the joint coordinates.

Nonholonomy is defined as "no holonomy," namely, the constraints of the system cannot be represented by equations of generalized coordinates and a time. However, in recent years especially in control and robotics [CLBW91], *nonholonomic systems* imply the systems with constraints represented by nonintegrable

*Generalized coordinates denote necessary and sufficient numbers of variables to represent the configuration of the system, i.e. positions, orientations, and joint angles etc.

differential equations including time-differentials of generalized coordinates, i.e. velocities and/or accelerations as:

$$\boldsymbol{h}(\boldsymbol{q}, \dot{\boldsymbol{q}}, \ddot{\boldsymbol{q}}, \cdots, t) = \mathbf{o} \tag{2.2}$$

The conventional control theories and methods cannot be applied to nonholonomic systems in general. Nevertheless, nonholonomic systems, e.g. car-like mobile robots, rolling contacts of disks, balls and planes, and free-flying space robots, etc. have been attracted great research interests. The reason is that these systems have the advantages that they do not require as many actuators as the generalized coordinates. We cannot reduce the number of generalized coordinates when the constraints are nonintegrable, thus, nonholonomic. Hence, the configuration space spans higher dimensional space than the DOF. Such systems which do not require as many number of actuators as the number of generalized coordinates are intrinsically completely *underactuated* systems.

2.2 History of Research on Nonholonomic Systems

In the first researches considering nonholonomic constraints in robotics, in 1987 Laumond [Lau87] discussed the kinematic constraints and path-planning of mobile robots and Vafa [Vaf87] discussed orientational control of space robots supposing unintegrability of the constraints in his dissertation. The term "nonholonomy" was not recognized as a keyword at that moment. Nakamura and Mukherjee [NM89] studied path-planning of manipulators on free-flying space robot considered as the first paper entitled with nonholonomy. Meanwhile, Salisbury [Sal82] and Kerr and Roth [KR86] indicated that the rolling contacts of fingers and objects are nonholonomic constraints, and Li, Canny and Heinzinger [LC90, LCH90] discussed the problem as motion planning under nonholonomic constraints in 1989. Nakamura and Mukherjee [NM90, NM91] proved that the angular momentum conservation of space robots is nonholonomic and proposed a motion planning under nonholonomic constraints using *bi-directional approach*.

The above research subjects are *first-order nonholonomic systems* which are defined in Sec.2.2.3, and they are divided into two groups. One group consists of mobile robots and rolling contacts, and the other is the group of free-flying objects. The former is denoted by *nonholonomic systems under kinematic constraints* and the latter is denoted by *nonholonomic systems under dynamical constraints*.

2.2.1 Nonholonomic systems under kinematic constraints

The largest group of nonholonomic researches was for car-like mobile robots [Lau90, Lau91, LS90, LS93, KKMN90, KKMN91, SAA90, SAA91, Sam93]. From the standpoint of robotics, the nonholonomic constraints is important and significant problem for path planning and tracking control of mobile robots. From the standpoint of control, the nonholonomic constraints of mobile robots are the simplest examples of nonholonomic problems. Consequently, most of researches on feedback stabilization of nonholonomic systems were developed for examples of mobile robots such as tracking control [KKMN90, KKMN91], exponential stabilization by piece-wise continuous feedback [CdWS92, SCdW92, SDE93], time-varying feedback stabilization [Sam91a, Sam91b, Sam93, Pom92, Cor92, IKY96a], discontinuous feedback stabilization [KRM94, KCdW95, KCdW96], and time-state control form [SIKK94, SKI95, SKKS96]. Some similar systems were also studied: i.e. unicycle [LdN96], fire truck [MR96] and trailers [Sør93]). Kinematic constraints of underwater vehicles are also nonholonomic path-planning problems even in 3D space, though the dynamics is extremely difficult by various forces in water. Nakamura and Savant [NS91, NS92] studied the constraints, controllability, and tracking control and Sordalen [SDE93] proposed an exponentially convergent control law. Murray and Sastry [MS91] defined *chained form* and presented the sufficiency condition to transform a symmetric affine system into chained form. The above systems can be transformed into chained form and general control theorems are developed for chained form [AS96, MS96, IKY96a]. From the studies for a mobile robot with n trailers and chained form, Sørdalen, Nakamura and Chung developed a new mechanism called a *nonholonomic manipulator* [SNC94, CNS95b, CNS95a, SNC95a] and studied its motion planning [CN96, SNC95b]. The nonholonomic manipulator is one of the minimal forms of robot mechanisms which can control any number of joints only by two motors.

The other major subject in nonholonomic problems is the problem of rolling contacts of balls, disks and planes [LC90, BS95]. The problem was discussed connected with that of rolling contacts of fingers and objects [LCH90, MLS94a], and some interesting mechanisms were developed [CNS95b, P+96, MLF97]. Li, Canny and Heinzinger [LC90, LCH90] first discussed the motion planning of the rolling contacts of fingers and objects under their nonholonomic constraints. Murray et.al. [MLS94a] studied the mathematical features of robotic manipulation by fingers. Bicchi et.al. [BS95] proposed a manipulation strategy through rolling objects with various shapes. Chung, Nakamura and Sørdalen [CNS95b] developed a *nonholonomic manipulator* using the control properties of n-trailer system for the control design as mentioned above and the nonholonomic constraints of ball-disk

contacts for the mechanism. Its transmissions using nonholonomic ball-disk constraints were called *nonholonomic gears* of which gear-ratio continuously changes from 0 to 1. Peshkin et.al. [P+96] applied a similar nonholonomic transmission to a haptic display. Luo [MLF97] developed a nonholonomic table which can be positioned at any position and orientation on a 2D plane by two actuators through rolling contacts of balls and the plane. These problems were based on the assumption that the rolling contacts do not slip and, then, the constraints are naturally geometrical. Hence, it is not necessary to consider their dynamics but their kinematics. Manipulation of objects through sliding [LM95] or throwing [ML93, Lyn96, LM96] is introduced in Sec.2.2.3 since the constraints are classified into second-order nonholonomic ones and the dynamics needs to be considered.

2.2.2 Nonholonomic systems under dynamical constraints

At the same time when the *nonholonomic systems under kinematic constraints* were studied, problems on orientational motions of free-flying space robots by internal motions of their manipulators were recognized as one of nonholonomic problems [Vaf87]. Such the problem of the free-flying system occurs from that the angular momentum conservation is nonintegrable constraint including the angular velocities. Such systems are called *nonholonomic systems under dynamical constraints*.

Systems under angular momentum conservation are often referred as the falling cat phenomenon [Mar94]. Kane and Scher [KS69] discussed the problem from a dynamical standpoint and Yamafuji et.al. [YKK92] developed a robotic falling cat. Frohlich [Fro79] studied dynamical features of somersaults on a springboard or trampoline. Kane et.al. [KS70, KHY72] proposed an orientation control of an astronaut by his limb motion and proved it through experiments. In robotics field, Lapshin [Lap91] and Nakano and Tsuchiya [NT93] investigated orientation control of a robot in jumping phase or midair. A major subject in dynamical nonholonomic researches is orientation control of free-flying space robots by manipulator motions. Umetani and Yoshida [UY87, UY89] proposed a path control of manipulators while the orientation of their base was diverging, and they introduced the generalized Jacobian. Vafa introduced nonholonomic features of dynamics and control of space robots with manipulators [Vaf87] and many researchers started to work with the problem considering the nonholonomic constraints [VD90, Lon90, NM89, NM90, NM91, Sre90, SMO91, AS93, Yam93, MZ94, Yam96, NM97] and these are introduced in Chap.3. In Chap.3, a motion planning method of the end-effector of free-flying space robots is proposed, which is called *spiral motion*.

2.2.3 2nd-order nonholonomic systems

The above two groups of researches were focused on systems under constraints represented by nonintegrable first-order differential equations including generalized coordinates and velocities as:

$$\boldsymbol{h}(\boldsymbol{q}, \dot{\boldsymbol{q}}, t) = \mathbf{o} \tag{2.3}$$

Such the constraints are called *first-order nonholonomic*. On the other hand, the constraints which arise from the dynamics and do not have even first integrals are represented by nonintegrable second-order ones, moreover, including accelerations, as

$$\boldsymbol{h}(\boldsymbol{q}, \dot{\boldsymbol{q}}, \ddot{\boldsymbol{q}}, t) = \mathbf{o} \tag{2.4}$$

Such the constraints are called *second-order nonholonomic*.

Up to recent years, the term "nonholonomy" has been used to represent only the first-order systems or, in other word, the symmetric affine driftless systems. The reason is that "nonholonomy" is equivalent to the property that "there is no smooth static state feedback stabilization to an equilibrium point" for first-order systems from the famous Brockett's theorem [Bro83]. On the other hand, Oriolo and Nakamura [ON91b] proposed that the constraints of manipulators with free joints are represented by generally nonintegrable second-order differential equations and the system were called *second-order nonholonomic*. Second-order nonholonomic systems are transformed into non-symmetric affine systems in state equation form and Brockett's theorem is not powerful to show their stabilizability. For instance, the *inverted pendulum* is, in fact, second-order nonholonomic and its approximated system around the equilibrium is stabilizable by a smooth static feedback. The *free-joint manipulator* is second-order nonholonomic and its controllability and stabilizability cannot be shown. We have had less control theories and methods to prove the controllability of some sorts of second-order nonholonomic systems. The problems of controllability and stabilizability are stated in Chap.4 and control methods of free-joint manipulators are proposed in Chaps.4, 5 and 6.

2.3 Controllability of Nonholonomic Systems

There are several terms which imply the possibility of control, i.e. controllability, reachability, accessibility, small-time local controllability(STLC). These terms are all equivalent for holonomic and first-order nonholonomic systems and proper definition of controllability hasn't been known very well. In fact, controllability of linear time-invariant systems are defined and explained in their constant matrix form and cannot be applied to nonlinear systems. *Small-time local controllability* (STLC) [Sus87] has been regarded as *controllability* for first-order nonholonomic

systems. Accessibility, reachability, and attainability denote similar meaning and are not defined clearly. However a second-order nonholonomic system is accessible [RvdSMK96], its STLC can be proved only by sufficient conditions such as Sussmann's conditions [Sus87] and the conditions are often not satisfied. Global controllability of second-order nonholonomic systems has been proved only by construction method as [LM95, Ara96]. Then, we need to distinguish these control properties for second-order nonholonomic systems. In the followings, definitions and theorems for controllability are summarized.

Consider a control system Σ of the form as:

$$\Sigma: \ \dot{\boldsymbol{x}}(t) = \boldsymbol{g}_0(\boldsymbol{x}(t)) + \sum_{i=1}^{m} \boldsymbol{g}_i(\boldsymbol{x}(t))u_i(t) \ , \quad \boldsymbol{x} \in \boldsymbol{M} \subset \boldsymbol{R}^n \tag{2.5}$$

First, the system is *globally controllable* if there exists some period $T > 0$ and input $\boldsymbol{u}(t)$:$(0 < t < T)$ satisfying $\boldsymbol{x}(0) = \boldsymbol{x}_0$, $\boldsymbol{x}(T) = \boldsymbol{x}_f$ for each two states $\boldsymbol{x}_0, \boldsymbol{x}_f \in \boldsymbol{M}$ [NvdS90, MLS94b].

If there is a trajectory which starts from $\boldsymbol{x}(0) = \boldsymbol{x}_0$ and reaches $\boldsymbol{x}(T) = \boldsymbol{x}_f$ in time T, $\boldsymbol{x}_f$ is *reachable* from $\boldsymbol{x}_0$ in time T [Sus87]. A set of $\boldsymbol{x}_f$ which is reachable from $\boldsymbol{x}_0$ in time T is called *reachable set* and represented as $\mathrm{Reach}(\Sigma, T, \boldsymbol{x}_0)$. Additionally,

$$\mathrm{Reach}(\Sigma, \leq T, \boldsymbol{x}_f) = \bigcup_{0 \leq t \leq T} \mathrm{Reach}(\Sigma, t, \boldsymbol{x}_0). \tag{2.6}$$

If $\boldsymbol{x}_0$ itself is an interior point of $\mathrm{Reach}(\Sigma, \leq T, \boldsymbol{x}_0)$ for all $T \geq 0$, the system Σ is *small-time local controllability* (STLC) from $\boldsymbol{x}_0$ [Sus87]. If the system is STLC for all $\boldsymbol{x}_0 \in \boldsymbol{M}$, it is also globally controllable unless there is a special restriction on the states or inputs. Note that these are just sufficient conditions for controllability, and the system is globally controllable even if it is not STLC.

If $\mathcal{F}$ is a family of C^∞ vector fields on a manifold M, then $L(\mathcal{F})$ denotes the Lie algebra of vector fields generated by the elements of $\mathcal{F}$. If $L(\mathcal{F})$ is the whole tangent space of $\boldsymbol{M}$ at $\boldsymbol{x}_0$, the family $\mathcal{F}$ is said to satisfy the *Lie algebra rank condition* (LARC) at $\boldsymbol{x}_0$. In other words, the following linear space extended by a set of vector space on $\boldsymbol{x}$ of the form (2.5):

$$\Delta(\boldsymbol{x}) = \{\boldsymbol{g}_0(\boldsymbol{x}), \cdots, \boldsymbol{g}_m(\boldsymbol{x})\} \tag{2.7}$$

is called the *distribution* by $\boldsymbol{g}_0, \cdots, \boldsymbol{g}_m$. If the dimension of minimum-dimensional involutive[†] distribution $\bar{\Delta}$ including Δ is equivalent to n, the system is said to satisfy LARC. An $\mathcal{F}$-trajectory is a curve $x(\cdot)$ which is a finite concatenation of

[†]Pick any two vector fields $\boldsymbol{g}_i, \boldsymbol{g}_j$ from a distribution and produce the Lie bracket as: $[\boldsymbol{g}_i, \boldsymbol{g}_j] = \dfrac{\partial \boldsymbol{g}_j}{\partial \boldsymbol{x}} \boldsymbol{g}_i - \dfrac{\partial \boldsymbol{g}_i}{\partial \boldsymbol{x}} \boldsymbol{g}_j$ The distribution is involutive if the bracket belongs to the original distribution.

integral arcs of members of $\mathcal{F}$. The family $\mathcal{F}$ has the *accessibility property* (AP) from $\boldsymbol{x}_0$ if, for every $T > 0$, the set of points that can be reached from $\boldsymbol{x}_0$ by $\mathcal{F}$-trajectories in time $\leq T$ has a nonempty interior. The following theorem is known for the accessibility [Sus87].

Proposition 1: Let $\mathcal{F}$ be a family of C^∞ vector fields on a C^∞ manifold M. Then the LARC at $\boldsymbol{x}_0$ implies the AP from $\boldsymbol{x}_0$. Conversely, the AP from $\boldsymbol{x}_0$ implies the LARC at $\boldsymbol{x}_0$ if $\boldsymbol{M}$ is a real-analytic manifold and the members of $\mathcal{F}$ are real-analytic. □

Proposition 2: A system Σ of the form (2.5), with $\boldsymbol{g} = (\boldsymbol{g}_0, \cdots, \boldsymbol{g}_m)$ real analytic, cannot be STLC from a point $\boldsymbol{x}_0$ unless $\boldsymbol{g}$ satisfies the LARC from $\boldsymbol{x}_0$. □

Namely, in general, AP is indicated by LARC and is a necessary condition for STLC. Note that the property AP does not imply that the system is *reachable* to some point.

In general, first-order nonholonomic systems can be represented in the state equation form as:

$$\dot{\boldsymbol{x}} = \sum_{i=1}^{m} \boldsymbol{g}_i u_i \tag{2.8}$$

where $\boldsymbol{x}$ denote the state variables. The Eq.(2.8) is of the form of Eq.2.5 with $\boldsymbol{g}_0 \equiv \mathbf{o}$. Such a form is called a symmetric affine system. For symmetric affine systems, LARC automatically means STLC and, hence, are globally controllable in general. Hence, LARC is also called the *controllability rank condition* for first-order nonholonomic systems.

Second-order nonholonomic systems can be represented as affine systems with drift in the state equation form as Eq.2.5. For general affine systems with drift (i.e. second-order nonholonomic system), STLC is verified by Sussmann's sufficient condition [Sus87].

For some degrees of a Lie bracket B produced by $\boldsymbol{g}_i (i = 0, \cdots, m)$ in Eq.(2.5), for instance, $\big[\boldsymbol{g}_i, \big[\boldsymbol{g}_j, [\boldsymbol{g}_k, \boldsymbol{g}_l]\big]\big]$, define $\delta_i(B)$ as a degree that $\boldsymbol{g}_i$ occurs in B, and $\sum_{i=0}^{m} \delta_i(B)$ as the degree of B. A bracket B is *bad* if $\delta_0(B)$ is odd and $\delta_i(B) (i = 1, \cdots, m)$ are all even. Otherwise, B is *good*.

Theorem 1 (Sussmann's condition) If the system (2.5) satisfies that

(1) $(\boldsymbol{g}_0, \cdots, \boldsymbol{g}_m)$ satisfies LARC at $\boldsymbol{x}_0$ and

(2) every *bad* bracket is represented by a connection of *good* brackets which are lower dimensional than the bad bracket (the bad bracket is then said to be *neutralized*),

then the system (2.5) is STLC from $\boldsymbol{x}_0$. □

This theorem is an efficient tool for verifying STLC of some of second-order nonholonomic systems. Lynch [LM95] applied the theorem to show the STLC of an object forced on a frictionless horizontal plane. Lewis and Murray [LM97] defined *configuration controllability* for a large class of Lagrangian systems including second-order nonholonomic systems, and derived conditions for *small-time local configuration controllability* (STLCC) from Sussmann's conditions based on mathematical structures of mechanical systems. Although free-joint manipulators in Chaps.4, 5 and 6 satisfy LARC, they do not satisfy Sussmann's conditions. Hence, we have to prove controllability of such second-order nonholonomic systems by the other methods, e.g. constructive method as in [Ara96].

2.4 Feedback Stabilization of Nonholonomic Systems

Not all controllable nonholonomic systems are stabilizable. The following Brockett's theorem and remarks [Bro83] are well-known.

Theorem 2 (Brockett) Let $\dot{\boldsymbol{x}} = \boldsymbol{f}(\boldsymbol{x}, \boldsymbol{u})$ be given with $\boldsymbol{f}(\boldsymbol{x}_0, \mathbf{o}) = \mathbf{o}$ and $\boldsymbol{f}(\cdot, \cdot)$ continuously differentiable in a neighborhood of $(\boldsymbol{x}_0, \mathbf{o})$. A necessary condition for the existence of a continuously differentiable control law which makes $(\boldsymbol{x}_0, \mathbf{o})$ asymptotically stable is that:

(i) the linearized system should have no uncontrollable modes associated with eigenvalues whose real part is positive.

(ii) there exists a neighborhood $\boldsymbol{N}$ of $(\boldsymbol{x}_0, \mathbf{o})$ such that for each $\boldsymbol{\xi} \in \boldsymbol{N}$ there exists a control $\boldsymbol{u}_\xi(\cdot)$ defined on $[0, \infty)$ such that this control steers the solution of $\dot{\boldsymbol{x}} = \boldsymbol{f}(\boldsymbol{x}, \boldsymbol{u}_\xi)$ from $\boldsymbol{x} = \boldsymbol{\xi}$ at $t = 0$ to $\boldsymbol{x} = \boldsymbol{x}_0$ at $t = \infty$.

(iii) the mapping

$$\gamma \ : \ \boldsymbol{R}^n \times \boldsymbol{R}^m \to \boldsymbol{R}^n$$

defined by $\gamma \ : \ (\boldsymbol{x}, \boldsymbol{u}) \mapsto \boldsymbol{f}(\boldsymbol{x}, \boldsymbol{u})$ should be onto an open set containing $\mathbf{o}$.

□

Remark 1: If the control system is of the form

$$\dot{\boldsymbol{x}} = \boldsymbol{g}_0(\boldsymbol{x}) + \sum \boldsymbol{g}_i(\boldsymbol{x})u_i \qquad ; \qquad \boldsymbol{x}(t) \in \boldsymbol{N} \subset \boldsymbol{R}^n$$

then condition (iii) implies that the stabilization problem cannot have a solution if there is a smooth distribution Δ which contains $\boldsymbol{g}_0(\cdot), \cdots, \boldsymbol{g}_m$ with $\dim\Delta < n$. □

Remark 2: One further special case: If we have

$$\dot{\boldsymbol{x}} = \sum \boldsymbol{g}_i(\boldsymbol{x})u_i \qquad ; \qquad \boldsymbol{x}(t) \in \boldsymbol{N} \subset \boldsymbol{R}^n$$

with the vector $\boldsymbol{g}_i(\boldsymbol{x})$ being linearly independent at $\boldsymbol{x}_0$ then there exists a solution to the stabilization problem if and only if $m = n$. □

It is well-known that first-order nonholonomic systems cannot be stabilized to an equilibrium point by smooth static feedback laws for the above Remark 2. Accordingly, many researchers proposed feedback control methods avoiding the restriction of Brockett's theorem as: a piecewise analytic feedback law by Canudas de Wit and Sørdalen, time-varying feedback laws by Samson [Sam91a, Sam91b, Sam93], Pomet [Pom92] and Coron [Cor92], discontinuous feedback laws by Kolmanovsky et.al. [KRM94] and Khennouf and Canudas de Wit [KCdW95, KCdW96], time-state control form by Sampei et.al. [SIKK94, SKI95, SKKS96], a method in which defects of discontinuous feedback were supplemented by time-varying feedback by Imura et.al. [IKY96a], etc.

Chapter 3

Spiral Motions of Free-Flying Space Robots

3.1 Nomenclature

$\boldsymbol{a}, \boldsymbol{b}, \boldsymbol{c}$; parameters of the closed-path motion
C ; closed path in the end-effector coordinates space
$\boldsymbol{D}$; effect of the closed-path motion
$\boldsymbol{D}_{ij} \in \boldsymbol{S}^3$; (i, j) element of $\boldsymbol{D}$ defined by Eq.(3.15),
D_{ijk} ; k-th element of $\boldsymbol{D}_{ij}$ $(k = 0, \cdots, 3)$
$d()$; *differential form* [Var84] of ()
$d\boldsymbol{x}$; *1-form* [Sch80]
$d(d\boldsymbol{x})$; *2-form* [Sch80]
E ; area enclosed by s_1 and s_2 or its value such that $dE \stackrel{\text{def}}{=} ds_1 \wedge ds_2$
$\boldsymbol{f}_i$; vector defined by Eq.7.8
$\boldsymbol{H} \stackrel{\text{def}}{=} \dfrac{\partial \boldsymbol{\epsilon}}{\partial \boldsymbol{q}}$; 4×6 Jacobian from the joint coordinates to the satellite orientation in Eq.(3.1)
$\boldsymbol{I}$; identity matrix
$\boldsymbol{J} \stackrel{\text{def}}{=} \dfrac{\partial \boldsymbol{u}}{\partial \boldsymbol{q}}$; 7×6 *Generalized Jacobian* [UYS7,NM91] from the joint coordinates to the end-effector coordinates in Eq.(3.2)
J ; augmented criterion defined by Eq.(7.10)
L ; weight for length in $\boldsymbol{W}$, [m]
n ; 'spiral pitch'
$\boldsymbol{n} \in \boldsymbol{R}^3$; unit vector which denotes rotation axis
Q ; criterion
$\boldsymbol{q} \in \boldsymbol{R}^6$; joint coordinates
q_i ; i-th component of $\boldsymbol{q}$, or the angle of i-th joint, [rad]
S ; area enclosed by C
s_1, s_2 ; time periodic functions with the period Δt
$\boldsymbol{u} \in \boldsymbol{R}^3 \times \boldsymbol{S}^3$; end-effector coordinates (position and orientation)

$\boldsymbol{v}_e$; linear velocity of the end-effector in Eq.(3.16)

$\boldsymbol{W} \stackrel{\text{def}}{=} \text{diag}\left(\frac{1}{L^2}, \frac{1}{L^2}, \frac{1}{L^2}, 1, 1, 1, 1\right)$; non-dimensionalizing matrix

$\boldsymbol{X} \stackrel{\text{def}}{=} \begin{pmatrix} \boldsymbol{Y} \\ \boldsymbol{I} \end{pmatrix}$; 11×7 Jacobian from the joint coordinates to the generalized coordinates

$\boldsymbol{X}_i \in \boldsymbol{S}^3 \times \boldsymbol{R}^3 \times \boldsymbol{S}^3$; i-th column vector of $\boldsymbol{X}$

$\boldsymbol{X}_n$; matrix $\boldsymbol{X}$ when actuated by the nominal end-effector motion $\boldsymbol{u}_n$

$\boldsymbol{x} \stackrel{\text{def}}{=} \begin{pmatrix} \boldsymbol{\epsilon} \\ \boldsymbol{u} \end{pmatrix}$; generalized coordinates of the space robot

$\boldsymbol{Y} \stackrel{\text{def}}{=} \boldsymbol{H}_0 \boldsymbol{J}^{\natural}$; 4×7 Jacobian from the end-effector coordinates to the satellite orientation

$\boldsymbol{Y}_i \in \boldsymbol{S}^3$; i-th column vector of $\boldsymbol{Y}$

$\Delta()$; change of () in Δt

Δt ; 'spiral period', [sec]

$\boldsymbol{\epsilon} = \begin{Bmatrix} e_0 \\ e_1 \\ e_2 \\ e_3 \end{Bmatrix}$; Euler parameters or satellite orientation represented by Euler parameters

$\boldsymbol{\epsilon}^* \stackrel{\text{def}}{=} \begin{Bmatrix} e_0 \\ -e_1 \\ -e_2 \\ -e_3 \end{Bmatrix}$; conjugate of $\boldsymbol{\epsilon}$

$\Delta\boldsymbol{\epsilon}_{cd} \stackrel{\text{def}}{=} \Delta\boldsymbol{\epsilon}_d - \Delta\boldsymbol{\epsilon}_n$; desired change of the satellite orientation for the closed path

θ ; rotation angle

$\boldsymbol{\lambda}$; Lagrange multiplier

$\boldsymbol{\xi}$; Gibbs vector

$\sigma \stackrel{\text{def}}{=} \|\boldsymbol{a}\|_W$; 'spiral radius'

σ_d ; upper limit of the spiral radius

$\phi \stackrel{\text{def}}{=} \frac{2\pi}{\Delta t}$; 'spiral frequency', or the angular frequency of the closed-path motion, [rad/sec]

ϕ_n ; spiral frequency for n pitches

ϕ_1 ; spiral frequency for a single-turn spiral motion

$\boldsymbol{\omega} \in \boldsymbol{R}^3$; angular velocity (of the satellite)

$\boldsymbol{\omega}_e$; angular velocity of the end-effector in Eq.(3.16)

$\wedge$; *exterior derivative* [Sch80]

$\|\boldsymbol{a}\|_W \stackrel{\text{def}}{=} \sqrt{\boldsymbol{a}^T \boldsymbol{W} \boldsymbol{a}}$; $\boldsymbol{W}$-weighted norm of $\boldsymbol{a}$

Subscripts

c	; closed-path motion element
d	; desired value
n	; nominal motion element
p	; positional element
q	; for expression by joint coordinates
ϵ	; orientational element
0	; initial value

Superscripts

(i)	; i-th iterated value
$\sharp$	; pseudoinverse matrix

3.2 Introduction

A free-flying space robot is subject to the momentum and angular momentum conservation laws. It is well known that the angular momentum conservation law is nonintegrable and thus nonholonomic [NM91]. Since the momentum conservation law forms a set of holonomic constraints, the generalized coordinates of a free-flying space robot consist of those for the satellite orientation and those for the manipulator configurations. Therefore, a free-flying space robot with a six DOF manipulator, for example, has nine generalized coordinates. Generally, it is impossible to follow an arbitrary given nine dimensional trajectory of the generalized coordinates only by the manipulator joints' actuation, if orientation control devices such as CMG are not equipped on the satellite. However, it was shown that a free-flying space robot without orientation control devices is locally controllable [NM91]. However an arbitrary given 9D trajectory cannot be followed, there can be found a feasible trajectory connecting an arbitrary initial point and arbitrary desired point in the 9D space only if the nonholonomic constraints are carefully considered in planning and control. Although it is assumed from pure technical point of view, there are various possible advantages for the system without any special orientation control device:

(1) One may consider the case of malfunction or breakdown of the device.
(2) One may wish to minimize the use of the device, if it consists of thrusters that use limited and expensive fuel.
(3) Even when the device consists of wheels, one may find frequent or continuous actuation of wheels takes too much electricity.

(4) The future designer of small space robot services may choose not to have such a heavy and bulky device if a robot can live without it.

The motion control of free-flying space robots has two major problems because of nonholonomic constraints. (1) Path planning, and (2) feedback control have been already studied in depth for the conventional fixed-base manipulators. However, they are not as intuitive for the free-flying space robots as those are for the fixed-base manipulators.

For the path planning of the fixed-base manipulators, only the environmental constraints which are commonly holonomic and thus geometric need to be considered. Meanwhile, the nonholonomic constraints need to be taken into account in addition to the environmental ones for the path planning of the free-flying space robots. This leads the fact that many intuitive path planning algorithms developed for holonomic robots become inapplicable. Vafa et.al. [VD90] proposed a method to minimize the disturbance of satellite orientation by cyclic motions of a manipulator. Nakamura et.al. [NM91] proposed a method of finding a solution by using a Lyapunov function and called it a "*bi-directional approach.*" Sreenath [Sre90] proposed a shape control of space multibody systems. Senda et.al. [SMO91] obtained a trajectory using a neural network. Akiyama et.al. [AS93] obtained an optimal trajectory for planar 2-link robots and 3D 3-link robots using nonlinear programming method. Yamada [Yam93] used the variational method to find a closed trajectory of manipulator joints that generates an arbitrary change of satellite attitude. Mukherjee and Zurowski [MZ94] introduced a pseudo-holonomic behavior of space robots.

The feedback control of free-flying space robots is difficult in particular since they fall in the class of a nonlinear system that is not stabilizable with a smooth static feedback law [Bro83]. Only a few works have been published on this issue. Sampei et.al. [SKI95] proposed feedback stabilization of a simple free-flying space robot via the time-state control form. Yamada [Yam96] applied iterative cyclic motion of manipulator joints to stabilize the satellite orientation.

In this chapter, a method to approximate an arbitrary 9D trajectory planned rather intuitively disregarding the nonholonomic constraints is proposed via introducing a spiral-like perturbation around the 9D trajectory. The perturbation is determined by careful consideration of the nonholonomic constraints. One of the advantages of this approach is that the already developed path planning algorithms for the holonomic robots can be tied to a nonholonomic path-planning algorithm. This what divides the large path-planning problem into two subproblems, one of which considers only the environmental constraints and the other takes care of the nonholonomic constraints. The spiral-like perturbation is designed around the six dimensional components that correspond to the end-effector motion, such that it

causes an appropriate change of the remaining three components of the satellite orientation. It is a theoretical feature that the method approximates an arbitrary 9D trajectory with an arbitrary small non-zero error. The method can be extended to free-flying space robots with a manipulator of higher degree of freedom and with multiple manipulators, in a straightforward manner. The spiral motion restores the configuration of the system to the desired at each end of the period and limits the deviation from the desired configuration within an arbitrary designated margin. The margin need not be designed to be very small but small just enough to avoid obstacles or boundaries only in their neighborhood. While the spiral motion is proposed here as a method of motion planning, iterative cyclic motion of the manipulator of a space robot can be applied to feedback stabilization to a desired configuration of the satellite orientation and manipulator, which was proposed by Yamada [Yam96].

3.3 The Spiral Motion

3.3.1 The concept

The concept of spiral motion is first stated rather intuitively before describing the detailed discussion. Consider a satellite and a 6 DOF manipulator on it. Although there could be more the degrees of freedom of the manipulator, the discussion in this chapter is focused on this minimum but common situation. When the attitude control device of the satellite is not used, the whole system is represented by 9 generalized coordinates, (6 of the manipulator joints and 3 of the satellite orientation) being driven by 6 joint actuators.

The 6 generalized coordinates of the manipulator may be represented by the position and orientation of the end-effector except for the singular cases. When an arbitrary trajectory is given for the 9 generalized coordinates to trace, it is generally infeasible with 6 joint actuators. Umetani and Yoshida [UY87] proposed to follow the end-effector trajectory disregarding the satellite orientation. The top two pictures of the left hand side of Fig.3.1 illustrate the case. The satellite will have $\Delta\boldsymbol{\epsilon}_n$ as a side-effect that depends on the nominal end-effector motion $\boldsymbol{u}_n(t)$. Yamada [Yam93] computed an optimal closed path in the joint space that yields the designated change of the satellite orientation and minimizes the radius of the closed path. It will also be possible to find a closed path $\boldsymbol{u}_c(t)$ of the end-effector which changes the satellite orientation into the designated configuration. The bottom two pictures of the left hand side of Fig.3.1 show such a trajectory.

The right hand side of Fig.3.1 shows the motion when two paths $\boldsymbol{u}_n$ and $\boldsymbol{u}_c$ are simply added. A simply addition of these paths $\boldsymbol{u}_n + \boldsymbol{u}_c$ traces a single-turn

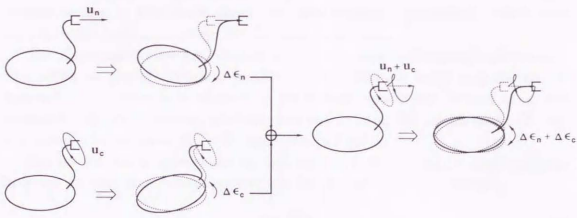

Figure 3.1: Spiral motion planning

spiral-like path. The radius of $\boldsymbol{u}_c$ is referred to as the spiral radius of $\boldsymbol{u}_n + \boldsymbol{u}_c$. The corresponding satellite orientation change becomes nearly $\Delta\boldsymbol{\epsilon}_n + \Delta\boldsymbol{\epsilon}_c$ although this simple addition is not exact due to nonlinearity. If $\boldsymbol{u}_n$ is divided into small parts and a closed path of the end-effector for each of them is computed, the spiral becomes multi-turn and the spiral radii get smaller, which is explained in the section 3.4.4. In this way, a closed path such that the trajectory of the satellite orientation approximately follows an arbitrary given one can be found. The resultant motion caused by the multi-turn spiral end-effector motion is considered an approximation of the given 9D trajectory of $\boldsymbol{u}_n$ and $\boldsymbol{\epsilon}_d$ which is physically infeasible in general. It is noteworthy that the smaller the division of the end-effector path becomes, the more the spiral radii reduce and the better the approximation becomes. From this point of view, it is possible to approximate a given 9D trajectory with arbitrary specified non-zero error. If the given trajectory includes temporal requirements, the length of path to trace in the given time becomes larger and the approximation with smaller radii results in larger velocity along the path. This problem is mathematically formulated in the following sections. A computational scheme of the minimal spiral motion is also developed where the exact nonlinearity is to be taken into consideration.

3.3.2 Generalized coordinates

Yamada [Yam93] took the manipulator joint coordinates $\boldsymbol{q}$ and the satellite orientation $\boldsymbol{\epsilon}$ as generalized coordinates, and computed a closed path of $\boldsymbol{q}$ that generates the desired change of $\boldsymbol{\epsilon}$ after a cycle. This problem was solved as an optimization in the Euclidean space $\boldsymbol{R}^6$ of the joints. Since the trajectory control of an end-effector

is important in practice, $\boldsymbol{u}$ is considered a part of the generalized coordinates in this chapter instead of joint coordinates. The two choices of generalized coordinates are physically equivalent except for the singularity cases.

The *Euler parameters* are adopted to represent three-dimensional orientation. The definition and properties of the Euler parameters are briefly summarized in Appendix A.1. Since $\boldsymbol{u}$ is adopted as generalized coordinates instead of $\boldsymbol{q}$, the proposed trajectory planning problem does not lie in an Euclidean space $\boldsymbol{R}^6$ but in a non-Euclidean space $\boldsymbol{R}^3 \times \boldsymbol{S}^3$, as shown in Fig.3.2.

The satellite orientation velocity is expressed in terms of the joint angle velocity from the *angular momentum conservation law* as follows [NM91, Yam93]:

$$\dot{\boldsymbol{\epsilon}} = \boldsymbol{H}\dot{\boldsymbol{q}} \tag{3.1}$$

On the other hand, the relationship between the end-effector velocity and the joint angle velocity satisfies the following equation [UY87, NM91]:

$$\dot{\boldsymbol{u}} = \boldsymbol{J}\dot{\boldsymbol{q}} \tag{3.2}$$

When the number of the manipulator joints is 6, $\boldsymbol{u}$ and $\boldsymbol{q}$ are diffeomorphic except for the singular points. The orientation in 3D space is represented by Euler parameters which has four elements. However the minimum required dimensions are three, the orientation space is non-Euclidean and has several singular points with only three coordinates. The advantage of the Euler parameters is that it is the most smooth representation of 3D rotation without any singular points in its space. Consequently, the coordinates are expressed by more components than required. Namely, $\boldsymbol{u}$ has seven elements and $\boldsymbol{J}$ is a 7×6 matrix. When the Jacobian $\boldsymbol{J}$ is full-rank, the solution $\dot{\boldsymbol{q}}$ for a physically consistent $\dot{\boldsymbol{u}}$ is obtained as follows:

$$\dot{\boldsymbol{q}} = \boldsymbol{J}^{\dagger}\dot{\boldsymbol{u}} \tag{3.3}$$

Adopting the *differential form* [Sch80], the equation of motion of the whole system is obtained from Eqs.(3.1) and (3.3) as follows:

$$d\boldsymbol{x} = \boldsymbol{X}d\boldsymbol{u} \tag{3.4}$$

3.4 Planning the spiral motion

In the section 3.4.1, an approximate closed trajectory for a *single-turn spiral motion* connecting the start and end points of the desired trajectory is yielded. Then, a method finding a locally optimal solution about the approximate solution obtained in Sec.3.4.1 is described in Sec.3.4.2. In the section 3.4.3, a method for searching the

exact solution of the spiral motion is described. Finally, a method for computing a *multi-turn spiral motion* to obtain the solution for the arbitrary given non-zero allowance of approximation is stated in the section 3.4.4.

Yamada proposed a variational method to find an optimal solution taking joint coordinates as the space for trajectory planning [Yam93]. In this chapter, the $\boldsymbol{R}^3 \times \boldsymbol{S}^3$ space of end-effector position and orientation is adopted as the space for trajectory planning and expressed with 7 elements using Euler parameters. As the computational algorithm of optimization, the Yamada's method is extended.

3.4.1 Single-turn spiral motion

The formula of closed trajectory motion that results in an arbitrary change of satellite orientation is derived by using the *differential form* and *Lie bracket*. The desired trajectory $\boldsymbol{x}_d$ is generally infeasible. Let $\boldsymbol{u}_n(t) \stackrel{\text{def}}{=} \boldsymbol{u}_d(t)$ denote the nominal motion of the end-effector along the desired trajectory. The difference between $\boldsymbol{u}$ and $\boldsymbol{u}_n$ is expressed as $\boldsymbol{u}_c(t) \stackrel{\text{def}}{=} \boldsymbol{u}(t) - \boldsymbol{u}_n(t)$. When $\boldsymbol{u}$ connects the start and end points of the desired trajectory, $\boldsymbol{u}_c$ becomes a closed path.

A feasible trajectory of $\boldsymbol{x}$ connecting the start and end points of the desired trajectory is obtained from Eq.(3.4).

$$\Delta \boldsymbol{x}(t) = \boldsymbol{x}_0 + \int_{t_0}^{t} \boldsymbol{X}\boldsymbol{u} dt \tag{3.5}$$

The change of generalized coordinates by $\boldsymbol{u}_n$ becomes as follows:

$$\Delta \boldsymbol{x}_n(t) = \boldsymbol{x}_0 + \int_{t_0}^{t} \boldsymbol{X}_n \boldsymbol{u}_n dt \tag{3.6}$$

Let $\boldsymbol{x}_c$ as

$$\boldsymbol{x}_c(t) \stackrel{\text{def}}{=} \boldsymbol{x}(t) - \boldsymbol{x}_n(t) = \int_{t_0}^{t} (\boldsymbol{X}\boldsymbol{u} - \boldsymbol{X}_n \boldsymbol{u}_n) dt \tag{3.7}$$

Adopting the differential form, Eq.(3.7) becomes as

$$d\boldsymbol{x}_c = \boldsymbol{X} d\boldsymbol{u} - \boldsymbol{X}_n d\boldsymbol{u}_n \tag{3.8}$$

Differentiating Eq.(3.8), it is obtained from Eq.(3.4) as

$$d(d\boldsymbol{x}_c) = \frac{\partial \boldsymbol{X}}{\partial \boldsymbol{x}} \boldsymbol{X} d\boldsymbol{u}_c \wedge d\boldsymbol{u}_c + \left(\frac{\partial \boldsymbol{X}}{\partial \boldsymbol{x}} \boldsymbol{X} - \frac{\partial \boldsymbol{X}_n}{\partial \boldsymbol{x}} \boldsymbol{X}_n \right) d\boldsymbol{u}_n \wedge d\boldsymbol{u}_n \tag{3.9}$$

The first term of Eq.(3.9) implies the change of generalized coordinates due to the closed trajectory motion. The second term means the effect due to the $\boldsymbol{u}_n$. In the case that the desired trajectory is sufficiently short, $\boldsymbol{u}_n$ can be considered small. On the other hand, in the case that the spiral trajectory is sufficiently near to the

desired trajectory, $\boldsymbol{\epsilon}$ nearly equals $\boldsymbol{\epsilon}_n$. In both cases, the second term in Eq.(3.9) can be neglected. In this section and the next the first term is only considered and the second one is neglected. Now, $d(d\boldsymbol{\epsilon}_c)$ becomes the function of only $\boldsymbol{u}_c$. $\Delta\boldsymbol{\epsilon}_c$ is obtained from *Stokes theorem* [Sch80, Yam93] and Eq.(3.9) becomes as follows:

$$\Delta\boldsymbol{x}_c = \int_C d\boldsymbol{x}_c = \int_S d(d\boldsymbol{x}_c) = \int_S \sum_{i,j} \frac{\partial \boldsymbol{X}_j}{\partial \boldsymbol{x}} \boldsymbol{X}_i du_{c,i} \wedge du_{c,j} \tag{3.10}$$

The closed trajectory $\boldsymbol{u}_c$ is expressed by two parameters s_1, s_2 as:

$$\boldsymbol{u}_c = \boldsymbol{a}s_1 + \boldsymbol{b}s_2 \tag{3.11}$$

For simplicity and smoothness of the spiral trajectory, let s_1 and s_2 be expressed by sinusoidal functions as:

$$\begin{aligned} s_1 &= \cos\phi(t - t_0) - 1 \\ s_2 &= \sin\phi(t - t_0) \end{aligned} \tag{3.12}$$

Fig.3.4.1 shows s_1 and s_2 versus time. The closed trajectory $\boldsymbol{u}_c$ becomes elliptice. The $\boldsymbol{a}$ and $\boldsymbol{b}$ denote two radii of the ellipse. From Eq.(7.3), $\boldsymbol{\epsilon}^T\boldsymbol{\epsilon} = 1$ always must be satisfied. Considering the case where $s_1 = 1$ and $s_2 = 0$ and other cases, Eqs.(3.11) and (3.12) yield the following constraints for the orientational elements (lower four components) of $\boldsymbol{a}$ and $\boldsymbol{b}$.

$$\begin{aligned} \boldsymbol{a}_\epsilon^T \boldsymbol{b}_\epsilon &= \boldsymbol{a}_\epsilon^T \boldsymbol{c}_\epsilon = \boldsymbol{b}_\epsilon^T \boldsymbol{c}_\epsilon = 0 \\ \boldsymbol{a}_\epsilon^T \boldsymbol{a}_\epsilon &= \boldsymbol{b}_\epsilon^T \boldsymbol{b}_\epsilon \end{aligned} \tag{3.13}$$

These are the additional constraints to be satisfied when the optimization in $\boldsymbol{R}^3 \times \boldsymbol{S}^3$ is carried out rather than in $\boldsymbol{R}^6$.

Adopting Eq.(3.11), Eq.(3.10) can be alternatively represented by *Lie bracket* [Var84, Sch80].

$$\begin{aligned} \Delta\boldsymbol{x}_c &= \int_F \sum_{i,j} \left(a_i b_j \frac{\partial \boldsymbol{X}_j}{\partial \boldsymbol{x}} \boldsymbol{X}_i - a_j b_i \frac{\partial \boldsymbol{X}_j}{\partial \boldsymbol{x}} \boldsymbol{X}_i \right) dE \\ &= \sum_{i,j} a_i b_j \int_E [\boldsymbol{X}_i, \boldsymbol{X}_j]\, dE \\ &= \boldsymbol{a}^T \boldsymbol{D} \boldsymbol{b} \end{aligned} \tag{3.14}$$

where $\boldsymbol{D}$ denotes a 7×7 tensor whose (i, j) element is defined as

$$\boldsymbol{D}_{ij} \stackrel{\text{def}}{=} \int_E [\boldsymbol{X}_i, \boldsymbol{X}_j]\, dE \tag{3.15}$$

Note that the satellite orientation change is expressed in terms of Lie brackets of column vectors of $\boldsymbol{X}$ and since the lower part of $\boldsymbol{x}$ is the input $\boldsymbol{u}$ itself, the lower parts of $\boldsymbol{x}_c$ and $\boldsymbol{D}_{ij}$ is equivalently zero. It is rather simpler formulation of the effect than that of Yamada's.

3.4.2 Computation of single-turn spiral motion

There are many solutions of the closed trajectory $\boldsymbol{u}_e$. An optimization method is proposed in this section. The $\boldsymbol{u}_e$ has two unknown vectors, $\boldsymbol{a}$ and $\boldsymbol{b}$ as seen in Eq.(3.11). The goal in this section is to find minimal $\boldsymbol{a}$ and $\boldsymbol{b}$.

Let the criterion to minimize as $Q = \boldsymbol{a}^T \boldsymbol{W} \boldsymbol{a} + \boldsymbol{b}^T \boldsymbol{W} \boldsymbol{b}$. The criterion can be equivalently represented by

$$Q = \frac{1}{\phi^2} \left(\frac{1}{L^2} \boldsymbol{v}_e^T \boldsymbol{v}_e + \frac{1}{4} \boldsymbol{\omega}_e^T \boldsymbol{\omega}_e \right) \tag{3.16}$$

with the relation of Eq.(7.4). Namely, the criterion is interpreted as minimizing a normalized end-effector velocity.

The following optimization is carried out as if the problem would lie in $\boldsymbol{R}^7$ rather than $\boldsymbol{R}^3 \times \boldsymbol{S}^3$. Namely, the constraints of Eq.(3.13) for lower four components of $\boldsymbol{u}$ is disregarded. This simplification makes possible to use Yamada's algorithm as it is. A brief summarization is introduced in the appendix B. At the end of this subsection, it is shown that the optimal solution thus obtained automatically satisfies the constraints of Eq.(3.13).

The $\boldsymbol{D}$ in Eq.(3.14) is a fairly complex function of $\boldsymbol{a}$ and $\boldsymbol{b}$. The Yamada's algorithm assumes that the integrands of Eqs.(3.6) and (3.15) are constant and invariant to $\boldsymbol{a}$ and $\boldsymbol{b}$. The error due to this assumption will be corrected at the next section when the exact solution is computed. Therefore, $\boldsymbol{x}(t_0 + \Delta t)$ can be represented from Eqs.(3.6), (3.7) and (3.14) as

$$\boldsymbol{x}(t_0 + \Delta t) = \boldsymbol{x}(t_0) + \Delta \boldsymbol{x}_n + \boldsymbol{a}^T \boldsymbol{D} \boldsymbol{b} \tag{3.17}$$

where $\Delta \boldsymbol{x}_n$ can be calculated as

$$\Delta \boldsymbol{x}_n = \boldsymbol{X}(\boldsymbol{u}_n(t_0 + \Delta t) - \boldsymbol{u}_n(t_0)) \tag{3.18}$$

and Eq.(3.15) is rewritten as

$$\boldsymbol{D}_{ij} = \begin{pmatrix} \left(\dfrac{\partial \boldsymbol{Y}_j}{\partial u_i} - \dfrac{\partial \boldsymbol{Y}_i}{\partial u_j} + \dfrac{\partial \boldsymbol{Y}_j}{\partial \boldsymbol{\epsilon}} \boldsymbol{Y}_i - \dfrac{\partial \boldsymbol{Y}_i}{\partial \boldsymbol{\epsilon}} \boldsymbol{Y}_j \right) E \\ \mathbf{0} \end{pmatrix} \tag{3.19}$$

The partial derivatives in Eq.(3.19) are obtained by numerical differentiation. This needs some consideration since $\boldsymbol{\epsilon}$ are the Euler parameters and are constrained on a unit 4D hypersphere. A method of numerical differentiation with Euler parameters is proposed in Appendix A.2.

To summarize the above procedure, a single-turn spiral motion is calculated as follows:

(1) Let $\boldsymbol{u}_n = \boldsymbol{u}_d(t)$, then calculate $\Delta\boldsymbol{\epsilon}_n$.

(2) Solve a closed trajectory motion $\boldsymbol{u}_c$ (or equivalently $\boldsymbol{a}$ and $\boldsymbol{b}$) which satisfies $\Delta\boldsymbol{\epsilon}_c = \Delta\boldsymbol{\epsilon}_d - \Delta\boldsymbol{\epsilon}_n$ according to the Yamada's algorithm in B.

(3) Letting $\boldsymbol{u} = \boldsymbol{u}_n + \boldsymbol{u}_c$, compute a single-turn spiral motion trajectory connecting the start and end points of the desired trajectory.

From Eq.(7.12), the optimal solutions of $\boldsymbol{a}$ and $\boldsymbol{b}$ obtained above satisfy

$$\begin{aligned} \boldsymbol{a}^T\boldsymbol{W}\boldsymbol{b} &= 0 \\ \boldsymbol{a}^T\boldsymbol{W}\boldsymbol{a} &= \boldsymbol{b}^T\boldsymbol{W}\boldsymbol{b} = -\frac{1}{2}\boldsymbol{\lambda}^T\Delta\boldsymbol{\epsilon}_{cd} \end{aligned} \tag{3.20}$$

For any choices of L in $\boldsymbol{W}$, the optimal solution thus obtained automatically satisfies the constraints of Eq.(3.13).

3.4.3 Searching for an exact solution

The previous solution is no more than an approximate solution since $\Delta\boldsymbol{\epsilon}_n$ and $\boldsymbol{D}$ are calculated only by the initial condition and the effect of $\boldsymbol{u}_n$ for $\boldsymbol{\epsilon}_c$ is not considered. Searching for the exact solution, the motion of the space robot using the approximate solution and $\Delta\boldsymbol{\epsilon}$ are calculated. Then an exact solution is searched for by iterative calculation with *Newton's method* as

$$\begin{pmatrix} \boldsymbol{a}^{(i)} \\ \boldsymbol{b}^{(i)} \end{pmatrix} = \begin{pmatrix} \boldsymbol{a}^{(i-1)} \\ \boldsymbol{b}^{(i-1)} \end{pmatrix} - \left(\frac{\partial\Delta\boldsymbol{\epsilon}}{\partial\boldsymbol{a}} \frac{\partial\Delta\boldsymbol{\epsilon}}{\partial\boldsymbol{b}} \right)^{\sharp} (\Delta\boldsymbol{\epsilon} - \Delta\boldsymbol{\epsilon}_d) \tag{3.21}$$

where the second term of the right side is calculated using $\boldsymbol{a}^{(i-1)}, \boldsymbol{b}^{(i-1)}$.

Note that though the approximate solution requires only the initial and final values of $\boldsymbol{u}_n$, $\Delta\boldsymbol{\epsilon}$ is calculated while searching for the exact solution by the following integration.

$$\Delta\boldsymbol{\epsilon} = \int_{t_0}^{t_f} \boldsymbol{Y}(\dot{\boldsymbol{u}}_n + \dot{\boldsymbol{u}}_c)dt \tag{3.22}$$

Therefore, the exact solution follows the desired trajectory.

3.4.4 Multi-turn spiral motion

Previously, the single-turn spiral motion which connects the start and end points of an arbitrary 9D trajectory was proposed. However, if the environment of a space robot is surrounded by obstacles, the space robot should avoid them. In this subsection, the *"multi-turn spiral motion"* which enables one to approximately follow an arbitrary 9D trajectory with an arbitrary margin is proposed.

From Eq.(3.20), σ implies the radius of closed trajectory. The spiral frequency of single-turn spiral motion from $t = t_0$ to $t = t_0 + \Delta t$ is $\phi_1 = \dfrac{2\pi}{\Delta t}$ and E in Eq.(3.19) becomes $E = \dfrac{\phi_1 \Delta t}{2} = \pi$. For multi-turn spiral motion within Δt, the spiral frequency is represented by $\phi_n = n\phi_1 = \dfrac{2n\pi}{\Delta t}$ and, therefore, $E = \dfrac{\phi_n \Delta t}{2} = n\pi$. Since E is proportional to spiral pitch n as above, $\boldsymbol{D}$ is proportional to n from Eq.(3.19), and σ^2 is inversely proportional to n from Eq.(3.14). Accordingly, it is inversely proportional to ϕ. Namely,

$$\sigma^2 \propto \frac{1}{n} \propto \frac{1}{\phi} \tag{3.23}$$

Therefore, the larger the spiral pitch (that is, faster the spiral frequency) is, the smaller the spiral radius is.

A method to solve a multi-turn spiral motion is described by imposing σ_d as:

(1) Set $n^{(0)} = 1$.

(2) Calculate $\Delta t = \dfrac{t_f - t_0}{n}$ and $\phi = \dfrac{2\pi}{\Delta t}$.

(3) Solve a single-turn spiral motion with ϕ in (2). Obtain the spiral radius σ.

(4) Compute $n^{(k)}$ by rounding up $n^{(k-1)} \times \left(\dfrac{\sigma}{\sigma_d}\right)^2$ to the nearest whole number.

(5) If $n^{(k)} = n^{(k-1)}$, then the $n^{(k)}$ gives the maximum single-turn spiral motion, with the spiral limit σ_d. Otherwise, return step (2).

(6) Compute the next spiral starting from the end of the previous spiral. Set $n^{(0)} = n^{(k)} - 1$. Go to step (2).

A multi-turn spiral trajectory approximating the desired trajectory within the spiral limit can be solved by the above procedure. The procedure is illustrated in Fig.3.4.

Since the spiral perturbation is determined repeatedly at each cycle, it can be designed to reduce the motion error generated or accumulated in the previous cycles. This implies the method is suitable as a feedback control method, if computed in real-time with faster computers in the future.

3.5 Computer Simulation

The lengths, mass, and inertia matrices of the satellite and each link of the space robot are assumed as given in Table 3.5, where the 0-th link denotes the base satellite. The arrangement of each link and joint is given in Fig.3.5. The

Table 3.1: Link parameters

Link	Length[m]	Mass[kg]	Inertia[kg·m^2]		
0	$\phi 2 \times 1$	500	100	100	100
1	0.2	10	0.1	0.1	0.1
2	1.0	30	3	0.2	3
3	0.5	20	0.5	0.2	0.5
4	0.5	20	0.5	0.2	0.5
5	0.1	10	0.1	0.1	0.1
6	0.2	20	0.1	0.1	0.1

satellite (link(0)) is a cylinder of which radius is 2[m] represented as $\phi 2$ in Fig.3.5 and Table 3.5 and height is 1[m]. The positions of the center of gravity of each link are assumed at the geometric center of the link.

The initial configuration of the space robot is $\boldsymbol{q} = \left(\frac{\pi}{3}, -\frac{\pi}{3}, \frac{\pi}{3}, -\frac{\pi}{3}, \frac{\pi}{3}, -\frac{\pi}{3}\right)$[rad] with the configuration of Fig.3.5 as the origin. The desired trajectory of the end-effector is to move it for 1 second at the constant speed 0.5[m/sec] in the positive x-axis direction and to maintain its orientation. And that of the satellite orientation is to maintain the satellite orientation. The initial configuration and the desired trajectory are given in Fig.3.6, where the broken line stretched from end-effector denotes the desired trajectory.

Figure 3.7 shows the satellite orientation variation in response to the end-effector desired trajectory without spiral motion. The solid, broken and chain line denote the 3 vector elements of Euler parameters in the order. Figure 3.8 shows the same motion every 0.2[sec].

The results of single-turn spiral motion are shown in Figs. 3.9 through 3.11. In the figure 3.9, the solid line denotes the end-effector coordinate x variation, the broken and the chain line denote y and z. The dotted lines denote each desired trajectories. Figure 3.10 shows the satellite orientation variation. Figure 3.11 illustrates the motion every 0.2[sec].

The figures 3.12 through 3.14 correspond to the multi-turn spiral motion when the spiral radius limit σ_d sets 0.1[m]. Figures 3.12 and 3.13, similarly to Figs.3.9 and 3.10, show the end-effector coordinate variation and the satellite orientation variation. Figure 3.14 illustrates the motion, where only the trajectory of end-effector position was plotted. The satellite with solid line denotes the final state and that with broken line denotes the initial state. Note that the satellite makes small fluctuation in Fig.3.13 while making multi-turn spiral motion.

From Figs.3.7 and 3.8, it is seen that the satellite orientation would be subject to a great disturbance when following the end-effector desired trajectory. When the spiral motion is applied, a trajectory connecting the start and end points is obtained as in Figs.3.9 through 3.14. Especially, the infeasible desired trajectory is approximated with the desired spiral radius by the multi-turn spiral motion as in Figs.3.12 through 3.14. If the spiral limit σ_d is chosen smaller, one can get a multi-turn spiral motion with better approximation. Since ϕ is inversely proportional to ${\sigma_d}^2$, the motion becomes much faster in this case.

Table 3.2: Computational time

Computational time [sec]		Spiral motion		
		none	Single	Multi
Direction	x	20	3.0×10^3	5.7×10^3
	y	20	3.7×10^3	–
	z	20	3.0×10^3	3.5×10^3

Similar simulations are done for all three axes of x, y and z and showed almost similar results. The computational time by Sun SPARC station 10 is shown in Table 2 for each case of none, single-turn, and multi-turn spiral motion.

3.6 Effects of Singularity

In the course of computer simulations, it is found that for some desired trajectories there are cases where the searching convergence to the exact solution becomes very slow. It turned out that it happens when the system passes by the neighborhood of a singular point in the trajectory. The relationship between singularity and convergence of the solution is investigated with spiral radius in the cases of multi-turn spiral motions in Figs. 3.12 through 3.14. The results are shown in Fig. 3.15. The (a) shows magnitudes of the spiral radius, normalized by the spiral period $\Delta t = \dfrac{t_f - t_0}{n}$, where the solid line and empty circles denote $\dfrac{\|\boldsymbol{a}\|_W}{\sqrt{\Delta t}}$. The broken line and crosses denote $\dfrac{\|\boldsymbol{b}\|_W}{\sqrt{\Delta t}}$. The (b) shows the number of iterations in each period of single-turn spiral motion, normalized by the spiral period Δt. The (c) shows variations of the condition numbers, where the solid line and empty circles denote the condition numbers of $\boldsymbol{Y}$ in the motion, and the broken line and crosses denote the condition number of the generalized Jacobian $\boldsymbol{J}$.

From Fig. 3.15, it can be seen that after the condition number becomes larger near $t = 0.7$[s] and $t = 0.9$[s], the spiral radius and the number of iterations becomes larger suddenly near $t = 0.8$[s] and $t = 1.0$[s]. Iterative calculation should continue until the error becomes sufficiently small. However, in practice when the number of iterations becomes too large the iteration was terminated and it advanced to the next spiral. Although some error remained, the error is expected to be resolved in the step afterward. The convergence that actually resulted was worse, since a larger orientation error had to be resolved in the following steps. This what seems the reason that the number of iterations tends to be large at the end of motion after the neighborhood of singular points. The singularities would also reduce the accuracy of the calculation particularly for small spiral radii. The resolution of this problem belongs to the open problem. In a practical sense, the spiral radii should be maximized within the designated margin.

3.7 Conclusion

Space robots cannot realize an arbitrary motion of the manipulator and satellite only by actuation of the manipulator joints. The followings are made clear from this study:

(1) A method to approximate infeasible motions by spiral-like perturbations around the desired trajectory of the end-effector with an arbitrary non-zero maximum allowance was proposed.

(2) Transitions of the satellite orientation with the end-effector motion were formulated in the non-Euclidean space $\boldsymbol{R}^3 \times \boldsymbol{S}^3$. The Yamada's variational method was extended to obtain the optimal spiral motion.

(3) Multi-turn spiral motion was proposed and a method to solve them was constituted by imposing the upper limit of the spiral radius.

(4) The effectiveness of computation was verified by computer simulation. In the course of the simulation, the problem that convergence becomes slow after passing through neighborhoods of singular points was pointed out. It would be one of the open problems.

Note that the motions of space robots are intrinsically geometric since the nonholonomic constraints are first-order without dynamics. Therefore, the planned motion can be extended by time-scaling when the resultant motion would be extremely rapid.

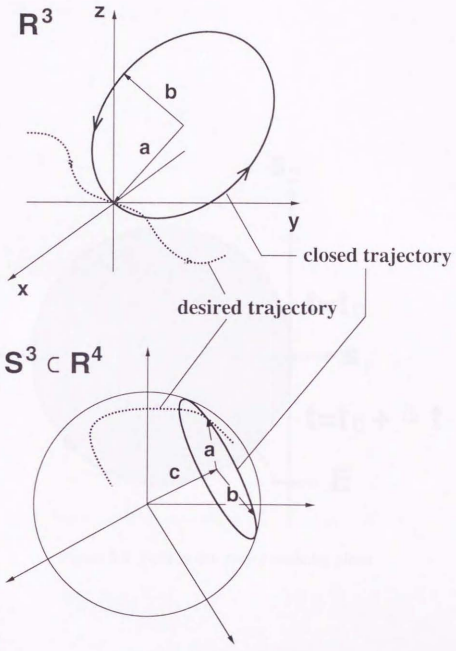

Figure 3.2: Trajectory in non-Euclidean space:
The top indicates the mapping of the desired closed trajectory in $R^3 \times S^3$ into R^3 (end-effector position), the bottom shows the mapping of the same path into S^3 (end-effector orientation).

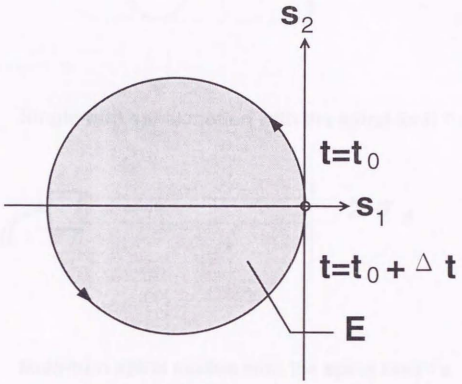

Figure 3.3: Path in the time parameter plane

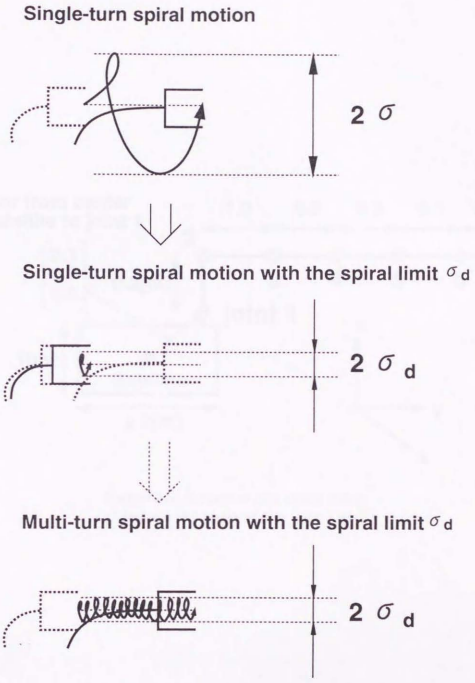

Figure 3.4: Multi-turn spiral motion planning

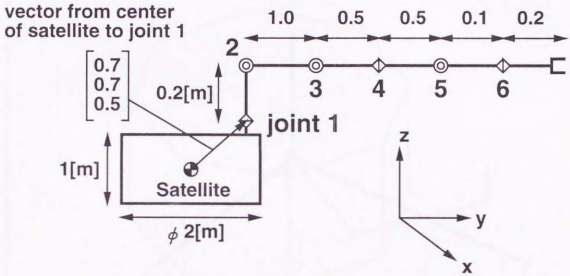

Figure 3.5: Structure of a space robot
(q_i denotes the angle of the joint i [rad])

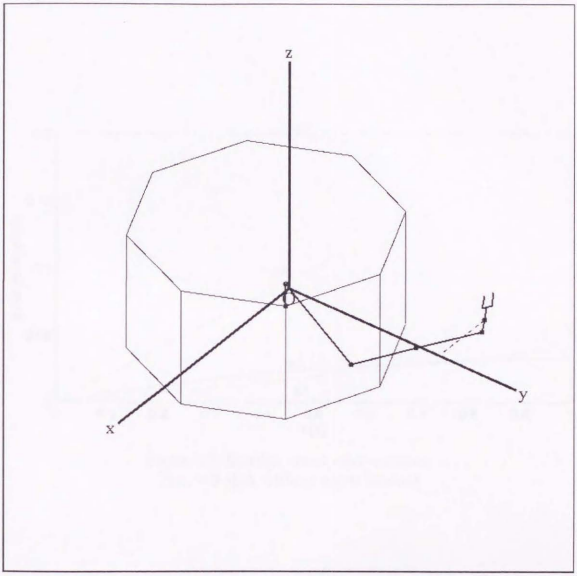

Figure 3.6: Initial configuration of the space robot

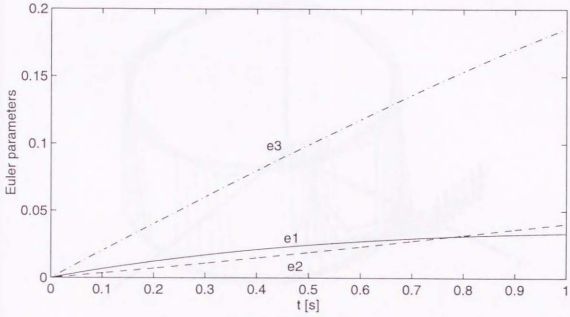

Figure 3.7: Satellite orientation variation
($\Delta u_r = 0.5$[m], without spiral motion)

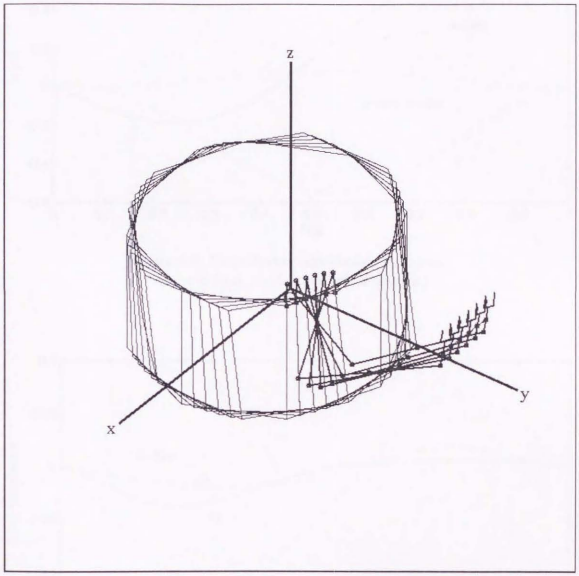

Figure 3.8: Movements of the space robot
($\Delta u_x = 0.5$[m], without spiral motion)

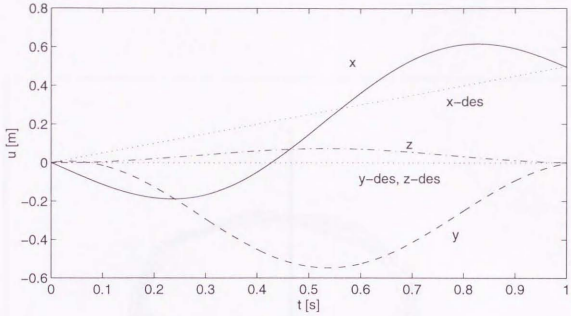

Figure 3.9: End-effector coordinates variation
($\Delta u_x = 0.5$[m], single-turn spiral motion)

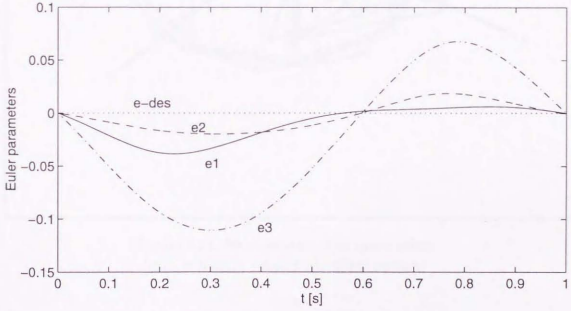

Figure 3.10: Satellite orientation variation
($\Delta u_x = 0.5$[m], single-turn spiral motion)

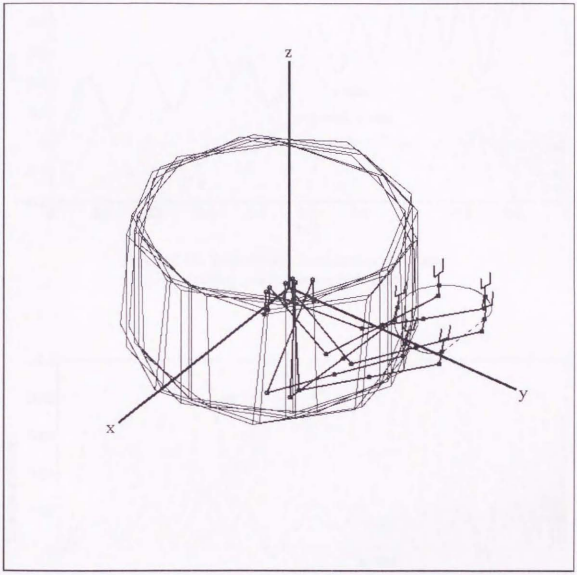

Figure 3.11: Movements of the space robot
($\Delta u_z = 0.5$[m], single-turn spiral motion)

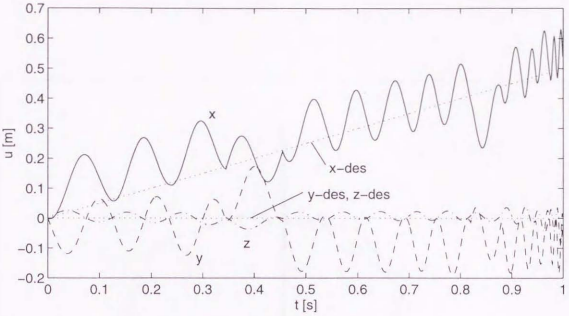

Figure 3.12: End-effector coordinates variation
($\Delta u_x = 0.5$[m], multi-turn spiral motion)

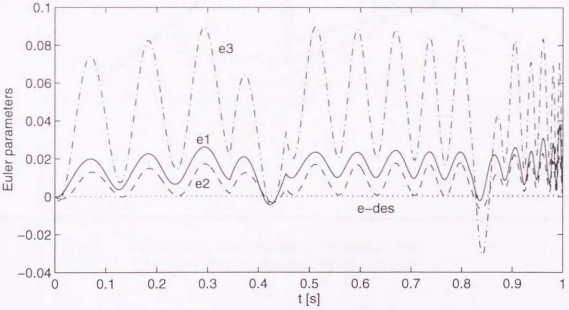

Figure 3.13: Satellite orientation variation
($\Delta u_x = 0.5$[m], multi-turn spiral motion)

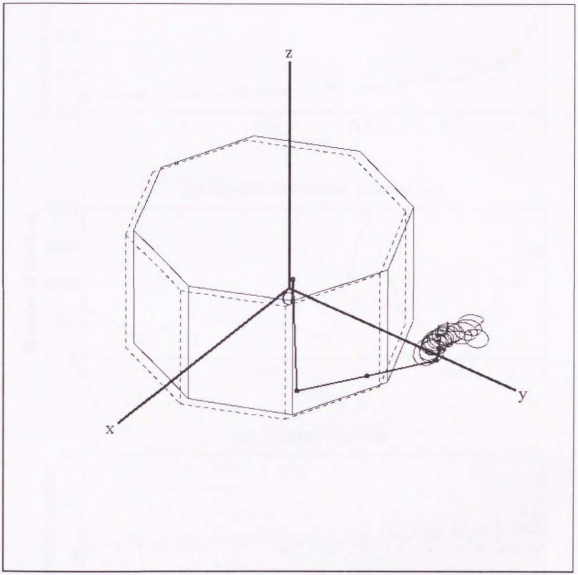

Figure 3.14: Movements of the space robot
($\Delta u_r = 0.5$[m], multi-turn spiral motion)

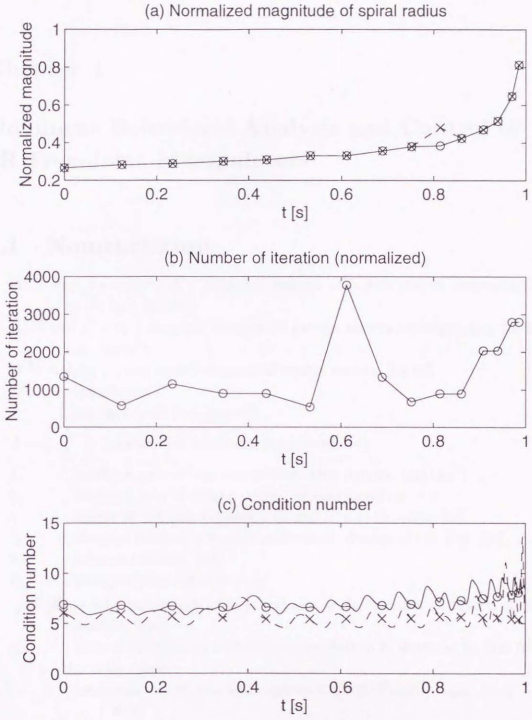

Figure 3.15: Effects of singular points
($\Delta u_x = 0.5$[m], multi-turn spiral motion)

Chapter 4

Nonlinear Behavioral Analysis and Control of 2R Free-Joint Manipulators

4.1 Nomenclature

$A_1 \stackrel{\text{def}}{=} m_1 {l_{c1}}^2 + m_2 {l_1}^2 + I_1$; diagonal element of inertia matrix corresponding to 1st link, [kg·m^2]

$A_2 \stackrel{\text{def}}{=} m_2 {l_{c2}}^2 + I_2$; diagonal element of inertia matrix corresponding to 2nd link, [kg·m^2]

$B \stackrel{\text{def}}{=} m_2 l_1 l_{c2}$; non-diagonal element of inertia matrix, [kg·m^2]

H ; Hamiltonian

I_i ; inertia of i-th link, [kg·m^2]

$\boldsymbol{J} = \begin{pmatrix} J_1 \\ J_2 \end{pmatrix}$; generalized momenta, [kg·m^2·rad/sec]

k_1 ; feedback gain of input-amplitude with signum, [rad/sec^2]

k_2 ; feedback gain of elliptic radius for compensation > 0

l_i ; length of i-th link between i-th and $(i+1)$-th joints, [m]

l_{ci} ; distance between i-th joint and center-of-mass of i-th link, [m]

m_i ; mass of i-th link, [kg]

P_{ϕ_0} ; Poincaré map cut at $\phi = \bar{\phi}_0$

$r_d \stackrel{\text{def}}{=} |\theta_{2d} - \theta_e|$; half-length of principal axis in θ_2 direction of desired elliptic manifold, [rad]

r_ω ; ratio of principal axis of elliptic manifold in $\dot{\theta}_2$ direction to that in θ_2 direction, [rad]

r_0 ; intersection of θ_2 axis and connected actual Poincaré map, [rad]

$\boldsymbol{x} = \boldsymbol{x}(t) \stackrel{\text{def}}{=} \begin{pmatrix} \theta_1(t) \\ \theta_2(t) \\ J_1(t) \\ J_2(t) \end{pmatrix}$; trajectory of system (4.6)

$\boldsymbol{x}_2(\phi,\varepsilon) \stackrel{\text{def}}{=} \begin{pmatrix} \theta_2(\phi,\varepsilon) \\ \Omega(\phi,\varepsilon) \end{pmatrix}$; phase state of second joint

$\alpha_1 = \alpha_1(\theta_2, J_1, J_2) \stackrel{\text{def}}{=} \dfrac{B\cos\theta_2 \cdot J_1 - (A_1 + B\cos\theta_2)J_2}{\Delta(\theta_2)}$; dynamic parameter, [rad/sec]

$\alpha_2 = \alpha_2(\theta_2, J_1, J_2) \stackrel{\text{def}}{=} \dfrac{A_2 J_1 - (A_2 + B\cos\theta_2)J_2}{\Delta(\theta_2)}$; dynamic parameter, [rad/sec]

γ ; amplitude of periodic input τ, [kg·m^2·rad/sec] , or $\ddot{\theta}_1$, [rad/sec^2]

γ_0 ; nominal input-amplitude, [rad/sec^2]

$\Delta = \Delta(\theta_2) \stackrel{\text{def}}{=} A_1 A_2 - B^2\cos^2\theta_2$; denominator element of dynamic parameter, [kg^2·m^4]

δ_r ; feedback error of squared elliptic radius

$\delta\theta_2$; bound of neighborhood of destination in θ_2 axis, [rad]

$\varepsilon \stackrel{\text{def}}{=} \dfrac{\gamma}{\omega^2}$; nondimensionalized amplitude of periodic input

$\boldsymbol{\theta} = \begin{pmatrix} \theta_1 \\ \theta_2 \end{pmatrix}$; generalized coordinates, or angle of i-th joint, [rad]

θ_c ; center of elliptic manifold, [rad]

$\mu \stackrel{\text{def}}{=} \dfrac{B}{A_2} = \dfrac{m_2 l_1 l_{c2}}{m_2 {l_{c2}}^2 + I_2}$; dynamic coefficient

Σ ; neighborhood of destination where termination control is applied defined by Eq.(4.27)

$\Sigma^{\bar{\phi}_0}$; intersection in phase space

τ ; generalized force, [kg·m^2·rad/sec^2]

$\phi \stackrel{\text{def}}{=} \omega t$; nondimensionalized torus time coordinate, [rad]

$\Omega \stackrel{\text{def}}{=} \dfrac{d\theta_2}{d\phi} = \dfrac{1}{\omega}\dot{\theta}_2$; nondimensionalized angular velocity of 2nd joint

ω ; angular frequency of periodic input, [rad/sec]

$\bar{*}$; averaged coordinates corresponding to $*$

Subscripts

d ; desired value

Superscripts

(k) ; k-th evaluation

4.2 Introduction

Manipulators with free joints are typical examples of second-order nonholonomic systems and underactuated mechanisms. Oriolo and Nakamura [ON91b] [ON91a] clarified that the dynamical constraints of a manipulator with free joints are generally nonintegrable and, therefore, second-order nonholonomic.

On control of a manipulator with free joints, Arai and Tachi [AT91] studied a path control of a manipulator with electromagnetic brakes at free joints. Nakamura and Iwamoto [NI93] discussed a space multi-link structure with free joints and its shape control. Seto and Baillieul [SB94] discussed a control theory of super-articulated mechanical systems, which had an equilibrium stabilizable by the feedback linearization approach. Wichlund, Sørdalen and Egeland [WSE95] discussed the integrability and stabilizability of a class of underactuated dynamical systems including underwater vessels. Nakamura, Iwamoto and Yoshimoto [NIY95] proposed a stabilization method of a 2R free-joint manipulator to a stable equilibrium. Recently, Arai [Ara96] proved the controllability of a 3-link manipulator with a free joint and two actuated joints by constructive method. De Luca, Mattone and Oriolo [LMO96b] discussed control properties of a class of underactuated mechanisms and proposed a control method of 2P1R redundant manipulator with two dimensional end-effector commands. Imura, Kobayashi and Yoshikawa [IKY96b] proposed an exponential stabilization of 2P1R free-joint manipulator with two actuators. De Luca, Mattone and Oriolo [LMO96a] proposed a control method of 2R free-joint manipulator via nilpotent approximation.

Although free-joint manipulators are similar to pendulums, all the configurations with zero velocity are connecting equilibrium manifold without gravitational potential. Free-joint manipulators are also different from pendulums in controllability and stabilizability where pendulums are stabilizable to its equilibrium via exact linearization. The largest advantage of free-joint manipulators is that they have a possibility to control larger number of joints only by one actuator, while first-order nonholonomic systems require two or more actuators.

In this chapter, the nonlinear behaviors of a free-joint manipulator are investigated. A simple planar 2R manipulator with the second joint free is adopted to obtain mathematical insights of the nonlinearity. The analysis of nonlinear dynamical behavior and the simultaneous positioning of both joints are the focus of this chapter. Although the results derived in this chapter are tied with the particular mechanism, the approaches and tools of analysis developed in this chapter will be a part the basis of further research of free-joint manipulators with higher complexity.

4.3 A Free-Joint Manipulator

4.3.1 Dynamics modeling

A planar 2R manipulator in Fig.1 has the first joint actuated and the second joint free and stays in the horizontal plane. This is the simplest model of nonholonomic free-joint manipulators.

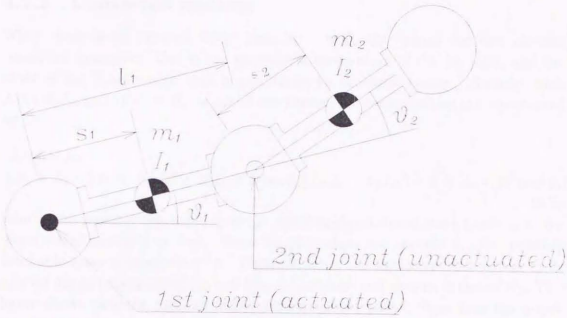

Figure 4.1: A planar 2R free-joint manipulator

The Hamiltonian is represented by

$$H = \frac{A_1 {J_2}^2 + A_2(J_2 - J_1)^2 + 2B\cos\theta_2 \cdot J_2(J_2 - J_1)}{2(A_1 A_2 - B^2\cos^2\theta_2)} \tag{4.1}$$

$\boldsymbol{J}$ are obtained through the Hamilton's canonical transformation as follows:

$$\boldsymbol{J} = \begin{pmatrix} (A_1 + A_2 + 2B\cos\theta_2)\dot{\theta}_1 + (A_2 + B\cos\theta_2)\dot{\theta}_2 \\ (A_2 + B\cos\theta_2)\dot{\theta}_1 + A_2\dot{\theta}_2 \end{pmatrix} \tag{4.2}$$

The dynamics of the manipulator is obtained by

$$\begin{aligned} \frac{d\boldsymbol{\theta}}{dt} &= \frac{\partial H}{\partial \boldsymbol{J}} \\ \frac{d\boldsymbol{J}}{dt} &= -\frac{\partial H}{\partial \boldsymbol{\theta}} \end{aligned} \tag{4.3}$$

Namely,

$$\frac{d}{dt}\begin{pmatrix} \theta_1 \\ \theta_2 \\ J_1 \\ J_2 \end{pmatrix} = \begin{pmatrix} \alpha_2(\theta_2, J_1, J_2) \\ -\alpha_1(\theta_2, J_1, J_2) - \alpha_2(\theta_2, J_1, J_2) \\ \tau \\ B\sin\theta_2 \cdot \alpha_1(\theta_2, J_1, J_2) \cdot \alpha_2(\theta_2, J_1, J_2) \end{pmatrix} \tag{4.4}$$

$$(\theta_1, \theta_2, J_1, J_2) \in \boldsymbol{T}^2 \times \boldsymbol{R}^2$$

4.3.2 Conserved motions

When there is no external force, namely, $\tau = 0$, the system has two obvious conserved quantities. One is the generalized momentum of the 1st joint, and the other is the Hamiltonian that is equivalent to the total energy. Namely, with $J_1(0) = J_{10}$ and $H(0) = H_0$ as initial conditions, the conservations are represented by

$$\begin{aligned} &J_1(t) = J_{10} \\ &(A_1 + A_2 + 2B\cos\theta_2){J_2}^2 + 2(A_2 + B\cos\theta_2)J_{10}J_2 + A_2{J_{10}}^2 - 2(A_1A_2 - B^2\cos^2\theta_2)H_0 = 0 \end{aligned} \tag{4.5}$$

Hence, the possible reachable space in the four-dimensional state space is a two dimensional manifold or less. Since Eq.(4.1) does not include θ_1, the possible reachable space is invariant for θ_1. Figure 2 shows the sections perpendicular to θ_1 axis for initial conditions of $J_{10} = 0.1$[kg·m^2·rad/sec] and various values of H_0. The figure shows that the motions follow ordered closed paths. Note that the upper two and lower two curves in Fig.4.2 are also closed at $\theta_2 = \pm\pi$ since the space of θ_2 is $\boldsymbol{S}^1$.

The behaviors of systems with strong nonlinearity are drawing much attention in various research fields. Chaos is one such behavior. It is known [Tab89] that, for continuous systems, chaos is observed in a 3 dimensional manifold or higher. The two conserved quantities of Eq.(4.5) reduce the dimension to two, and provide an ordered behavior as in Fig.4.2.

4.3.3 Nonlinear behaviors with periodic inputs

When the system is subject to time-periodic input of $\tau = \gamma\cos\omega t$, the dynamics is represented by

$$\frac{d}{dt}\begin{pmatrix} \theta_1 \\ \theta_2 \\ J_1 \\ J_2 \\ \phi \end{pmatrix} = \begin{pmatrix} \alpha_2(\theta_2, J_1, J_2) \\ -\alpha_1(\theta_2, J_1, J_2) - \alpha_2(\theta_2, J_1, J_2) \\ \gamma\cos\phi \\ B\sin\theta_2 \cdot \alpha_1(\theta_2, J_1, J_2) \cdot \alpha_2(\theta_2, J_1, J_2) \\ \omega \end{pmatrix}$$

$$(\theta_1, \theta_2, J_1, J_2, \phi) \in \boldsymbol{T}^2 \times \boldsymbol{R}^2 \times \boldsymbol{T}^1 \tag{4.6}$$

Note that a new coordinate ϕ is included in Eq.(4.6) to make an autonomous system. Although J_1 is not conserved any more, it is easily integrated and solved as

$$J_1 = J_{10} + \frac{\gamma}{\omega}(\sin\phi - \sin\phi_0) \tag{4.7}$$

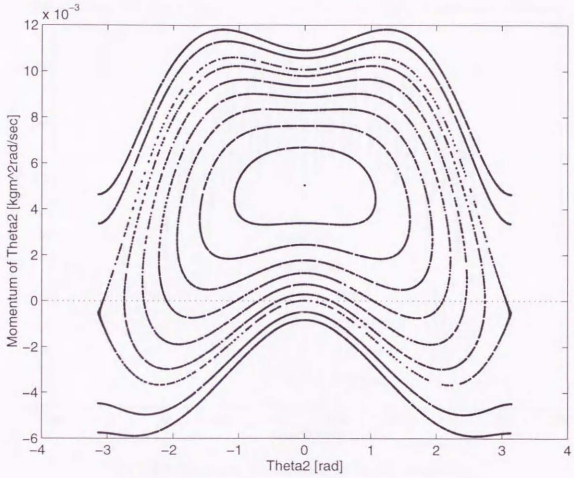

Figure 4.2: Phase plane at $J_1 = 0.1[\text{kg}\cdot\text{m}^2\cdot\text{rad/sec}]$

which implies a new conservation. Since there neither is the energy conservation, the dimension of the manifold on which the system evolves is four.

Chaos is characterized by two fundamental natures, namely, the sensitive dependence on initial conditions (SDIC) and the topological transitivity. Their brief definitions is provided in appendix C. Figure 4.3 shows trajectories starting from four mutually close initial values for the case with $\gamma = 4[\text{kg}\cdot\text{m}^2\cdot\text{rad/sec}^2]$ and $\omega = 2\pi[\text{rad/sec}]$. The solid line has $(J_1, J_2, \theta_1, \theta_2)|_{t=0} = (0, 0, 0, 0)$ as the initial condition. The other lines have small differences in the initial value of θ_2 as seen in the figure. The figure illustrates that the difference of trajectories diverges as time goes on, which implies the SDIC.

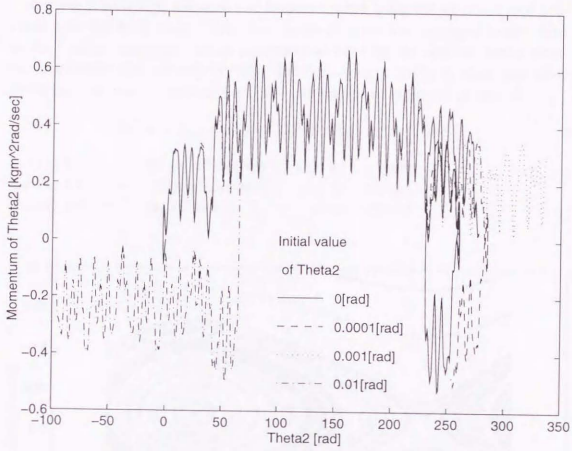

Figure 4.3: Sensitive dependence on initial conditions

The Poincaré map is an intersection of trajectories in the whole phase space with a certain hyper-plane. It reduces the dimension and helps to understand the system's behavior. Let $\Sigma^{\bar{\phi}_0}$ be the intersection in the phase space:

$$\Sigma^{\bar{\phi}_0} \stackrel{\text{def}}{=} \left\{ (\boldsymbol{x}, \phi) \in \boldsymbol{T}^2 \times \boldsymbol{R}^2 \times \boldsymbol{T}^1 \mid \phi = \bar{\phi}_0 \right\} \tag{4.8}$$

Then, the Poincaré map is represented by the mapping as

$$P_{\bar{\phi}_0} : \Sigma^{\bar{\phi}_0} \mapsto \Sigma^{\bar{\phi}_0}, \left(\boldsymbol{x} \left(\frac{\bar{\phi}_0 - \phi_0}{\omega} \right), \bar{\phi}_0 \right) \mapsto \left(\boldsymbol{x} \left(\frac{\bar{\phi}_0 - \phi_0 + 2\pi}{\omega} \right), \bar{\phi}_0 + 2\pi \right) \tag{4.9}$$

or

$$\boldsymbol{x} \left(\frac{\bar{\phi}_0 - \phi_0}{\omega} \right) \mapsto \boldsymbol{x} \left(\frac{\bar{\phi}_0 - \phi_0 + 2\pi}{\omega} \right) \tag{4.10}$$

The fixed points of $P_{\bar{\phi}_0}$ imply the periodic trajectories with the period $2\pi/\omega$, and the k-period points of $P_{\bar{\phi}_0}$ imply the periodic trajectories that pass k times through $\Sigma^{\bar{\phi}_0}$ before returning the initial state.

Figures 4.4 through 4.6 show the Poincaré maps being cut at $\phi = 0$ and projected onto the θ_2-H plane. Note that the θ_2-H plane was employed rather than the θ_2-J_2 plane, since the two are equivalent and the former provides better physical insights for the current problems. The behaviors in the θ_2-J_2 plane also show similarity. The initial conditions and the parameters of input are chosen as

$$(\theta_1, \theta_2, J_1)|_{t=0} = (0[\text{rad}], 0[\text{rad}], 0[\text{kg} \cdot \text{m}^2 \cdot \text{rad/sec}])$$

for Fig.4.4: $\gamma = 0.04$ [kg·m^2·rad/sec^2], $\omega = 2\pi$ [rad/sec]
for Fig.4.5: $\gamma = 0.4$ [kg·m^2·rad/sec^2], $\omega = 2\pi$ [rad/sec]
for Fig.4.6: $\gamma = 4$ [kg·m^2·rad/sec^2], $\omega = 2\pi$ [rad/sec]

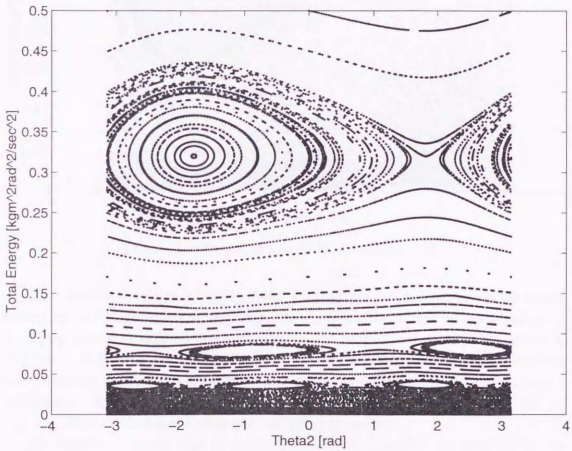

Figure 4.4: Poincaré map with $\gamma = 0.04, \omega = 2\pi$

Only γ was set at a different value and $\omega = 2\pi$ was applied for each figure. Various initial values of J_2 were chosen and their trajectories were plotted in the figures.

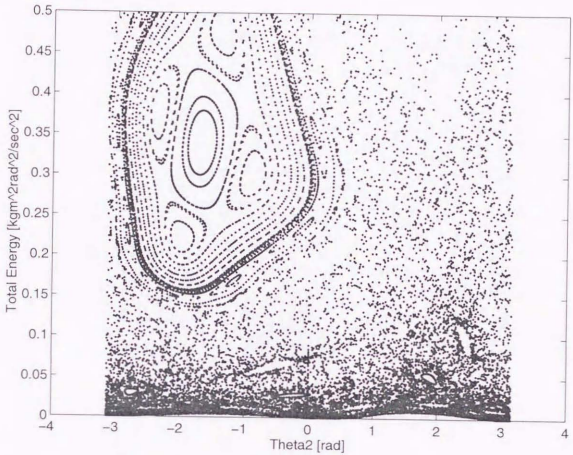

Figure 4.5: Poincaré map with $\gamma = 0.4, \omega = 2\pi$

The conserved motion of the system with zero input torque would be represented by a horizontal straight line in the θ_2-H plane, which means rotation of θ_2. In the case with a small input-amplitude, the motion is perturbed and shows a difference. In the Poincaré map, the frequency of the rotation of θ_2 originated from the conserved motion and the frequency of time-periodic input mutually cause a resonance. The series of cavities or eye balls along lines parallel to the θ_2 axis in Fig. 4.4 show the harmonic resonance of different orders.

The figures illustrate that as amplitude γ becomes larger, the homoclinic trajectories connecting the saddle points in Fig. 4.4 start collapsed as seen in Fig. 4.5. When the amplitude grows further in Fig. 4.6, the system shows complete topological transitivity. These results conclude that the free-joint 2R manipulator driven by a time-periodic input follows a cyclic trajectory in the θ_2-H plane when the amplitude is small, while it behaves chaotic with the large amplitudes.

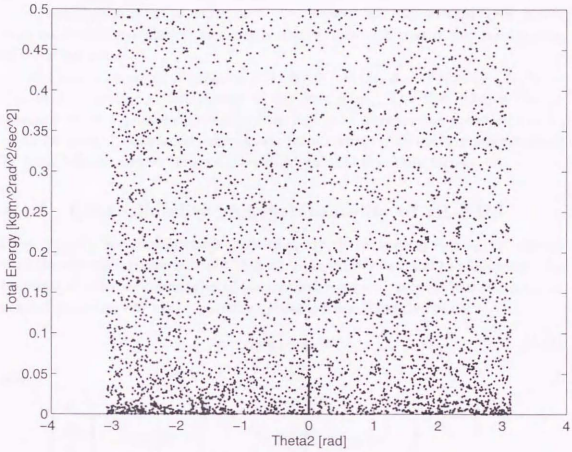

Figure 4.6: Poincaré map with $\gamma = 4, \omega = 2\pi$

It is noteworthy that the behavior of such a simple deterministic mechanical system varies from cyclic one to chaotic one in response to the growth of input-amplitude. In the sections that follows, we propose to design a controller based on the cyclic behavior for smaller input-amplitude. Although use of chaotic behavior remains in the scope of future research, it would be significant to establish control for rapid and gross motions.

4.4 Nonlinear Control of 2R-FJM

Oriolo and Nakamura [ON91b] concluded that smooth feedback stabilization to a single equilibrium point is not possible, and derived a control law for the asymptotic stabilization to equilibrium manifold as

$$M = \{(\theta_1, \theta_2, \dot{\theta}_1, \dot{\theta}_2) \mid \theta_1 = \theta_{1d}, \dot{\theta}_1 = \dot{\theta}_2 = 0\}$$

In this section, positioning of both joints of the free-joint manipulator is discussed and a control law that enables to go from an arbitrary initial point to an arbitrary single equilibrium point is established. The control law uses time-periodic inputs with amplitude modulation and means neither feedback control nor stabilization in the strict sense.

The basic strategy of positioning is (1) $(\theta_1, \dot{\theta}_1) \rightarrow (\theta_{1d}, 0)$ and then (2) $(\theta_2, \dot{\theta}_2) \rightarrow (\theta_{2d}, 0)$ with a time-periodic input of the first joint. The first subgoal can be attained by simple feedback control of the first joint disregarding the motion of θ_2, or by Oriolo and Nakamura's asymptotic stabilization to an equilibrium manifold. In what follows, control to meet the second subgoal is mainly focused on.

4.4.1 Controllability and stabilizability of 2R-FJM

First, control and stabilization properties are to be investigated in accordance with the control theories as in the chapter 2. In this section and the followings, the following simpler representation of the dynamics is more suitable to discussions on control than Eq.(4.6) in the previous section on nonlinear dynamics:

$$\dot{\boldsymbol{x}} = \boldsymbol{g}_0(\boldsymbol{x}) + \boldsymbol{g}_1(\boldsymbol{x})u \tag{4.11}$$

where

$$\boldsymbol{x} = \begin{pmatrix} \theta_1 \\ \theta_2 \\ \dot{\theta}_1 \\ \dot{\theta}_2 \end{pmatrix}, \quad \boldsymbol{g}_0(\boldsymbol{x}) = \begin{pmatrix} \dot{\theta}_1 \\ \dot{\theta}_2 \\ 0 \\ -\mu\dot{\theta}_1^2 \sin\theta_2 \end{pmatrix}, \quad \boldsymbol{g}_1(\boldsymbol{x}) = \begin{pmatrix} 0 \\ 0 \\ 1 \\ -(1+\mu\cos\theta_2) \end{pmatrix}$$

and $u = \ddot{\theta}_1$. The above representation is in the form of Eq.(2.5) in the chapter 2 of general control theories and is a drift system with a single input.

4.4.1.1 Accessibility and STLC

First, several Lie brackets produced by $\boldsymbol{g}_0$ and $\boldsymbol{g}_1$ are obtained as:

$$\boldsymbol{g}_2 = [\boldsymbol{g}_0, \boldsymbol{g}_1] = \frac{\partial \boldsymbol{g}_1}{\partial \boldsymbol{x}}\boldsymbol{g}_0 - \frac{\partial \boldsymbol{g}_0}{\partial \boldsymbol{x}}\boldsymbol{g}_1 = \begin{pmatrix} -1 \\ 1+\mu\cos\theta_2 \\ 0 \\ \mu(2\dot{\theta}_1 + \dot{\theta}_2)\sin\theta_2 \end{pmatrix} \tag{4.12}$$

$$\boldsymbol{g}_3 = [\boldsymbol{g}_0, \boldsymbol{g}_2] = \begin{pmatrix} 0 \\ -2\mu(\dot{\theta}_1 + \dot{\theta}_2)\sin\theta_2 \\ 0 \\ \mu(\dot{\theta}_1 + \dot{\theta}_2)^2\cos\theta_2 + \mu^2\dot{\theta}_1^2\cos 2\theta_2 \end{pmatrix} \tag{4.13}$$

$$\boldsymbol{g}_4 = [\boldsymbol{g}_1, \boldsymbol{g}_2] = \begin{pmatrix} 0 \\ 0 \\ 0 \\ -\mu^2 \sin 2\theta_2 \end{pmatrix} \tag{4.14}$$

And the distribution formed by $\boldsymbol{g}_0$, $\boldsymbol{g}_1$, $\boldsymbol{g}_2$, and $\boldsymbol{g}_3$ satisfies the Lie algebra rank conditions as:

$$\text{span}\,\{\boldsymbol{g}_0, \boldsymbol{g}_1, \boldsymbol{g}_2, \boldsymbol{g}_3\} \in \boldsymbol{R}^4$$

except for a few singularity points. Therefore, the accessibility condition is proved. However, the STLC cannot be proved from Sussmann's condition since the *bad* bracket $\boldsymbol{g}_4 = [\boldsymbol{g}_1, [\boldsymbol{g}_0, \boldsymbol{g}_1]]$ cannot be *neutralized* by lower dimensional *good* brackets, $\boldsymbol{g}_0$, $\boldsymbol{g}_1$, and $\boldsymbol{g}_2$. Nevertheless, the Sussmann's condition is just a sufficient condition of STLC and, furthermore, STLC is just a sufficient condition of global controllability. Consequently, there is currently no way to show controllability of the free-joint manipulator except to develop a control method as in the following sections.

Stabilizability of the free-joint manipulator is investigated by Remark 1 of Brockett's theorem. The smooth distribution, $\Delta = \{\boldsymbol{g}_0, \boldsymbol{g}_1\}$, is obviously lower than the dimension of the system and, then, there is no smooth static feedback law to stabilize the system to an equilibrium. Additionally, configuration flatness is to be investigated in the next paragraph.

4.4.1.2 Configuration Flatness of 2R-FJM

Let me investigate configuration flatness [RM96] of 2R-FJM. The Riemannian metric g is represented by:

$$g = \begin{bmatrix} A_1 + 2B\cos\theta_2 + A_2 & B\cos\theta_2 + A_2 \\ B\cos\theta_2 + A_2 & A_2 \end{bmatrix} \tag{4.15}$$

If I assume the control vector field P as $P = \text{span}\{d\theta_1\}$, the annihilator of P becomes $\text{ann}P = \{\frac{\partial}{\partial\theta_2}\}$ and, then, $\boldsymbol{\xi} = \frac{\partial}{\partial\theta_2}$. Par the derivation in [RM96],

$$\nabla_{\frac{\partial}{\partial\theta_1}}\boldsymbol{\xi} = \nabla_{\frac{\partial}{\partial\theta_2}}\boldsymbol{\xi} = \frac{\mu\sin\theta_2}{\frac{a}{c} - \mu}\left\{-\frac{\partial}{\partial\theta_1} + (1 + \mu\cos\theta_2)\frac{\partial}{\partial\theta_2}\right\} \tag{4.16}$$

Then,

$$D = \text{span}\left\{\boldsymbol{\xi}, \nabla_{\frac{\partial}{\partial\tau}}\boldsymbol{\xi}\right\} = \text{span}\left\{\frac{\partial}{\partial\theta_2}, -\frac{\partial}{\partial\theta_1} + (1 + \mu\cos\theta_2)\frac{\partial}{\partial\theta_2}\right\} \tag{4.17}$$

$D = TQ$ for generic points on Q, for generic parameter values (unless b or c equal 0, or $\sin\theta_2 = 0$) and hence the systems is not configuration flat regardless of the potential energy function.

4.4.2 Control with periodic inputs

The input torque of the first joint is determined such that the acceleration of the joint is time-periodic, namely, $\ddot{\theta}_1 = \gamma \cos \omega t$, which guarantees that $(\theta_1, \dot{\theta}_1)$ always returns to $(\theta_{1d}, 0)$ after each cycle. The dynamics of the system with the input is represented as:

$$\frac{d}{dt}\begin{pmatrix} \theta_1 \\ \theta_2 \\ \dot{\theta}_1 \\ \dot{\theta}_2 \\ \phi \end{pmatrix} = \begin{pmatrix} \dot{\theta}_1 \\ \dot{\theta}_2 \\ \gamma \cos \phi \\ -\mu \dot{\theta}_1^2 \sin \theta_2 - (1 + \mu \cos \theta_2)\gamma \cos \phi \\ \omega \end{pmatrix}$$

$$(\theta_1, \theta_2, \dot{\theta}_1, \dot{\theta}_2, \phi) \in \boldsymbol{T}^2 \times \boldsymbol{R}^2 \times \boldsymbol{T}^1 \tag{4.18}$$

Integrating with initial values of $\dot{\theta}_{10} = 0$ and $\phi_0 = 0$, θ_1 and $\dot{\theta}_1$ can be eliminated from Eq.(4.18). Nondimensionalizing Eq.(4.18) yields the following simpler equation:

$$\frac{d}{d\phi}\begin{pmatrix} \theta_2 \\ \Omega \end{pmatrix} = \begin{pmatrix} \Omega \\ -\mu\varepsilon^2 \sin \theta_2 \sin^2 \phi - (1 + \mu \cos \theta_2)\varepsilon \cos \phi \end{pmatrix}$$

$$(\theta_2, \Omega) \in \boldsymbol{T}^1 \times \boldsymbol{R}^1 \tag{4.19}$$

The nonlinear behavior of Eq.(4.19) is to be investigated by using the Poincaré map as in subsection 4.3.3. With large amplitudes of the input, it is observed in Fig.4.7 that the dynamics shows chaotic behavior as seen in subsection 4.3.3

On the other hand, with rather small amplitudes of γ, namely, of ε, the system shows well-ordered behavior as seen in the Poincaré map of Fig.4.8, where the curves have their initial values at $(\dot{\theta}_2, \gamma, \omega) = (0, 6, 4\pi)$ and various values of θ_2. From the figure, the Poincaré maps of the system with a small amplitude form an ellipse-like closed curve, or waving curve locating upper or lower of ellipses, in the phase plane. A closed curve in the phase plane denotes a periodic swing of the second joint, and an waving curve which is also closed denotes a revolution. Note that the second joint naturally swings directly by periodic actuation of the first joint, which is disregarded in the figures by taking Poincaré maps, and these swing and revolution occur as side effects and have much slower frequency than the frequency of the periodic input. Another interesting and useful feature was observed from the difference between Fig.4.8 and Fig.4.9 with a different input-amplitude $\gamma = 8$. Increasing and decreasing the amplitude tends to stretch and shrink the elliptic manifolds in the vertical direction of $\dot{\theta}_2$ as seen in the figures. The feature is utilized to control the second joint to a manifold which is formulated in the next subsection.

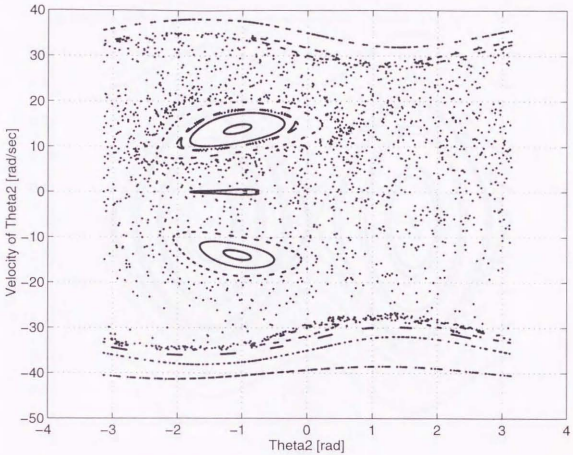

Figure 4.7: Poincaré map with $\gamma = 60, \omega = 4\pi$

4.4.3 Feedback control to an elliptic manifold

In this subsection, a feedback control law to an elliptic manifold that passes through $(\theta_2, \dot{\theta}_2) = (\theta_{2d}, 0)$ is designed. Approximate the manifold by an ellipse as

$$\frac{\left(\dfrac{\dot{\theta}_2}{r_\omega}\right)^2 + (\theta_2 - \theta_e)^2}{{r_d}^2} = 1 \tag{4.20}$$

The r_ω and θ_e depend on the input-amplitude and are determined from simulation results for a nominal input-amplitude, γ_0.

Let γ denote an amplitude of periodic input and change it at the beginning of every cycle depending upon the distance from the ellipse. This can be considered the amplitude modulation of feedback error. The modulation is according to the following law:

$$\gamma \;=\; \gamma_0 + k_1 \delta_r \tag{4.21}$$

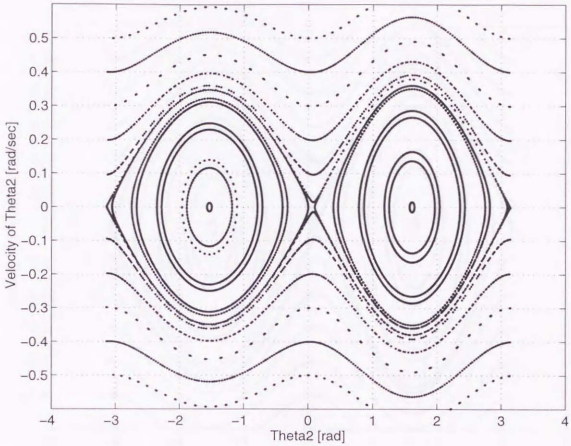

Figure 4.8: Poincaré map with $\gamma = 6, \omega = 4\pi$

$$\delta_r = \frac{\left(\frac{\dot{\theta}_2}{r_\omega}\right)^2 + (\theta_2 - \theta_c)^2}{{r_d}^2} - 1 \tag{4.22}$$

The feedback gain k_1 has a constant magnitude and changes its signum depending upon the area in the phase plane as shown in Fig. 4.10. The nominal amplitude γ_0 should be chosen such that Eq.(4.20) best approximates the corresponding Poincaré map. If $(\theta_2, \dot{\theta}_2)$ is on the desired ellipse, $(\theta_2, \dot{\theta}_2)$ approximately follows it afterward with this amplitude. When $(\theta_2, \dot{\theta}_2)$ is off the desired ellipse, the feedback law of Eqs.(4.21) and (4.22) chooses another *taller-and-narrower* or *shorter-and-wider* ellipse that will intersect with the desired ellipse afterward. This feedback law was designed on the basis of the observation at the end of 4.4.2. This heuristic design of feedback law will be shown to make the elliptic manifold as an attractor of $(\theta_2, \dot{\theta}_2)$ by simulations and experiments in the subsequent sections.

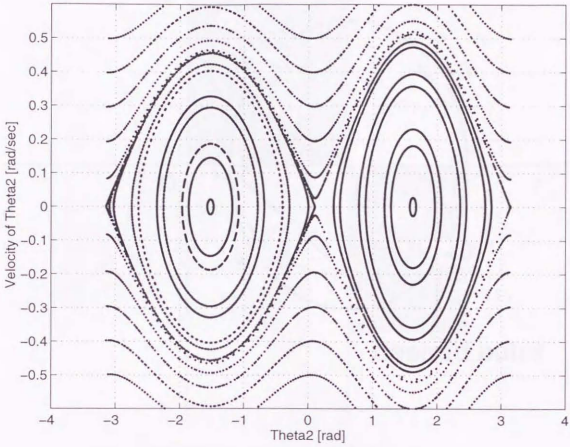

Figure 4.9: Poincaré map with $\gamma = 8, \omega = 4\pi$

Stability analysis and the possibility of generalization are major theoretical subjects of the proposed heuristic feedback law. Since it involves discretization to get the Poincaré map and approximation to represent an ellipse, a rigorous analysis of stability is not straightforward. The problem is as important as analytical identification of parameters of elliptic manifolds. The discussions in the next chapter provide analytical identification of invariant manifolds of free-joint manipulators. The generalization of proposed feedback law to higher dimensional systems with more free joints is not obvious as it is but is provided in the next chapter via averaging analysis. Nevertheless, the use of time-periodic inputs and the idea of feedback control with amplitude modulation are worth considered for generalization since they can be developed, as indicated in this chapter, with the Poincaré map known as a strong mathematical tool of nonlinear dynamics analysis.

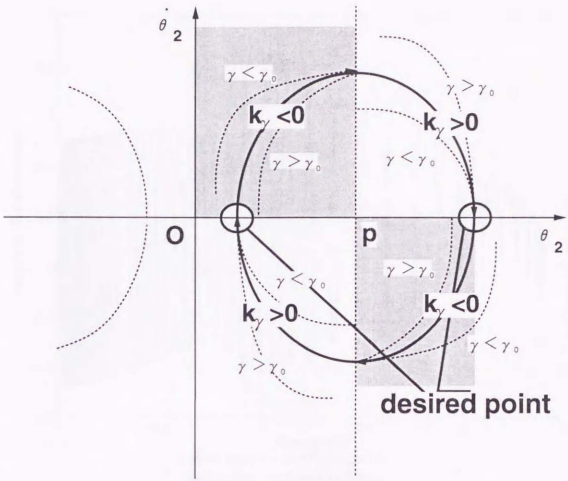

Figure 4.10: Amplitude modulation of the feedback error

Figure 4.11 shows one of the simulation results with the initial condition $(\theta_2, \dot{\theta}_2) = (0, 0)$ and the desired position $\theta_{2d} = \frac{3\pi}{4}$[rad]. The constants used were $\gamma_0 = 6$[rad/sec^2] and $\omega = 4\pi$[rad/sec]. The dotted line in Fig.4.11 indicates the desired ellipse. The solid line implies the whole trajectory of the system. The small circles in the figure denote the Poincaré maps of the trajectory. It is observed from the figure that the desired ellipse attracted $(\theta_2, \dot{\theta}_2)$.

4.4.4 Stopping at the destination

Although the Poincaré map follows the elliptic manifold by the feedback law developed in subsection 4.4.3, it does not guarantee to terminate the system at the destination $(\theta_2, \dot{\theta}_2) = (\theta_{2d}, 0)$ that the ellipse passes through. The motion near the destination is enlarged from Eq.(4.10) and shown in the left figure of Fig.4.13.

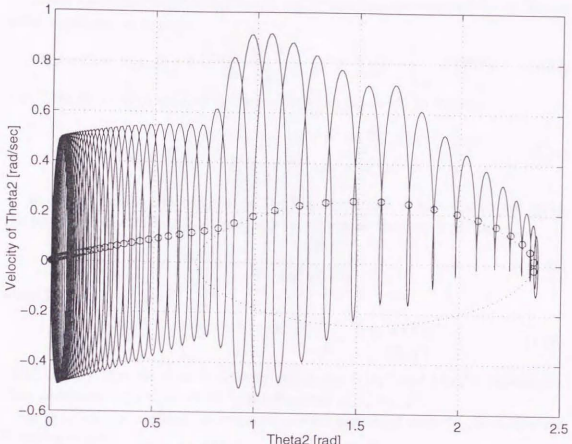

Figure 4.11: Simulation : control from 0 to $\frac{3\pi}{4}$[rad]

The motion will continue and follow the elliptic path, although in these figures the computation was terminated when the Poincaré map passed the destination. The system can stop at the destination only when the Poincaré map very fortunately makes its footprint (a small circle) exactly on the destination. In this subsection, determination of the input-amplitude in the neighborhood of the destination, namely, the input of the last cycle before the destination, is proposed so as to make the following footprint on the horizontal axis ($\dot{\theta}_2 = 0$) rather than to remain on the ellipse with the feedback law of Eqs.(4.21) and (4.22). Note that this strategy does not guarantee to reach the destination but does to stop the motion in the neighborhood of the destination. The followings describe how to compute the input-amplitude.

When ε is small, the ϕ-evolution of $\boldsymbol{x}_2(\phi, \varepsilon)$ can be approximated by the Taylor series expansion as follows:

$$\boldsymbol{x}_2(\phi, \varepsilon) = \boldsymbol{x}_2(\phi, 0) + \varepsilon \left.\frac{\partial \boldsymbol{x}_2(\phi, \varepsilon)}{\partial \varepsilon}\right|_{\varepsilon=0} + \frac{1}{2}\varepsilon^2 \left.\frac{\partial^2 \boldsymbol{x}_2(\phi, \varepsilon)}{\partial \varepsilon^2}\right|_{\varepsilon=0} + \boldsymbol{O}(\varepsilon^3) \tag{4.23}$$

The Poincaré map of $\boldsymbol{x}_2(\phi, \varepsilon)$ is calculated using Eq.(4.19) as follows:

$$\begin{pmatrix} \theta_2 \\ \Omega \end{pmatrix} \mapsto \begin{pmatrix} \theta_2 + 2\pi\Omega + \frac{1}{2}\pi^2\varepsilon^2\mu^2 \sin 2\theta_2 + O(\varepsilon^3) \\ \Omega + \frac{1}{2}\pi\varepsilon^2\mu^2 \sin 2\theta_2 + O(\varepsilon^3) \end{pmatrix} \tag{4.24}$$

In order to make the footprint on the horizontal axis of $\dot{\theta}_2 = 0$ after the cycle, the upper element of Eq.(4.24) suggests to determine the amplitude by

$$\varepsilon_d = \sqrt{\frac{2\Omega}{-\pi\mu^2 \sin 2\theta_2}} \tag{4.25}$$

From Eq.(4.24), we have

$$\begin{pmatrix} \theta_2 \\ \Omega \end{pmatrix} \mapsto \begin{pmatrix} \theta_2 + \pi\Omega + O({\varepsilon_d}^3) \\ O({\varepsilon_d}^3) \end{pmatrix} = \begin{pmatrix} \theta_2 + O({\varepsilon_d}^2) \\ O({\varepsilon_d}^3) \end{pmatrix} \tag{4.26}$$

which implies that the error of velocity and θ_2 are $O({\varepsilon_d}^3)$ and $O({\varepsilon_d}^2)$ respectively. The corresponding amplitude of $\ddot{\theta}_1$ is computed as $\gamma_d = \varepsilon_d\omega^2$.

In practice, the proposed termination control is applied when $(\theta_2, \dot{\theta}_2)$ enters the following region:

$$\Sigma \stackrel{\text{def}}{=} \left\{(\theta_2, \dot{\theta_2}) \in \boldsymbol{T}^1 \times \boldsymbol{R}^1 \mid \varepsilon_d < \varepsilon_0,\ |\theta_2 - \theta_{2d}| < \delta\theta_2\right\} \tag{4.27}$$

From Eq.(4.25), $\varepsilon_d < \varepsilon_0$ in Eq.(4.27) yields

$$\dot{\theta}_2 = \omega\Omega \begin{cases} > -\frac{1}{2}\pi\omega{\varepsilon_0}^2\mu^2 \sin 2\theta_2 & : \text{for } \sin 2\theta_2 < 0 \\ < -\frac{1}{2}\pi\omega{\varepsilon_0}^2\mu^2 \sin 2\theta_2 & : \text{for } \sin 2\theta_2 > 0 \end{cases} \tag{4.28}$$

The concept of termination control is shown in Fig.4.12. Figure 4.13 compares the simulation results of the strategies proposed in subsection 4.4.3 (left) and this subsection (right). The right shows that $(\dot{\theta}_2, \theta_2)$ terminated near the destination. Note that Eqs.(4.24) and (4.25) imply that the change of velocity by ε becomes very small in the neighborhood of $\theta_2 = \pm\frac{N\pi}{2}$, which is the singularity of the strategy. A stabilization control at $\theta_2 = \pm\frac{\pi}{2}$ proposed by Nakamura and Iwamoto [NI93] can be used in this case, while $\theta_2 = 0$ and $\pm\pi$ are saddle points as seen in Fig.4.8 and can be reached carefully following a stable manifold.

In the control strategy proposed in subsection 4.4.3 and this, the amplitude of time-periodic input is determined at the beginning of every cycle. Therefore, the control is open-loop within a cycle, although it is closed-loop between cycles.

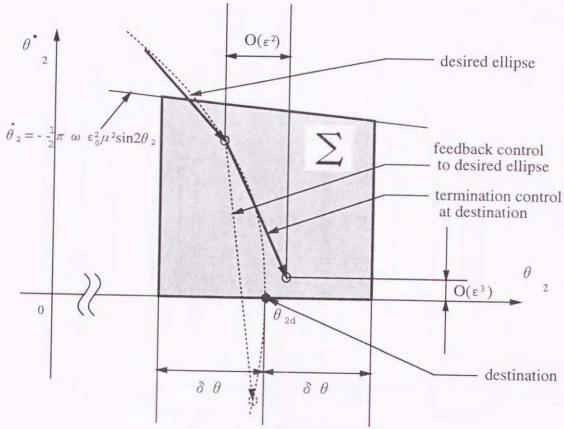

Figure 4.12: Stopping at the destination

4.4.5 Compensating the modeling error

An ellipse is employed to model the Poincaré map of Fig. 4.8. However, the modeling error tends to become large for those passing near $\theta_2 = 0, \pm\pi$. This results in the fact that the actual Poincaré map does not go through the desired position θ_{2d}, even though the elliptic manifold is chosen so and the feedback law of Eqs.(4.21) and (4.22) is designed based on the ellipse. In order to compensate this error, the desired elliptic manifold is adaptively modified in this subsection. Namely, whenever the actual Poincaré map passes the θ_2 axis (every half rotation of the Poincaré map), the constant r_d in Eq.(4.22) is modified according to the following rule:

$$r_d^{(k+1)} = r_d^{(k)} \left(1 + k_2 \cdot \frac{r_d^{(k)} - r_0}{r_0} \right) \tag{4.29}$$

The effect of this compensation was verified by simulation. Figure 4.14 shows a result of simulation. The initial condition and the destination were $(\theta_2, \dot{\theta}_2) = \left(\frac{\pi}{3}, 0\right)$ and $(\theta_2, \dot{\theta}_2) = \left(\frac{\pi}{18}, 0\right)$, respectively. The dotted line in the figure shows the

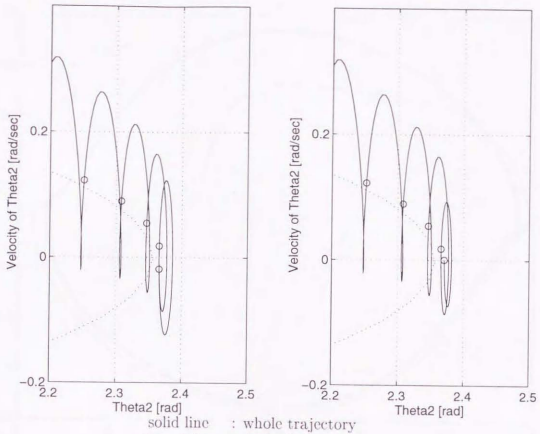

Figure 4.13: Simulation : stopping at $\frac{3\pi}{4}$

original ellipse that goes through the destination. The actual connected Poincaré map is represented by the solid line. Although the destination is close to $\theta_2 = 0$ where the modeling error becomes large, the actual Poincaré map reached the destination after a few rotations.

4.4.6 Global attraction

The control strategy in section 4.4.3 makes use of two elliptic families as seen in Fig.4.8. The family in the right half plane ($0 \leq \theta_2 \leq \pi$) has the half plane as the region of attraction and so does the family in the left. Therefore, nothing is promised for an initial state having its destination in the opposite half plane. In this subsection, it is shown that the global attraction can be guaranteed by a simple modification.

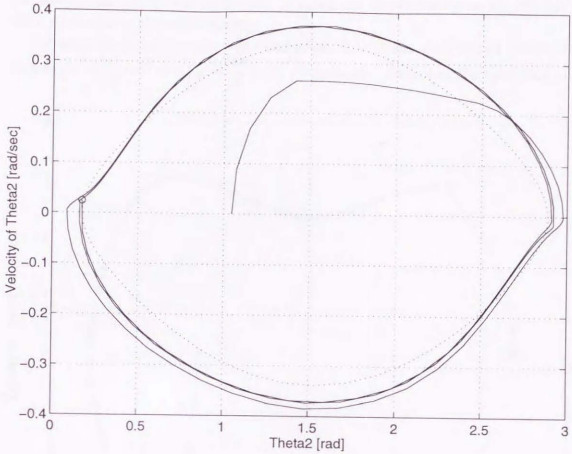

Figure 4.14: Simulation with compensating the modeling gap

It is important to note on the Poincaré maps above or below the elliptic families in Fig.4.8. The Poincaré maps above the families flow from the left to the right through $\dot{\theta}_2$ axis, while those below the families flow from the right to left. Therefore, if the initial state is in $\theta_2 < 0$ and $\dot{\theta}_2 > 0$, for example, the input-amplitude γ is determined such that the initial state flows from the left plane to the right plane. Accordingly, the area of $\dot{\theta}_2 > 0$ and $\theta_2 < 0$ can be included in the region of attraction of the elliptic family on the right half plane.

When $\theta_2 < 0$ and $\dot{\theta}_2 \leq 0$, it is not possible to find a single constant of γ that take the initial state to the right half plane. However, this can be attained by switching γ as follows: First, the feedback control developed in subsection 4.4.3 is applied. The state converges and follows an elliptic manifold on the left half plane. Then, when the state enters $\theta_2 < 0$ and $\dot{\theta}_2 > 0$, the strategy in the previous paragraph can be applied. Consequently with this switching, the whole state space becomes the region of attraction of an ellipse passing θ_{2d} in the right half plane.

The similar discussions will be applied to make the elliptic family on the left half plane attractive in the whole space.

Figure 4.15 shows the result of simulation. The initial and desired positions were $\theta_{20} = -\frac{5\pi}{12}$[rad] and $\theta_{2d} = \frac{3\pi}{4}$[rad], respectively. Note that the switching in

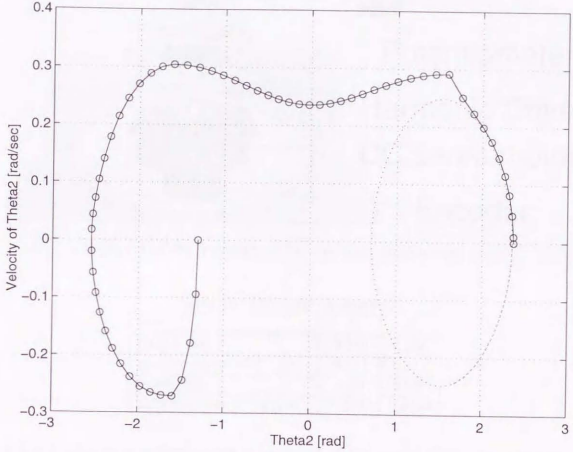

Figure 4.15: Simulation with global attraction

the left plane was done on the top of the ellipse, since it is preferable to have a sufficient momentum to travel from the left to the right passing through the $\dot{\theta}_2$ axis.

4.5 Experiments

Experiments were executed to verify the control strategy proposed in section 4.4. Figures 4.16 and 4.17 show the structure and the photograph of the 2DOF free-joint manipulator used for the experiments. The both joint axes are vertical. The first joint is actuated by a DC servo motor, while the second joint is free to move.

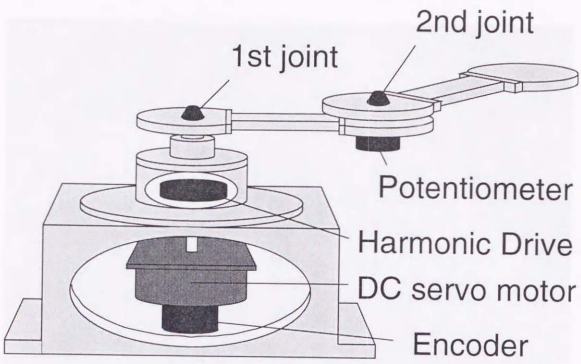

Figure 4.16: Structure of the free-joint manipulator

Table 4.1: Dynamic parameters

link	1	2
length [m]	0.240	0.240
gravity center (GC) [m]	0.111	0.111
mass [kg]	1.00	0.930
inertia about GC [kg·m^2]	0.0124	0.0115

A low-friction type potentiometer is equipped at the second joint. The dynamic parameters are summarized in Table 4.1. A high-gain velocity feedback control is designed to drive the first joint. The computed input, $\ddot{\theta}_1$, is integrated and sent to the velocity controller as a reference signal. The following values were used as the control constants: $\gamma_0 = 6.00$[rad/sec^2], $\omega = 4\pi$[rad/sec], $\theta_e = \pm 1.53$[rad], $r_\omega = 0.300$, $k_1 = 15.0$[rad/sec^2], and $k_2 = 0.500$.

Figures 4.18 and 4.19 show the results. Figure 4.18 is for the case with $\theta_{20} = 0.0$[rad] and $\theta_{2d} = -2.0$[rad], and Fig. 4.19 is for the case with $\theta_{20} = -2.0$[rad] and $\theta_{2d} = -0.0$[rad]. Due to the friction, the center point $(\theta_2, \dot{\theta}_2) = (\theta_e, 0)$ becomes a point of attraction. The convergence to elliptic manifold was not as smooth as that of Fig. 4.11 or 4.14, which is due to the effect of the point of attraction. In spite of such difficulty, thanks to the feedback control, the state finally terminated near the destinations. Note that though the point of termination shows a small

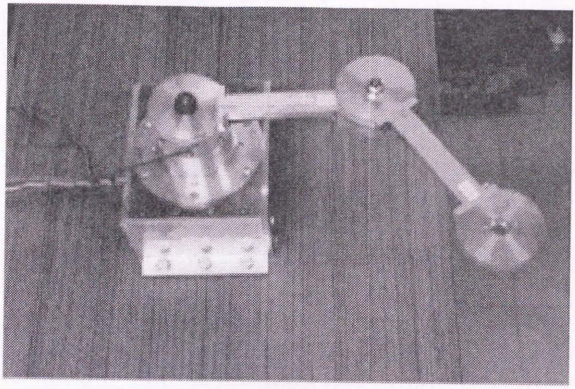

Figure 4.17: Photo of the free-joint manipulator

residual velocity in Fig. 4.19, it actually stopped in the experiment. It can be explained that (1) the residual velocity was damped out by the friction or (2) the residual velocity was due to discretization error in computing velocity from the potentiometer signal. The experimental results clearly show effectiveness of the developed positioning control strategy.

4.6 Conclusion

The nonlinear behavior of a planar 2R free-joint manipulator and its positioning control were investigated. Choosing a time-periodic input for the first joint was the fundamental strategy. When the amplitude of periodic input remained small, the Poincaré map of the behavior in the phase space formed an elliptic closed manifold. As the amplitude grew, the Poincaré map showed chaotic behaviors. A series of positioning control strategy was proposed where the amplitude modulation of the error signal was used for feedback control to a desired elliptic manifold and open-loop termination control in the neighborhood of the destination. The experiments were carried out to verify the developed positioning control strategy and clearly showed its effectiveness.

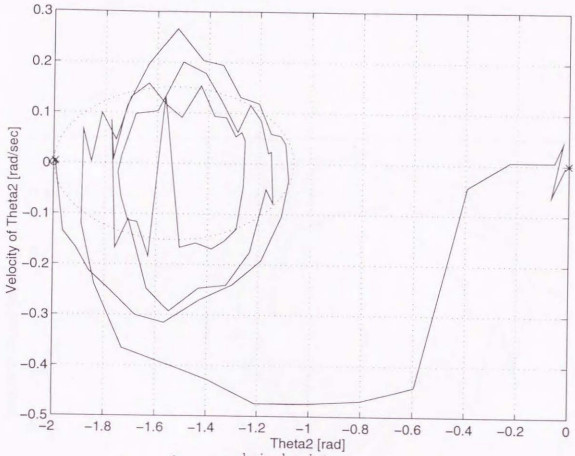

○	: desired point
∗	: initial point
×	: final point
solid line	: experimental Poincaré map
dotted line	: computed ellipse

Figure 4.18: Experiment 1: from 0[rad] to −2[rad]

Rigorous stability analysis of the feedback control designed in this chapter from heuristic observations is an important subject of future research. Extension to higher dimensional systems with more free-joints also remains in the future generalization.

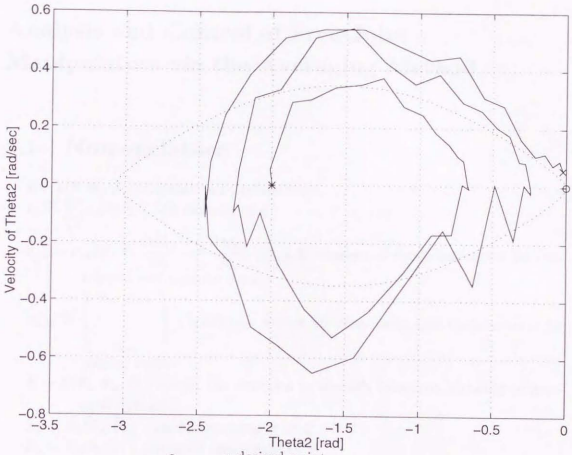

○	: desired point
∗	: initial point
×	: final point
solid line	: experimental Poincaré map
dotted line	: computed ellipse

Figure 4.19: Experiment 2: from -2[rad] to 0[rad]

Chapter 5

Analysis and Control of Free-Joint Manipulators via the Averaging Method

5.1 Nomenclature

$\boldsymbol{c} = \boldsymbol{c}(\boldsymbol{\theta}, \dot{\boldsymbol{\theta}})$; centripetal and Coriolis term

$c_i \stackrel{\text{def}}{=} \sum_{j,k} c_{ijk}\dot{\theta}_j\dot{\theta}_k$; i-th element of $\boldsymbol{c}$

$c_{ijk} = c_{ijk}(\boldsymbol{\theta}) \stackrel{\text{def}}{=} \dfrac{\partial M_{ij}}{\partial \theta_k} - \dfrac{1}{2}\dfrac{\partial M_{kj}}{\partial \theta_i}$; (i,j,k) element of coefficient tensor for centripetal and Coriolis term

$\boldsymbol{c}_{u,jk} \stackrel{\text{def}}{=} \begin{pmatrix} c_{(m+1)jk} \\ \vdots \\ c_{njk} \end{pmatrix}$; coefficient vector for centripetal and Coriolis term for passive joints

$E = E(\boldsymbol{\theta}_u, \dot{\boldsymbol{\theta}}_u; \varepsilon)$; energy-like function to identify invariant manifold of averaged dynamics

$E_k = E_k(\boldsymbol{\theta}_u, \dot{\boldsymbol{\theta}}_u)$; kinetic component of E

$E_p = E_p(\boldsymbol{\theta}_u; \varepsilon)$; potential component of E

$E_{nom} = E_{nom}(\boldsymbol{\theta}_u, \boldsymbol{\phi}_u)$; normalized energy on amplitude-normalized phase plane

$E_{nom,k} = E_{nom,k}(\boldsymbol{\theta}_u, \boldsymbol{\phi}_u)$; kinetic component of E_{nom}

$E_{nom,p} = E_{nom,p}(\boldsymbol{\theta}_u)$; potential component of E_{nom}

$E_{std} = E_{std}(\boldsymbol{\theta}_u, \dot{\boldsymbol{\theta}}_u)$; energy for standard input-amplitude

$f_T(t), g_T(t)$; periodic C^2 function with period T

J_k ; k-th column vector of $\left(\boldsymbol{M}_{uu}^{-1}\boldsymbol{M}_{ua}\right)_k$

$K \stackrel{\text{def}}{=} \dfrac{1}{T}\displaystyle\int_0^T (f_T'(t))^2\, dt$; mean square of periodic function $f_T'(t)$

k_3 ; gain for amplitude-modulation in Eq.(5.35)

L ; candidate of Lyapunov function

$\boldsymbol{M} \in \boldsymbol{R}^{n\times n}$; inertia matrix

M_{ij} ; (i,j) element of inertia matrix

$\boldsymbol{M}_{aa} \in \boldsymbol{R}^{m\times m}, \boldsymbol{M}_{ua} \in \boldsymbol{R}^{(n-m)\times m}, \boldsymbol{M}_{uu} \in \boldsymbol{R}^{(n-m)\times(n-m)}$; partitioned inertia matrices as $\boldsymbol{M} = \begin{pmatrix} \boldsymbol{M}_{a1} & \boldsymbol{M}_{ua}^T \\ \boldsymbol{M}_{ua} & \boldsymbol{M}_{uu} \end{pmatrix}$

m ; number of actuated joints

n ; number of joints or dimension of generalized coordinates

$p_i \stackrel{\text{def}}{=} \dfrac{\dot{\theta}_i}{\varepsilon}$; phase velocity of i-th joint normalized by ε

$\boldsymbol{p}_u \stackrel{\text{def}}{=} \begin{pmatrix} p_{m+1} \\ \vdots \\ p_n \end{pmatrix}$; amplitude-normalized phase velocities of passive joints

s ; scaled time

ε ; amplitude of periodic perturbation, [rad]

ε_{max} ; upper-limit of input-amplitude

ε_{new} ; lower-limit of input-amplitude

ε_{std} ; standard input-amplitude

$\boldsymbol{\theta}$; generalized coordinates

$\boldsymbol{\theta}_a \in \boldsymbol{R}^m, \boldsymbol{\theta}_u \in \boldsymbol{R}^{(n-m)}$; partitioned generalized coordinates as

$\theta_{2c} = \pm\dfrac{\pi}{2}$; center of elliptic manifold

θ_i ; i-th element of generalized coordinates or angle of i-th joint $\boldsymbol{\theta} = \begin{pmatrix} \boldsymbol{\theta}_a \\ \boldsymbol{\theta}_u \end{pmatrix}$

τ ; input-torque to the 1st joint

τ_i ; corresponding generalized force

$\tau_{rel,i}$; i-th joint torque or generalized force corresponding to the representation in relative angles

ϕ_i ; standard phase velocity corresponding to p_i

$\boldsymbol{\phi}_u \stackrel{\text{def}}{=} \begin{pmatrix} \phi_{m+1} \\ \vdots \\ \phi_n \end{pmatrix}$; standard phase velocities of passive joints

Subscripts

0 ; initial value

a ; corresponding to actuated joints

d ; desired value

new ; renewed value in next period

rel ; corresponding to the representation in relative angles

u ; corresponding to unactuated (passive) joints

Superscripts

0 ; unperturbed solution

(n) ; coordinates after n periods

o ; averaged function defined as $f^o(x) \stackrel{\text{def}}{=} \frac{1}{T}\int_0^T f(t,x)dt$

$*^{[2]}$; vector of second-order term of $*$ as $\begin{pmatrix} \vdots \\ *_i *_j \\ \vdots \end{pmatrix} (i,j = 1, \cdots n)$

$*'$; derivative of $*$

Notations of the other variables and constants conform to those in chapter 4.

5.2 Introduction

In the previous chapter, a control method of 2R free-joint manipulators to position the both joints by amplitude modulation of a periodic input was proposed. Although the method was an effective method to control such a system, it was quite heuristic and difficult to generalize. In this chapter, the averaging method, which is a suitable and powerful tool for the system with periodic inputs, is applied to free-joint manipulators. The invariant manifolds of the averaged motions of 2R free-joint manipulators with only one actuator are identified. A control method to reach the desired invariant manifold via modulation of the input amplitude is also proposed.

On control of second-order mechanical systems, Bloch et.al. [BRM92] formulated control and stabilization methods of nonholonomic dynamic systems. Baillieul [Bai93] discussed the averaging of the second-order mechanical systems such as a cart with a pendulum and analyzed the stability of its equilibrium points. Baillieul also defined an energy of the averaged system for assessing the asymptotic stability. The literature fundamentally dealt with the control theorem of a class of nonlinear systems to stabilize at an equilibrium point. A planar free-joint manipulator is a system difficult to control by the theorems in the literature since it has few stable equilibrium points and its controllability usually cannot be shown.

5.3 Formulating Manipulators with Free Joints

A multi-link system connected by free joints is an underactuated system whose dynamic constraints are not integrable. The dynamics is represented by

$$\sum_j M_{ij}\ddot{\theta}_j + \sum_{j,k} c_{ijk}\dot{\theta}_j\dot{\theta}_k = \tau_i \qquad (i = 1, \cdots, n) \tag{5.1}$$

Note that the above dynamics is with an assumption that the system resides in the horizontal plane, namely, there is no potential term in the dynamics. The

assumption is not only for simplification of formulation but also for an important property. With a potential term, each joint has a solitary equilibrium where the potential becomes minimal or maximal, namely, the joint directs perpendicularly up or down. On the other hand without the potential, every joint can be settled at any configuration which enlarges options to position the underactuated manipulator. When θ_i is defined by the relative angle of the i-th joint, τ_i denotes the i-th joint torque itself. In the other case that with the absolute angle, τ_i is represented by $\tau_i = \tau_{rel,i} - \tau_{rel,i+1}$.

Simply assume that the first joint is only actuated and the other joints are free joints, namely $m = 1$, which yields simplification as $\tau_1 = \tau, \tau_i = 0 (i \geq 2)$. Consider the input to the first joint as a periodic perturbation such as

$$\begin{aligned} \theta_1 &= \theta_{10} + \varepsilon f_T(t) \\ \dot{\theta}_1 &= \varepsilon f_T'(t) \\ \ddot{\theta}_1 &= \varepsilon f_T''(t) \end{aligned} \tag{5.2}$$

If the perturbed system is periodic, a powerful analytic approximating method, the *averaging method*, will be able to be applied. The theorem for averaging of a periodic system is quoted in the appendix D.1. To apply the averaging method, the system must be in the *standard form* such as:

$$\dot{\boldsymbol{x}} = \epsilon \boldsymbol{f}(t, \boldsymbol{x}) + \epsilon^2 \boldsymbol{g}(t, \boldsymbol{x}; \epsilon)$$

Otherwise, the following reformulation in the standard form [SV85] has to be executed:

Let a perturbed system be in the form as:

$$\dot{\boldsymbol{x}} = \boldsymbol{f}^0(t, \boldsymbol{x}) + \epsilon \boldsymbol{f}(t, \boldsymbol{x}; \epsilon) \tag{5.3}$$

with an initial condition $\boldsymbol{x}(t_0) = \boldsymbol{x}_0$, and its unperturbed problem, namely that with $\epsilon = 0$, as:

$$\dot{\boldsymbol{x}}^0 = \boldsymbol{f}^0(t, \boldsymbol{x}^0) \tag{5.4}$$

Assume that Eq.(5.4) can be solved explicitly. The solution is regarded as to depend on the initial condition and is represented as:

$$\boldsymbol{x}^0 = \boldsymbol{x}^0(t, \boldsymbol{\xi}), \qquad \boldsymbol{x}^0(0, \boldsymbol{\xi}) = \boldsymbol{\xi}, \qquad \boldsymbol{\xi} \in \boldsymbol{R}^n$$

The above unperturbed solution can be regarded as a transformation as:

$$\boldsymbol{x} = \boldsymbol{x}^0(t, \boldsymbol{\xi}) \tag{5.5}$$

Then, the following differential equation for $\boldsymbol{\xi}$ is obtained from Eqs.(5.3) and (5.4):

$$\frac{\partial \boldsymbol{x}^0}{\partial t} + \frac{\partial \boldsymbol{x}^0}{\partial \boldsymbol{\xi}} \frac{d\boldsymbol{\xi}}{dt} = \boldsymbol{f}^0(t, \boldsymbol{x}^0) + \epsilon \boldsymbol{f}(t, \boldsymbol{x}^0; \epsilon)$$

Since $\boldsymbol{x}^0$ *satisfies Eq.(5.4), the first terms of both sides are canceled out. Assume* $\dfrac{\partial \boldsymbol{x}^0}{\partial \boldsymbol{\xi}}$ *is nonsingular, then we have*

$$\dot{\boldsymbol{\xi}} = \epsilon \left(\frac{\partial \boldsymbol{x}^0(t, \boldsymbol{\xi})}{\partial \boldsymbol{\xi}} \right)^{-1} \boldsymbol{f}(t, \boldsymbol{x}^0(t, \boldsymbol{\xi}); \epsilon) \tag{5.6}$$

The above equation supplemented by the initial value of $\boldsymbol{\xi}$ *will be called a "perturbation problem in the standard form."* □

More precise discussion will be found in [SV85].

However, the transformation for the underactuated system is not as explicit as above. The considered system is represented as:

$$\begin{aligned} \dot{\boldsymbol{\theta}}_u &= \dot{\boldsymbol{\theta}}_u \\ \dot{\boldsymbol{\theta}}_u &= -\boldsymbol{M}_{uu}^{-1}\boldsymbol{M}_{ua}\varepsilon f_T'' \\ &\quad -\boldsymbol{M}_{uu}^{-1}\left(\boldsymbol{c}_{u,11}\varepsilon^2 {f_T'}^2 + \sum_{k\geq 2}(\boldsymbol{c}_{u,1k} + \boldsymbol{c}_{u,k1})\dot{\theta}_k \varepsilon f_T'(t) + \sum_{j,k\geq 2} \boldsymbol{c}_{u,jk}\dot{\theta}_j\dot{\theta}_k \right) \end{aligned} \tag{5.7}$$

with partitioned inertia matrices corresponding to actuated joints and passive joints. Transformation to the standard form derived from the unperturbed solution figured out directly from the above form as

$$\begin{aligned} \dot{\boldsymbol{\theta}}_u^0 &= \dot{\boldsymbol{\theta}}_u^0 \\ \dot{\boldsymbol{\theta}}_u^0 &= -\boldsymbol{M}_{uu}^{-1} \sum_{j,k\geq 2} \boldsymbol{c}_{u,jk}\dot{\theta}_j\dot{\theta}_k \end{aligned}$$

would not yield an appropriate standard form to which the averaging theorem can be applied. Then, a substitution as

$$p_i = \frac{\dot{\theta}_i}{\varepsilon}, \qquad i = 2, \cdots, n \tag{5.8}$$

should be introduced and the following averaging procedure of the system cannot be developed without the substitution. With this substitution, the system (5.1) is transformed to a perturbed system as:

$$\begin{aligned} \dot{\boldsymbol{\theta}}_u &= \varepsilon \boldsymbol{p}_u \\ \dot{\boldsymbol{p}}_u &= -\boldsymbol{M}_{uu}^{-1}\boldsymbol{M}_{ua} f_T'' \\ &\quad -\varepsilon \boldsymbol{M}_{uu}^{-1}\left(\boldsymbol{c}_{u,11} {f_T'}^2 + \sum_{k\geq 2}(\boldsymbol{c}_{u,1k} + \boldsymbol{c}_{u,k1}) p_k f_T'(t) + \sum_{j,k\geq 2} \boldsymbol{c}_{u,jk} p_j p_k \right) \end{aligned} \tag{5.9}$$

Then, the unperturbed problem of Eq.(5.9) is obtained as

$$\begin{aligned} \dot{\boldsymbol{\theta}}_u &= 0 \\ \dot{\boldsymbol{p}}_u &= -\boldsymbol{M}_{uu}^{-1}\boldsymbol{M}_{ua} f_T'' \end{aligned} \tag{5.10}$$

and the unperturbed solution is as

$$\begin{aligned} \boldsymbol{\theta}_u &= \boldsymbol{\theta}_{u0} \\ \boldsymbol{p}_u &= \boldsymbol{p}_{u0} - \boldsymbol{M}_{uu}^{-1}\boldsymbol{M}_{ua}f_T'(t) \end{aligned}$$

which yields the following transformation into the standard form:

$$\begin{aligned} \boldsymbol{\theta}_u &= \boldsymbol{\theta}_u \\ \boldsymbol{p}_u &= \boldsymbol{\phi}_u - \boldsymbol{M}_{uu}^{-1}\boldsymbol{M}_{ua}f_T'(t) \end{aligned} \tag{5.11}$$

Then, Eq.(5.9) is reformulated into the standard form as:

$$\begin{aligned} \dot{\boldsymbol{\theta}}_u &= \varepsilon\left(\boldsymbol{\phi}_u - \boldsymbol{M}_{uu}^{-1}\boldsymbol{M}_{ua}f_T'\right) \\ \dot{\boldsymbol{\phi}}_u &= \varepsilon\boldsymbol{M}_{uu}^{-1}\left(\sum_{j,k\geq 2}\left(\frac{1}{2}\frac{\partial M_{kj}}{\partial\theta_i}+\frac{\partial M_{ij}}{\partial\theta_k}\right)\phi_j\phi_k\right. \\ &\quad +\sum_{k\geq 2}\left(\frac{\partial M_{1k}}{\partial\theta_i}+\frac{\partial M_{ik}}{\partial\theta_1}-\sum_{j\geq 2}\left(\frac{\partial M_{jk}}{\partial\theta_i}+\frac{\partial M_{ik}}{\partial\theta_j}\right)J_j\right)\phi_k f_T' \\ &\quad \left.+\left(\frac{1}{2}\frac{\partial M_{11}}{\partial\theta_i}-\sum_{k\geq 2}\frac{\partial M_{1k}}{\partial\theta_i}J_k+\frac{1}{2}\sum_{j,k\geq 2}\frac{\partial M_{jk}}{\partial\theta_i}J_jJ_k\right)f_T'^2\right) \end{aligned} \tag{5.12}$$

The standard form implies the Poincaré map of the non-averaged system with the period of the input [Wig90]. Approximated dynamics of the system (5.12) is obtained by averaging as:

$$\begin{aligned} \dot{\bar{\boldsymbol{\theta}}}_u &= \varepsilon\bar{\boldsymbol{\phi}}_u \\ \dot{\bar{\boldsymbol{\phi}}}_u &= \varepsilon\boldsymbol{M}_{uu}^{-1}\left(\sum_{j,k\geq 2}\left(\frac{1}{2}\frac{\partial M_{kj}}{\partial\theta_i}+\frac{\partial M_{ij}}{\partial\theta_k}\right)\bar{\phi}_j\bar{\phi}_k\right. \\ &\quad \left.+K\left(\frac{1}{2}\frac{\partial M_{11}}{\partial\theta_i}-\sum_{k\geq 2}\frac{\partial M_{k1}}{\partial\theta_i}J_k+\frac{1}{2}\sum_{j,k\geq 2}\frac{\partial M_{kj}}{\partial\theta_i}J_jJ_k\right)\right) \end{aligned} \tag{5.13}$$

The averaged system will be simplified by the transformation of the time scale, $s=\varepsilon t$, as

$$\frac{d}{ds}\begin{pmatrix}\boldsymbol{\theta}_u\\ \boldsymbol{\phi}_u\end{pmatrix} = \begin{pmatrix}\boldsymbol{\phi}_u\\ \boldsymbol{f}(\boldsymbol{\theta}_u)\boldsymbol{\phi}_u^{[2]}+K\boldsymbol{g}(\boldsymbol{\theta}_u)\end{pmatrix} \tag{5.14}$$

The equation represents an autonomous system without the perturbation amplitude ε. This implies that the feature of the behavior with a small perturbation is determined by the averaged dynamics independently of ε. Since it is necessary to discuss the characteristic of the solution trajectory of the averaged dynamics concretely, control problems of 2R free-joint manipulators are presented in the following sections.

5.4 Analysis of 2R Free-Joint Manipulators via the Averaging Method

5.4.1 Averaged dynamics of 2R free-joint manipulators

The dynamics of 2R free-joint manipulators as shown in Chap. 4 to be analyzed is as

$$\frac{d}{dt}\begin{pmatrix}\theta_1\\ \theta_2\\ \dot{\theta}_1\\ \dot{\theta}_2\end{pmatrix} = \begin{pmatrix}\dot{\theta}_1\\ \dot{\theta}_2\\ \ddot{\theta}_1\\ -(1+\mu\cos\theta_2)\ddot{\theta}_1 - \mu\sin\theta_2\cdot(\dot{\theta}_1)^2\end{pmatrix} \tag{5.15}$$

where θ_i is defined as a relative angle of the i-th joint.

With the periodic input and the substitution as in the previous section, the system is represented by the following equation only for the second joint.

$$\begin{aligned}\dot{\theta}_2 &= \varepsilon p_2\\ \dot{p}_2 &= -(1+\mu\cos\theta_2)f_T''(t) - \varepsilon\mu\sin\theta_2\cdot(f_T'(t))^2\end{aligned} \tag{5.16}$$

Since its unperturbed solution is

$$\begin{aligned}\theta_2 &= \theta_{20}\\ p_2 &= p_{20} - (1+\mu\cos\theta_{20})f_T'(t),\end{aligned}$$

the transformation is given by

$$\phi_2 = p_2 + (1+\mu\cos\theta_2)f_T'(t) \tag{5.17}$$

The standard form is obtained from Eqs.(5.16) and (5.17) as

$$\begin{aligned}\dot{\theta}_2 &= \varepsilon(\phi_2 - (1+\mu\cos\theta_2)f_T'(t))\\ \dot{\phi}_2 &= \varepsilon\left(-\mu\phi_2\sin\theta_2\cdot f_T'(t) + \frac{\mu^2}{2}\sin 2\theta_2\cdot(f_T'(t))^2\right)\end{aligned} \tag{5.18}$$

The averaged system is obtained from Eq.(5.18) as

$$\begin{aligned}\dot{\bar{\theta}}_2 &= \varepsilon\bar{\phi}_2\\ \dot{\bar{\phi}}_2 &= \varepsilon\frac{K\mu^2}{2}\sin 2\bar{\theta}_2\end{aligned} \tag{5.19}$$

The solution of Eq.(5.19) is completely described by the *Jacobian elliptic functions* [SV85], $\mathrm{am}(u,k)$ and $\mathrm{sn}(u,k)$, as

$$\bar{\theta}_2 = \begin{cases}\mathrm{am}\,(at+C_2,k) - \dfrac{\pi}{2} & (0<k<1)\\ \sin^{-1}\left(\dfrac{1}{k}\mathrm{sn}\left(-kat - kC_2, \dfrac{1}{k}\right)\right) - \dfrac{\pi}{2} & (k>1)\\ \sin^{-1}\left(\tanh\left(at+C_2\right)\right) - \dfrac{\pi}{2} & (k=1)\end{cases} \tag{5.20}$$

where $a = \frac{\varepsilon\omega\mu}{\sqrt{2}k}$, $C_2 = \int_0^{\theta_{20}+\frac{\pi}{2}} \frac{dz}{\sqrt{1-k^2\sin^2 z}}$, $k = \sqrt{\frac{2}{1+C_1}}$ and $C_1 = \cos 2\theta_{20} + \left(\frac{2\dot{\theta}_{20}}{\mu}\right)^2$, and $\theta = \mathrm{am}(u,k)$ is called the *amplitude function* defined as an implicit function by:

$$\int_0^{\theta} \frac{dz}{\sqrt{1-k^2\sin^2 z}} = u \tag{5.21}$$

and $\mathrm{sn}(u,k) \stackrel{\mathrm{def}}{=} \sin(\mathrm{am}(u,k))$. Although one might think the above solution trajectory is complicated and difficult to describe, the solution simply follows a trajectory on the plane of $\bar{\theta}_2$ and $\bar{\phi}_2$ as

$$\bar{\phi}_2^2 + K\mu^2\left(\cos\bar{\theta}_2\right)^2 = \text{const.} \tag{5.22}$$

The above equation implies that the trajectory is on a time-invariant manifold uniquely determined by the initial configuration independently of ε. Since the velocity of the second joint is denoted by $\dot{\bar{\theta}}_2 = \varepsilon\bar{\phi}_2$, the trajectory in the phase plane of the second joint is stretched and shrunken proportionally to ε in the vertical direction of $\bar{\theta}_2$. In Chap. 4, it is observed that the Poincaré map of the system follows an ordered closed trajectory like ellipse in the case where the input amplitude is small, and that the elliptic trajectory is stretched and shrunken by modulating the input amplitude. The above discussion and Fig. 5.2 analytically explains the observation obtained from computer simulations and experiments.

Figures 5.1 and 5.2 show the simulated behaviors of the 2R free-joint manipulator and the behavior of its averaged dynamics, respectively. The figures are represented by the Poincaré map [Wig90] of the trajectory with the period T for the cases that the periodic input is $f_T(t) = 1 - \cos\omega t$ with $\varepsilon = 0.04$, $\omega = 4\pi$ and various values of $(\theta_2, \dot{\theta}_2)$ as the initial configurations. Invariability of manifolds of the averaged dynamics on the phase plane is discussed from a viewpoint of energy in the next subsection.

5.4.2 Conservation of the averaged dynamics

Considering Eq.(5.19), the averaged system has two center equilibrium points, $(\bar{\theta}_2, \bar{\phi}_2) = \left(\pm\frac{\pi}{2}, 0\right)$, and two saddle points, $(\bar{\theta}_2, \bar{\phi}_2) = (0,0), (\pi, 0)$. For another each destination such that $\bar{\phi}_2 = 0$, there is a corresponding invariant manifold, which is represented by Eq.(5.22), and it passes through the point and turns around one of the center points.

Considering the equation (5.22), an energy-like function can be defined as

$$E(\theta_2, \dot{\theta}_2; \varepsilon) \stackrel{\mathrm{def}}{=} \frac{1}{2}\dot{\theta}_2^2 + \frac{1}{2}\varepsilon^2 K\mu^2\cos^2\theta_2 \tag{5.23}$$

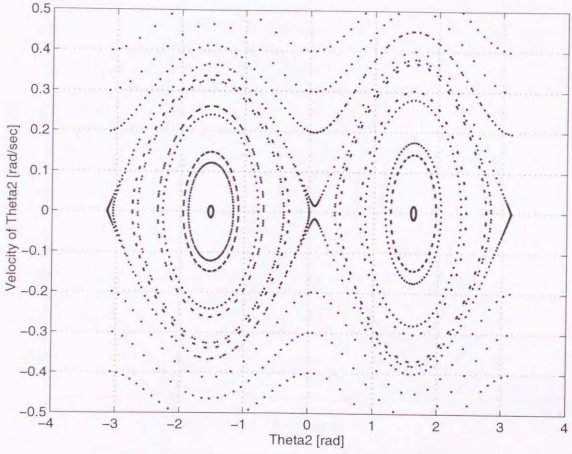

Figure 5.1: Simulated trajectories of the 2R-FJM

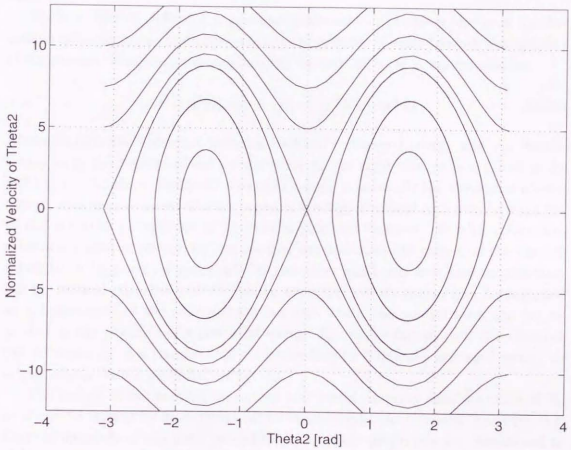

Figure 5.2: Averaged motions of the 2R-FJM

which denotes an identifier of the invariant manifold represented by Eq.(5.22). For a constant value of ε, E is conserved for the averaged system. The energy E consists of two components, namely, a kinetic component, $E_k = E_k(\dot{\theta}_2) \stackrel{\text{def}}{=} \frac{1}{2}\dot{\theta}_2^2$, and a potential component, $E_p = E_p(\theta_2; \varepsilon) \stackrel{\text{def}}{=} \frac{1}{2}\varepsilon^2 K\mu^2 \cos^2\theta_2$. It is natural to regard E_k and E_p as a kind of kinetic energy and potential energy and to regard E as a kind of Hamiltonian as $E = E_k + E_p$. Then, it can be concluded that the averaged system (5.19) is a kind of Hamiltonian conserved system for a constant value of ε.

Baillieul [Bai93] defined the *averaged potential* and *averaged energy* in his discussion of averaging second-order mechanical systems in order to show the stability of the motion. Baillieul's averaged energy for our 2R FJM is represented as

$$\bar{E} = \bar{E}(\theta_2, \dot{\theta}_2) = \frac{1}{2}\dot{\theta}_2^2 - \frac{1}{2}\varepsilon^2 K\mu^2 \cos^2\theta_2 \tag{5.24}$$

Although only the difference between Baillieul's averaged energy and our Hamiltonian is in the signum of the second term in the right side, it is a pretty great difference. The above Baillieul's averaged energy is naturally the average of kinetic energy, and never conserved with periodic forcing. Baillieul also noticed that the second term can be regarded as a potential quantity. However, since his system has a natural potential energy, he just merged the potential-like term into the natural potential in his *averaged potential*. On the other hand, our free-joint manipulator has no natural potential and the above averaged kinetic energy can be regarded as a Lagrangian of the averaged system and, then, the second term can be regarded as the negative of a potential energy E_p. Consequently, our Hamiltonian can be regarded as a Hamiltonian corresponding to Baillieul's averaged energy as a Lagrangian with a potential energy E_p.

The energy E has another important and useful property that the value of E_p or E can be altered by modulation of the input-amplitude ε at same point $(\theta_2, \dot{\theta}_2)$. Control methods of the both two joints using these properties are formulated in the following subsections.

5.5 Control of 2R Free-Joint Manipulators via Averaging Method

In Chap.4, a control strategy to position the both joints of 2R FJM was proposed as; *(1) Control the actuated first joint to the desired position regardless of the passive second joint, (2) Steer the second joint to the desired position by periodic actuation of the first joint.* The second subgoal is realized by dividing the control

into the following two phases; *(2-1) Stabilize the second joint onto an invariant manifold on the phase plane which passes through the destination, (2-2) Terminate the second joint at the destination when it enters the neighborhood of the destination.* Each control was realized by modulation of the input-amplitude in Chap.4. However, the proposed method was heuristically constructed from observations of simulations without mathematical proof and difficult to generalize. In this section, reformulation of the control method of (2-1) is developed using the energy of the averaged dynamics proposed in the previous section.

5.5.1 Control by amplitude-normalized energy

The system follows an invariant manifold of Eq.(5.22) and conserves the energy of Eq.(5.23) for a constant input-amplitude, and the manifold and energy can be modulated by modulation of the input-amplitude. The energy E can be rewritten in the 2nd joint's phase plane of the non-averaged system, $(\theta_2, \dot{\theta}_2)$, as

$$E(\theta_2, \dot{\theta}_2; \varepsilon) = \frac{1}{2}\varepsilon^2 \left({p_2}^2 + K\mu^2 (\cos\theta_2)^2 \right) \tag{5.25}$$

where $p_2 \stackrel{\text{def}}{=} \dfrac{\dot{\theta}_2}{\varepsilon}$. Considering that E is represented as a function of θ_2 and p_2, a normalized energy can be redefined as

$$E_{nom}(\theta_2, p_2) \stackrel{\text{def}}{=} E_{nom,k} + E_{nom,p} \tag{5.26}$$

where $E_{nom,k} \stackrel{\text{def}}{=} \dfrac{1}{2}{p_2}^2$ and $E_{nom,p} \stackrel{\text{def}}{=} \dfrac{1}{2}K\mu^2(\cos\theta_2)^2$ denote its kinetic and potential components, respectively. Note that the normalized energy is defined on a plane of θ_2 and p_2. Then, p_2 is termed an *amplitude-normalized velocity* of the second joint and the plane (θ_2, p_2) is called an *amplitude-normalized phase plane*. On the amplitude-normalized phase plane, the shapes of the manifolds of averaged dynamics and E_{nom} are maintained independently of ε. Though, since p_2 is defined as $\dfrac{\dot{\theta}_2}{\varepsilon}$, the value of p_2 and E_{nom} can be modulated into another value by amplitude modulation as

$$p_2 \mapsto p_{2new} = \left(\frac{\dot{\theta}_2}{\varepsilon_{new}} \right) = \left(\frac{\varepsilon}{\varepsilon_{new}} \right) p_2 \tag{5.27}$$

and

$$E \mapsto E_{new} = \left(\frac{\dot{\theta}_2}{\varepsilon_{new}} \right)^2 + K\mu^2(\cos\theta_2)^2 \tag{5.28}$$

The modulation of the input amplitude modifies only the kinetic component, whereas the potential component is invariant for ε. The modulation algorithm is obtained from Eq.(5.28) as

$$\varepsilon \mapsto \varepsilon_{new} = \varepsilon \cdot \sqrt{\frac{E_{nom,k} - E_{nom,kd}}{E_{nom,pd} - E_{nom,p}}} = \sqrt{\frac{\dot{\theta}_2^2 - \dot{\theta}_{2d}^2}{E_{pd} - E_p}} \tag{5.29}$$

When the value in the square root isn't negative or zero and ε_{new} has a real value, the normalized energy can be obtained as

$$E_{nom} = \frac{1}{2}\left(\frac{\dot{\theta}_{2d}}{\varepsilon_{new}}\right)^2 + \frac{1}{2}K\mu^2\cos^2\theta_{2d} \tag{5.30}$$

The position on the amplitude-normalized phase plane $(\bar{\theta}_2, \bar{p})$ jumps immediately to $\left(\bar{\theta}_2, \frac{\dot{\bar{\theta}}_2}{\varepsilon_{new}}\right)$ on an invariant manifold which passes through the destination. The modulation is executed only when the value in the square root is positive or zero. Since $\dot{\theta}_{2d}$ is usually set at zero for positioning, the case implies that $E_p < E_{pd}$, namely, $|\bar{\theta}_2 - \theta_{2e}| < |\bar{\theta}_{2d} - \theta_{2e}|$ where $\theta_e = \pm\frac{\pi}{2}$ denotes the center of the elliptic invariant manifolds.

5.5.2 Lyapunov control to a manifold

Set a standard input-amplitude ε_{std} and redefine the energy for the standard amplitude as:

$$E_{std}(\theta_2, \dot{\theta}_2) \stackrel{\text{def}}{=} \frac{1}{2}\dot{\theta}_2^2 + \frac{1}{2}{\varepsilon_{std}}^2 K\mu^2\cos^2\theta_2 \tag{5.31}$$

The energy is conserved when the input-amplitude settles at ε_{std}. If the input-amplitude is not at ε_{std}, the energy E_{std} is never conserved as:

$$\dot{E}_{std} = \frac{1}{2}K\mu^2({\varepsilon}^2 - {\varepsilon_{std}}^2)\sin 2\theta_2 \cdot \dot{\theta}_2 \tag{5.32}$$

Define a candidate of Lyapunov function as

$$L = \frac{1}{2}(E_{std} - E_d)^2 \tag{5.33}$$

where $E_d = E_{std}(\theta_{2d}, \dot{\theta}_{2d})$. Its derivative is obtained from Eq.(5.32) as:

$$\dot{L} = \frac{1}{2}K\mu^2({\varepsilon}^2 - {\varepsilon_{std}}^2)(E_{std} - E_d)\sin 2\theta_2 \cdot \dot{\theta}_2 \tag{5.34}$$

A modulation algorithm is designed as:

$$\varepsilon \mapsto \varepsilon_{new} = \begin{cases} \varepsilon_{std} \cdot \sqrt{1 - k_3(E_{std} - E_d)\sin 2\theta_2 \cdot \dot{\theta}_2} & ; \quad k_3(E_{std} - E_d)\sin 2\theta_2 \cdot \dot{\theta}_2 < 1 \\ 0 & ; \quad k_3(E_{std} - E_d)\sin 2\theta_2 \cdot \dot{\theta}_2 \geq 1 \end{cases} \tag{5.35}$$

With this amplitude-modulation, the time-derivative of the Lyapunov candidate is negative semi-definite as:

$$\dot{L} = -\frac{1}{2}k_3 K\mu^2 \varepsilon_{std}{}^2 (E_{std} - E_d)^2 \sin^2 2\theta_2 \cdot \dot{\theta}_2^2 \leq 0 \tag{5.36}$$

Note that $\dot{L}$ turns into zero for the cases that $\theta_2 = 0, \pm\frac{\pi}{2}, \pm\pi$ or $\dot{\theta}_2 = 0$. In these cases, the algorithm sets the input-amplitude as $\varepsilon = \varepsilon_{std}$ and, then, any states except for the cases at $(\theta_2, \dot{\theta}_2) = (0,0), \left(\pm\frac{\pi}{2}, 0\right), (\pm\pi, 0)$ are variant and the Lyapunov candidate stays asymptotically stable. The states $(\theta_2, \dot{\theta}_2) = (0,0), (\pm\pi, 0)$ are saddle points and each of them has unstable heteroclinic manifolds and, then, the system practically never stays at these points. The states $(\theta_2, \dot{\theta}_2) = \left(\pm\frac{\pi}{2}, 0\right)$ are center points and can be attractive by Iwamoto's method [NIY95] or friction as mentioned below. These points are actually difficult to be left but can be avoided to draw near by preserving the energy E_{std} enough large. Consequently, the proposed Lyapunov candidate is proved to be asymptotically stable almost globally except for the point $(\theta_2, \dot{\theta}_2) = \left(\pm\frac{\pi}{2}, 0\right)$.

The amplitude modulation (5.35) is executed just at each end of the period of the first joint since the values of θ_2 and $\dot{\theta}_2$ in the amplitude modulation are based on the averaged ones and non-averaged ones extremely diverge from them in the middle of the period. If the input-amplitude is modulated within the period, the motion of the first joint is no longer periodic which is the indispensable assumption and, then, the above discussion turns into meaningless. However this restriction for amplitude modulation makes the control method discontinuous, the stride of the Poincaré map is enough small for an appropriate ε_{std} and the actuation of the first joint is continuous and, then, the variation of the energy and Lyapunov candidate can be approximated as $\Delta E_{std} \simeq \dot{E}_{std} T$ and $\Delta L \simeq (E_{std} - E_d)\dot{E}_{std} T$, and the proposed algorithm is still valid. Additionally, ε is practically limited to be less than or equal to ε_{max} to guarantee the approximation of averaging and the treatment occurs no problem.

Although the amplitude-modulation proposed in this subsection and the previous seems to be a kind of energy feedback control, there is difference that the control is discontinuous and the energy is imaginary value. From a viewpoint to modify the manifold of the system by modulation of a parameter ε, the control method is related to the famous OGY method [OGY90] in control of chaos. However, there is also difference that the destination has no stable manifold and the manifold is a center manifold, while the OGY method carried the system onto a stable manifold converging to the desired equilibrium which is usually a saddle point.

About the subsequent procedure to the convergence to the desired manifold, that is, termination at the destination, the method was already provided in Chap. 4 and is reformulated by averaging analyses in the followings. In the next subsection, second-order averaging analysis is developed to approximate the Poincaré map better, and a termination control is reformulated based on the second-order averaging subsequently.

5.5.3 Better approximation by second-order averaging

Although the precedent first-order averaging analysis is sufficient to obtain dynamical comprehension of nonlinear behaviors of the system, its order of approximation is ε and is not enough accurate as seen in Fig. 5.1 and 5.2. It influences control design, especially termination control at the destination subsequently developed. Then, second-order averaging is introduced to improve the approximation. Theorem for second-order averaging is quoted in the appendix D.2. The standard form of Eq.(5.18) is approximated by second-order averaging as the followings. Let $f_T = 1 - \cos\omega t$, we have

$$\boldsymbol{y}^1 = \begin{pmatrix} (1+\mu\cos\theta_2)\cos\omega t \\ \mu\phi_2 \sin\theta_2 \cos\omega t - \dfrac{\mu^2\omega}{8}\sin 2\theta_2 \sin 2\omega t \end{pmatrix} \tag{5.37}$$

$$\boldsymbol{f}^1 = \begin{pmatrix} f_1^1 \\ f_2^1 \end{pmatrix} \tag{5.38}$$

where

$$f_1^1 = 2\mu\phi_2 \sin\theta_2 \cos\omega t + \frac{\mu\omega}{2}\sin\theta_2 \sin 2\omega t + \frac{\mu^2\omega}{8}\sin 2\theta_2 \sin 2\omega t$$

$$\begin{aligned} f_2^1 \;=\; & -\mu{\phi_2}^2 \cos\theta_2 \cos\omega t - \frac{\mu\omega}{2}\phi_2 \cos\theta_2 \sin 2\omega t \\ & -\frac{\mu^2\omega}{4}\phi_2(2-\cos 2\theta_2)\sin 2\omega t + \frac{\mu^2\omega^2}{4}\cos 2\theta_2(\cos\omega t - \cos 3\omega t) \\ & +\frac{\mu^3\omega^2}{32}(\cos\theta_2 + 7\cos 3\theta_2)\cos\omega t - \frac{\mu^3\omega^2}{32}(5\cos\theta_2 + 3\cos 3\theta_2)\cos 3\omega t \end{aligned}$$

Since the averages of $f^1(\boldsymbol{x}, t)$ are $f_1^{1o} = 0$ and $f_2^{1o} = 0$, namely, $f^{1o}(x) \equiv \mathbf{o}$, second-order averaged dynamics is obtained similarly to Eq.(5.19) with slight difference in transformation to the original dynamics as:

$$\begin{aligned} \theta_2 &= \bar{\theta}_2 + \varepsilon(1+\mu\cos\bar{\theta}_2)\cos\omega t + O(\varepsilon^2) \\ \phi_2 &= \bar{\phi}_2 + \varepsilon\mu\bar{\phi}_2 \sin\bar{\theta}_2 \cos\omega t - \varepsilon\frac{\mu^2\omega}{8}\sin 2\bar{\theta}_2 \sin 2\omega t + O(\varepsilon^2) \end{aligned} \tag{5.39}$$

The state every after period is obtained as:

$$\begin{aligned}\theta_2(nT) &= \bar{\theta}_2 + \varepsilon(1+\mu\cos\bar{\theta}_2) + O(\varepsilon^2)\\ \dot{\theta}_2(nT) &= \dot{\bar{\theta}}_2 + \varepsilon\mu\dot{\bar{\theta}}_2\sin\bar{\theta}_2 + O(\varepsilon^3)\end{aligned} \tag{5.40}$$

It shows that the error of Eq.(5.19) is not only first order of ε but also can be second order of ε in the second-order averaging.

5.5.4 Termination control via second-order averaging

In this subsection, formulation of a termination control at the destination is developed based upon the above averaging analysis. Derivation of the approximating equation is much easier in averaging context than that in 4.4.4. The results in the previous subsection shows that the averaged dynamics in Eq.(5.19) approximates the motion in an order of ε^2. Expansion of the averaged dynamics with $K = \dfrac{\omega^2}{2}$

$$\ddot{\bar{\theta}}_2 = \varepsilon^2\frac{\mu^2\omega^2}{4}\sin 2\bar{\theta}_2$$

around a point after n periods

$$\left(\bar{\theta}_2^{(n)}, \dot{\bar{\theta}}_2^{(n)}\right) = (\bar{\theta}_2, \dot{\bar{\theta}}_2)\Big\|_{t=nT}$$

is obtained as:

$$\ddot{\bar{\theta}}_2 = \varepsilon^2\frac{\mu^2\omega^2}{4}\sin 2\bar{\theta}_2^{(n)} + \varepsilon^2\frac{\mu^2\omega^2}{2}\cos 2\bar{\theta}_2^{(n)}\cdot\Delta\bar{\theta}_2 + O(\varepsilon^2\Delta\bar{\theta}_2{}^2) \tag{5.41}$$

Assume that $\ddot{\bar{\theta}}_2$ is sufficiently small to be $\dot{\bar{\theta}}_2 = O(\varepsilon^2)$, it is considered that

$$\Delta\bar{\theta}_2 = \int_0^t \ddot{\bar{\theta}}_2 dt = O(\varepsilon^2)$$

Integrating Eq.(5.41) from $t = nT$ to $(n+1)T$ yields:

$$\begin{aligned}\dot{\bar{\theta}}_2 &= \dot{\bar{\theta}}_2^{(n)} + \varepsilon^2\frac{\mu^2\omega^2}{4}\sin 2\bar{\theta}_2^{(n)}\cdot T + \varepsilon^2\frac{\mu^2\omega^2}{2}\cos 2\bar{\theta}_2^{(n)}\cdot O(\varepsilon^2) + O(\varepsilon^6)\\ &= \dot{\bar{\theta}}_2^{(n)} + \varepsilon^2\frac{\mu^2\omega}{4}\sin 2\bar{\theta}_2^{(n)}\cdot T + O(\varepsilon^4)\end{aligned} \tag{5.42}$$

Considering Eq.(5.40), the approximation error is concluded to be $O(\varepsilon^3)$. Therefore, the state $(\bar{\theta}_2, \dot{\bar{\theta}}_2)$ after a period when $\dot{\bar{\theta}}_2$ is sufficiently small is estimated as

$$\begin{aligned}\bar{\theta}_2^{(n+1)} &= \bar{\theta}_2^{(n)} + \dot{\bar{\theta}}_2^{(n)}T + \varepsilon^2\frac{\mu^2\omega^2}{4}\sin 2\bar{\theta}_2^{(n)}\cdot\frac{T^2}{2} + O(\varepsilon^3) = \bar{\theta}_2^{(n)} + O(\varepsilon^2)\\ \dot{\bar{\theta}}_2^{(n+1)} &= \dot{\bar{\theta}}_2^{(n)} + \varepsilon^2\frac{\pi\mu^2\omega}{2}\sin 2\bar{\theta}_2^{(n)} + O(\varepsilon^3)\end{aligned} \tag{5.43}$$

and considering Eq.(5.40) it is obtained that

$$\begin{aligned}\theta_2^{(n+1)} &= \bar{\theta}_2^{(n+1)} + \varepsilon(1 + \mu\cos\bar{\theta}_2^{(n+1)}) + O(\varepsilon^2)\\ \dot{\theta}_2^{(n+1)} &= \dot{\bar{\theta}}_2^{(n+1)} + \varepsilon\mu\dot{\bar{\theta}}_2^{(n+1)}\sin\bar{\theta}_2^{(n+1)} + O(\varepsilon^3) = \dot{\bar{\theta}}_2^{(n+1)} + O(\varepsilon^3)\end{aligned} \tag{5.44}$$

Consequently, the desired input-amplitude ε_d so as to make $\dot{\theta}_2^{(n+1)} = 0$ is obtained as

$$\varepsilon_d = \sqrt{\frac{-2\dot{\bar{\theta}}_2^{(n)}}{\pi\mu^2\omega\sin 2\bar{\theta}_2^{(n)}}} \tag{5.45}$$

The above agrees with the result in 4.4.4.

5.5.5 Global attraction

Combination of the above control to an invariant manifold and termination control realizes a positioning the second joint by periodic actuation of the first joint. However, a pair of different invariant manifolds divided by the axis $\theta_2 = 0$ have a same value of energy of Eq.(5.23) etc. as seen in Fig. 5.2. Then, a destination in, for instance, $\theta_2 > 0$ can be positioned only from an initial point in the same half of the phase plane with the combined control. Namely, the control is still insufficient to position it from any initial point to any destination. In this subsection, global attraction for any destination to be positioned is enabled.

The following is an algorithm for global attraction by the control methods to a manifold (5.29) or (5.35). The case with the destination in $\theta_2 > 0$ is considered in the algorithm and the other case with that in $\theta_2 < 0$ is represented in parentheses.

(i) If the state resides in the half $\theta_2 > 0$ ($\theta_2 < 0$), an invariant manifold passing through the destination is adopted as a destination to be stabilized.

(ii) If the state resides in the second quadrant $\theta_2 < 0$ and $\dot{\theta}_2 > 0$ (the fourth quadrant $\theta_2 > 0$ and $\dot{\theta}_2 < 0$), a manifold passing through $(\theta_2, \dot{\theta}_2) = (0, \pm v_{ex})$ is adopted as a destination to be stabilized.

(iii) If the state resides in the third quadrant $\theta_2 < 0$ and $\dot{\theta}_2 < 0$ (the first quadrant $\theta_2 > 0$ and $\dot{\theta}_2 > 0$), a manifold passing through $(\theta_2, \dot{\theta}_2) = (\pm q_{ex}, 0)$ is adopted as a destination to be stabilized.

The algorithm produces a flow: the third quadrant $\rightarrow (\pm q_{ex}, 0) \rightarrow$ the second quadrant $\rightarrow (0, \pm v_{ex}) \rightarrow$ the half $\theta_2 > 0 \rightarrow$ the destination, from the property that the manifold circulates around $\theta_2 = \pm\pi$. It enables to control to any destination from any initial point on the phase plane except for a few cases. All the points on the axis $\dot{\theta}_2 = 0$ except for the singular points $\theta_2 = 0, \pm\pi$ and $\theta_2 = \pm\dfrac{\pi}{2}$ are vibrated with a periodic perturbation and moved to another point with a certain

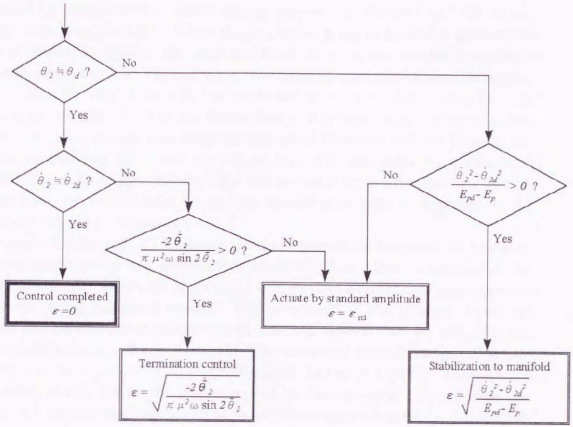

Figure 5.3: Flowchart of control by amplitude-normalized energy

velocity $|\dot{\theta}_2| > 0$. Furthermore from the second-order averaging analysis, since $\theta_2 = \bar{\theta}_2 + \varepsilon(1+\mu\cos\bar{\theta}_2)$ from Eq.(5.44), the singular points in the averaged dynamics $\theta_2 = 0, \pm\pi, \pm\frac{\pi}{2}$ shifts in the original dynamics by variation of ε. However, the fact that the stable point $\theta_2 = 0$ shifts simultaneously implies that the borders of the halves alters and the destination quite near to $\theta_2 = 0$ might be difficult to control since the half to which it belongs varies with ε.

5.6 Simulations

5.6.1 Control by amplitude-normalized energy

Figure 5.3 illustrates the flowchart of composition of the control to a desired manifold by amplitude-normalized energy proposed in Sec.5.5.1 and the termination control in Sec.5.5.4. When the control to a manifold or the termination control cannot be applied, the input-amplitude is set at the standard amplitude ϵ_{std} as shown in Fig. 5.3. The case when the control to a manifold cannot be applied denotes that $|\dot{\theta}_2 - \theta_{2c}| > |\dot{\theta}_{2d} - \theta_{2c}|$ as mentioned above in Sec.5.5.1. Therefore, the control will be difficult when the destination is very near to the center as shown below since the Poincaré map steps its footprints discretely and, accordingly, the chance to modulate the amplitude will be few. The case when the termination control cannot be applied denotes that the second joint overran the axis $\dot{\theta}_2 = 0$. In this case, the second joint has to turn around once again to approach to the neighborhood of the destination.

Figures 5.4 through 5.7 illustrate the trajectory of the averaged 2R free-joint manipulator, that on the amplitude-normalized phase plane, transition of the amplitude-normalized energy of the trajectory, and transition of the input-amplitude under the above composed control. The parameters of the periodic inputs are $\omega = 4\pi$ and the maximum, minimum and standard value of ε are set as $\varepsilon_{max} = 0.2$, $\varepsilon_{min} = 0.05$ and $\varepsilon_{std} = 0.1$, respectively. The initial and desired configurations are $(\theta_2, \dot{\theta}_2) = (0, 0) \mapsto (-130°, 0) = (-2.269[\text{rad}], 0)$. In Figs. 5.4 and 5.5, the solid line and empty circles denote the trajectory and its Poincaré map. The chained line in Fig. 5.5 denotes the desired elliptic manifold corresponding to the destination. Since the normalized energy is defined on the amplitude-normalized phase plane, the elliptic manifold is conserved only on the plane. In Fig. 5.6, the solid line denotes the energy transition and the dotted line denotes transition of the desired elliptic manifold corresponding to the destination. The energy was once stabilized to the desired value and it finally made slight difference by the termination control. In Fig. 5.7, the solid line denotes the transition of the input-amplitude. It is seen from the figure that the input-amplitude was modulated four times, $t = 5.5, 7, 7.5$ and 12.5[sec]. The first and third modulations of the input-amplitude correspond to the control to a desired manifold and the final modulation corresponds the termination control. The second modulation at $t = 7$[sec] implies that the input-amplitude was set at ε_{std} since θ_2 was very close to θ_{2d} and the termination control cannot be applied.

Since the averaged dynamics completely follows an invariant manifold for a constant input-amplitude, the modulation of Eq.(5.29) is carried out just a few times as shown in Fig. 5.7. The non-averaged original dynamics diverges from the invariant manifold after a period with an error order of ε^2 unless ε is sufficiently small. Therefore, the control method tends to stabilize the system where the velocity error is sufficiently small, since ε is figured out as a small value from

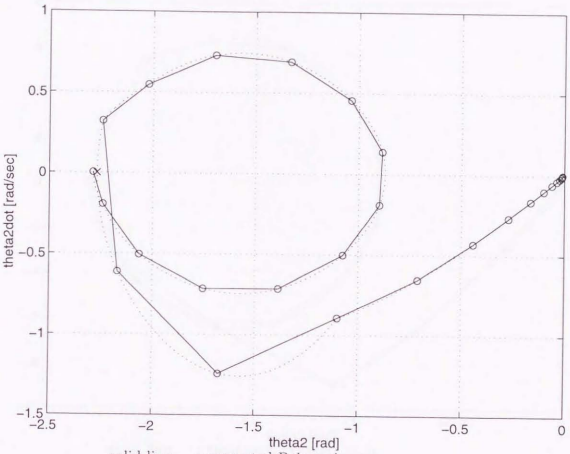

solid line : connected Poincaré map
dotted line : whole trajectory of averaged system
○ : Poincaré map
× : desired point

Figure 5.4: Trajectory of averaged 2R-FJM on 2nd joint's phase plane
Control by amp-normalized energy: $\theta_2 = 0° \mapsto -130°$

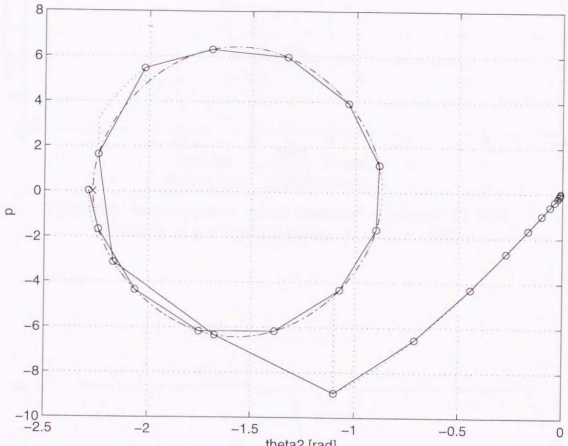

solid line	: connected Poincaré map
dotted line	: whole trajectory of averaged system
chained line	: desired elliptic manifold
∘	: Poincaré map
×	: desired point

Figure 5.5: Trajectory of averaged 2R-FJM on amp-normalized phase plane
Control by amp-normalized energy: $\theta_2 = 0° \mapsto -130°$

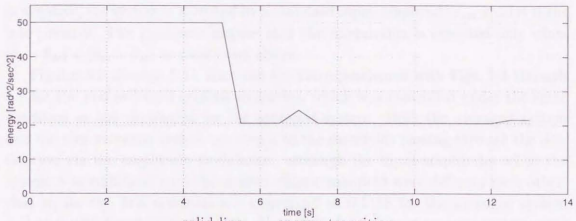

solid line : energy transition
dotted line : desired energy

Figure 5.6: Amp-normalized energy transition of averaged 2R-FJM
Control by amp-normalized energy: $\theta_2 = 0° \mapsto -130°$

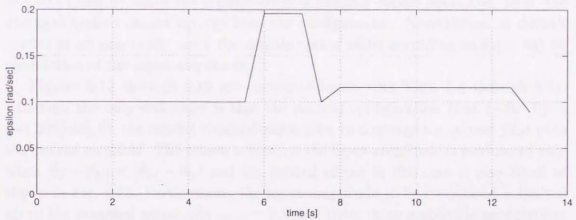

Figure 5.7: Input-amplitude transition for the averaged 2R-FJM
Control by amp-normalized energy: $\theta_2 = 0° \mapsto -130°$

Eq.(5.29). Practically, it is necessary to set an upper limit for the input-amplitude in order to maintain the approximation well and to set a lower limit so as not to almost stop the motion. In the case that the value in the square root of Eq.(5.29) is negative, the system is actuated by a standard input-amplitude ε_{std} until it turns into positive. The treatment implies that the modulation is executed only when $|\bar{\theta}_2 - \theta_{2c}| < |\bar{\theta}_{2d} - \theta_{2c}|$ as mentioned above.

Figures 5.8 through 5.11 illustrate the correspondences with Figs. 5.4 through 5.7 for the non-averaged original dynamics, which was controlled under the same condition as the simulation for the averaged system. Both the averaged system and the non-averaged system converged to the manifolds passing through the destination via the amplitude modulation, although the input-amplitudes when the system was stabilized onto the desired elliptic manifold were different each other, that is, for the first destination ε converged to 0.1158 for the averaged system and to 0.1018 for the non-averaged. Note that the values of energy are computed from phase values for the second-order averaged system by the following equations obtained from Eq.(5.44):

$$\begin{aligned} \bar{\theta}_2 &= \left\{ \bar{\theta}_2 \mid \theta_2 = \bar{\theta}_2 + \varepsilon(1 + \mu \cos \bar{\theta}_2) \right\} \\ \dot{\bar{\theta}}_2 &= \frac{\dot{\theta}_2}{1 + \varepsilon \sin \bar{\theta}_2} \end{aligned} \tag{5.46}$$

where the upper equation is solved numerically and, therefore, the value of desired energy varies a little depending on modulation of the input-amplitude. In addition, the initial configuration for the averaged system was not exactly at $(0, 0)$ but at $(-0.01[\text{rad}], 0)$, since the configuration is singular saddle point and, then, the averaged system cannot diverge from the configuration. Nevertheless, it doesn't matter at all practically since the singular point shifts according to Eq.(5.46) by modulation of the input-amplitude.

Figures 5.12 through 5.19 are correspondences with Figs. 5.4 through 5.11. Although the only difference is that the desired configuration is at $(-80°, 0) = (-1.396[\text{rad}], 0)$, the control required much time to converge the second joint onto the desired manifold. The reason is because the input-amplitude is modulated only when $|\bar{\theta}_2 - \theta_{2c}| < |\bar{\theta}_{2d} - \theta_{2c}|$ and the desired ellipse in this case is very small as shown in Fig. 5.13. Furthermore, the input-amplitude to be modulated is limited up to the maximal amplitude $\varepsilon_{max} = 0.2$ and then, more amplitude modulations are required to attain the desired ellipse.

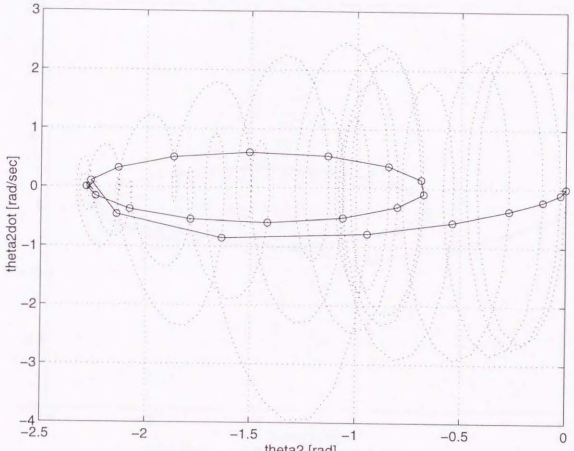

solid line : connected Poincaré map
dotted line : whole simulated trajectory
$\circ$: Poincaré map
$\times$: desired point

Figure 5.8: Trajectory of simulated 2R-FJM on 2nd joint's phase plane
Control by amp-normalized energy: $\theta_2 = 0° \mapsto -130°$

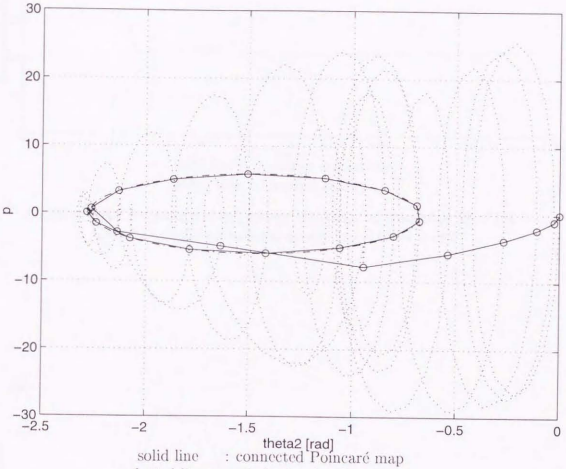

solid line	: connected Poincaré map
dotted line	: whole simulated trajectory
chained line	: desired elliptic manifold
∘	: Poincaré map
×	: desired point

Figure 5.9: Trajectory of simulated 2R-FJM on amp-normalized phase plane
Control by amp-normalized energy: $\theta_2 = 0° \mapsto -130°$

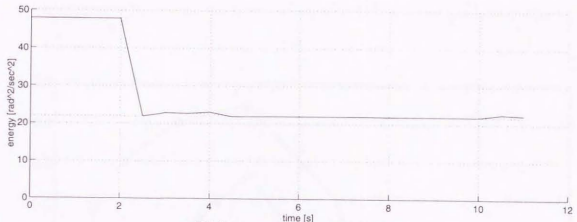

solid line : energy transition
dotted line : desired energy

Figure 5.10: Amp-normalized energy transition of simulated 2R-FJM
Control by amp-normalized energy: $\theta_2 = 0° \mapsto -130°$

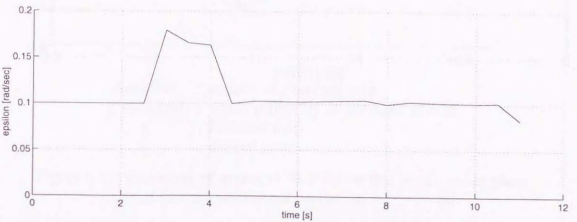

Figure 5.11: Input-amplitude transition for the simulated 2R-FJM
Control by amp-normalized energy: $\theta_2 = 0° \mapsto -130°$

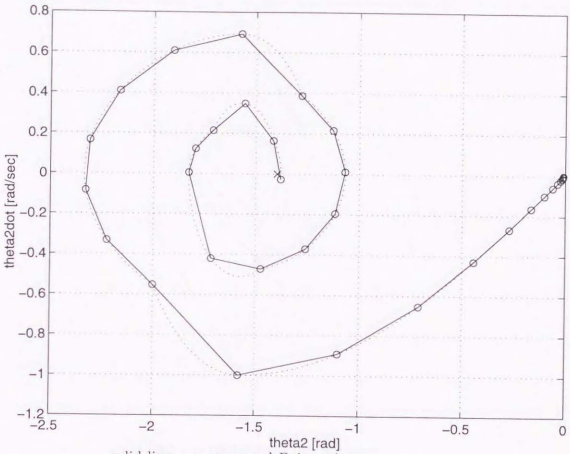

solid line : connected Poincaré map
dotted line : whole trajectory of averaged system
○ : Poincaré map
× : desired point

Figure 5.12: Trajectory of averaged 2R-FJM on 2nd joint's phase plane
Control by amp-normalized energy: $\theta_2 = 0° \mapsto -80°$

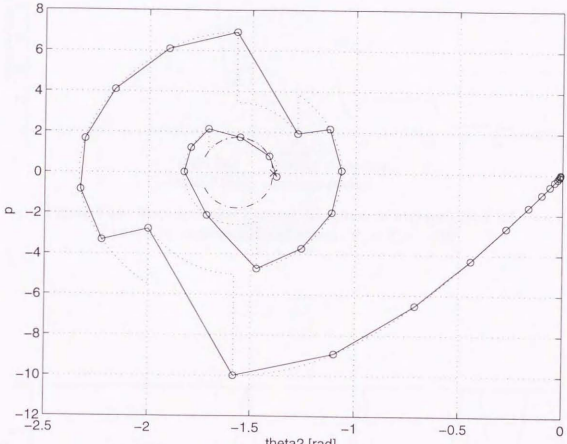

solid line	: connected Poincaré map
dotted line	: whole trajectory of averaged system
chained line	: desired elliptic manifold
∘	: Poincaré map
×	: desired point

Figure 5.13: Trajectory of averaged 2R-FJM on amp-normalized phase plane
Control by amp-normalized energy: $\theta_2 = 0° \mapsto -80°$

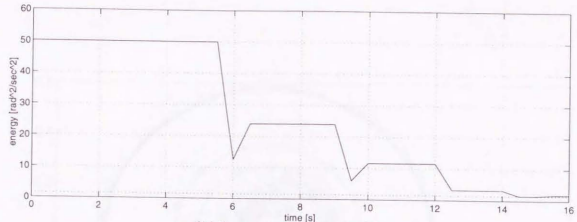

solid line : energy transition
dotted line : desired energy

Figure 5.14: Amp-normalized energy transition of averaged 2R-FJM
Control by amp-normalized energy: $\theta_2 = 0° \mapsto -80°$

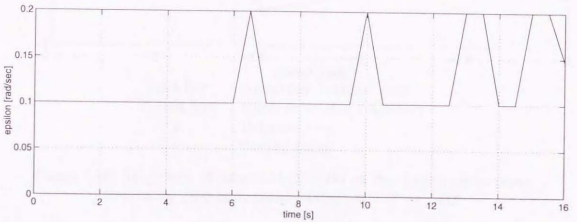

Figure 5.15: Input-amplitude transition for the averaged 2R-FJM
Control by amp-normalized energy: $\theta_2 = 0° \mapsto -80°$

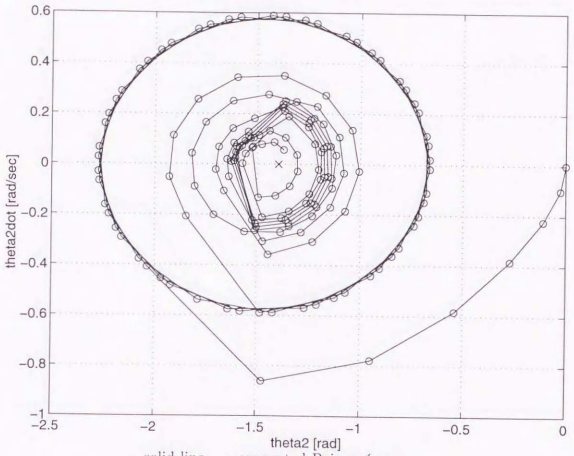

solid line	: connected Poincaré map
dotted line	: whole simulated trajectory
○	: Poincaré map
×	: desired point

Figure 5.16: Trajectory of simulated 2R-FJM on 2nd joint's phase plane
Control by amp-normalized energy: $\theta_2 = 0° \mapsto -80°$

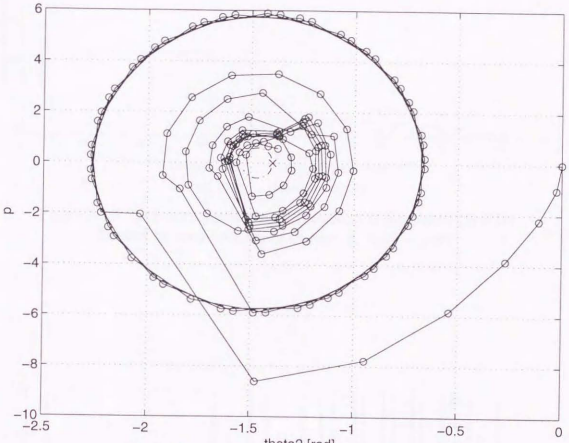

solid line	: connected Poincaré map
dotted line	: whole simulated trajectory
chained line	: desired elliptic manifold
○	: Poincaré map
×	: desired point

Figure 5.17: Trajectory of simulated 2R-FJM on amp-normalized phase plane
Control by amp-normalized energy: $\theta_2 = 0° \mapsto -80°$

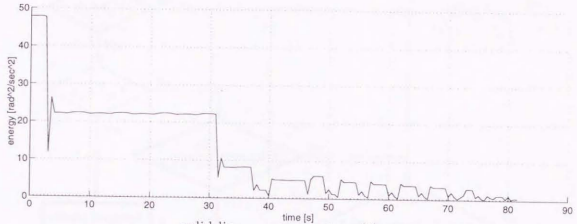

solid line : energy transition
dotted line : desired energy

Figure 5.18: Amp-normalized energy transition of simulated 2R-FJM
Control by amp-normalized energy: $\theta_2 = 0° \mapsto -80°$

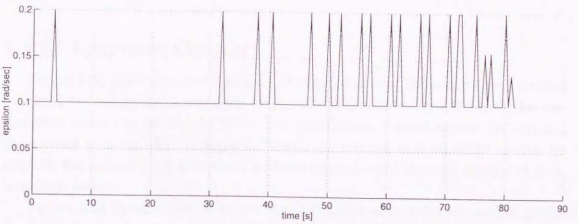

Figure 5.19: Input-amplitude transition for the simulated 2R-FJM
Control by amp-normalized energy: $\theta_2 = 0° \mapsto -80°$

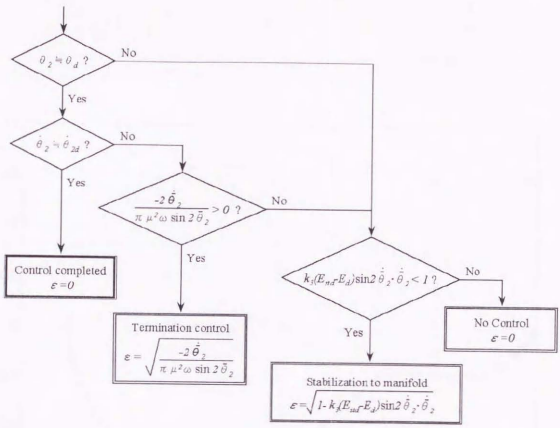

Figure 5.20: Flowchart of Lyapunov control

5.6.2 Lyapunov Control

Figure 5.20 illustrates the flowchart of composition of the control to a desired manifold by energy for a standard amplitude proposed in Sec.5.5.2 and the termination control in Sec.5.5.4. When the termination control cannot be applied, the control to a manifold is applied. When the control to a manifold cannot be applied, the second joint is released without control since the case implies that $\dot{\theta}_2$ is enough large.

Figures 5.21 through 5.26 illustrate the correspondences under the second amplitude-modulation control proposed in Sec.5.5.2 with Figs. 5.4 through 5.11 except Figs. 5.5 and 5.9 plotted on the amplitude-normalized phase plane. The conditions for simulations are same as in the above simulations for the control by amplitude-normalized energy. The gain for the amplitude modulation in Eq.(5.35) is set at $k_3 = 50.0$. The second method is a little more efficient than the first method

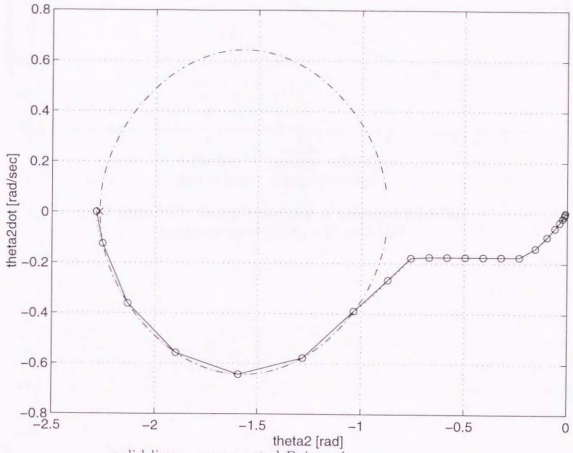

solid line	: connected Poincaré map
dotted line	: whole trajectory of averaged system
chained line	: desired elliptic manifold
∘	: Poincaré map
×	: desired point

Figure 5.21: Trajectory of averaged 2R-FJM on 2nd joint's phase plane
Lyapunov control: $\theta_2 = 0° \mapsto -130°$

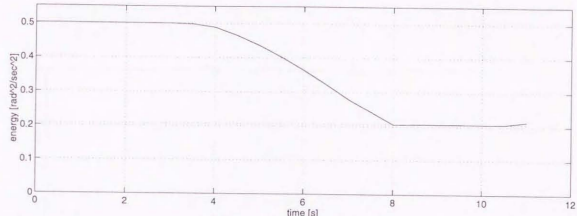

solid line : energy transition
dotted line : desired energy

Figure 5.22: Energy transition of averaged 2R-FJM
Lyapunov control: $\theta_2 = 0° \mapsto -130°$

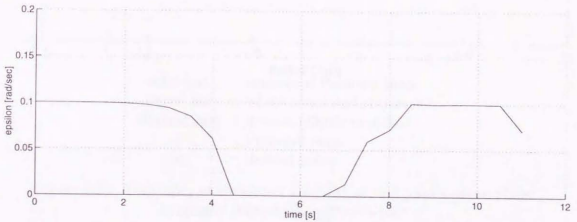

Figure 5.23: Input-amplitude transition for the averaged 2R-FJM
Lyapunov control: $\theta_2 = 0° \mapsto -130°$

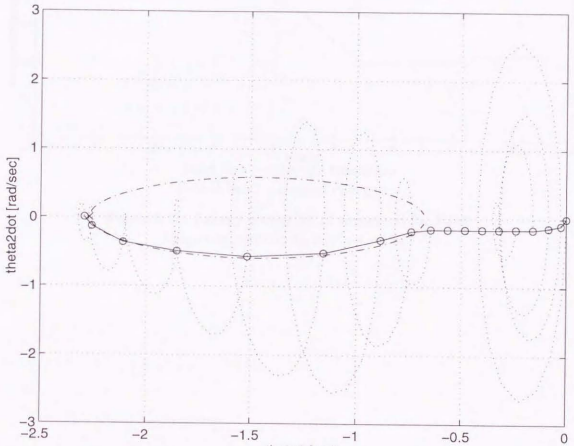

solid line	: connected Poincaré map
dotted line	: whole simulated trajectory
chained line	: desired elliptic manifold
○	: Poincaré map
×	: desired point

Figure 5.24: Trajectory of simulated 2R-FJM on 2nd joint's phase plane
Lyapunov control: $\theta_2 = 0° \mapsto -130°$

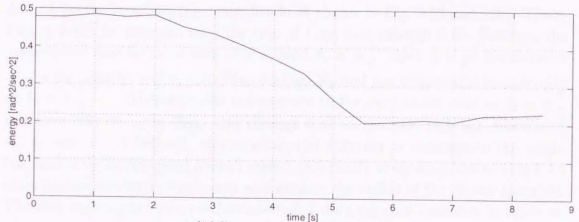

solid line : energy transition
dotted line : desired energy

Figure 5.25: Energy transition of simulated 2R-FJM
Lyapunov control: $\theta_2 = 0° \mapsto -130°$

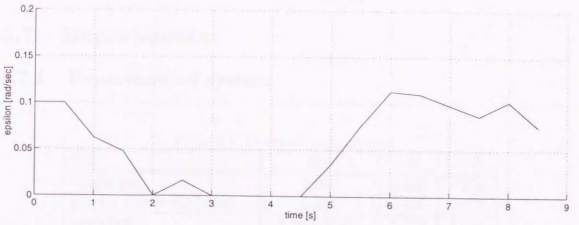

Figure 5.26: Input-amplitude transition for the simulated 2R-FJM
Lyapunov control: $\theta_2 = 0° \mapsto -130°$

since it uses "no control" phase when the second joint has enough momentum to drift toward the desired ellipse. A greater advantage of the method is that the amplitude is modulated to stabilize the energy to a constant desired value defined for the standard input-amplitude as shown in Fig. 5.22 and 5.25. Therefore, it won't be stagnant as in the case of Figs. 5.12 through 5.15. However, the convergence rate becomes very slow around $\theta_2 = \pm\frac{\pi}{2}$, since $\dot{L}$ is proportional to $E_{std} - E_d$, namely, $\cos^2\theta_2 - \cos^2\theta_{2d}$, and $\sin 2\theta_2$ and the magnitudes become zero at $\theta_2 = \pm\frac{\pi}{2}$. Therefore, the convergence to the destination near to $\theta_2 = \pm\frac{\pi}{2}$ was very difficult as in Figs. 5.30 through 5.32 in the case with the destination $\theta_{2d} = -80° = -1.396$[rad]. Nevertheless, the difficulty to converge to the neighborhood of the center point doesn't matter practically as shown in the section 5.7.3 since friction dissipates the energy and reduces the radius of the elliptic manifold. The slow convergence rate will be dissolved if the Lyapunov candidate is taken as:

$$L' = \frac{1}{2}\left(\frac{E_{std}}{E_d} - 1\right)^2 \tag{5.47}$$

The derivative of L' yields

$$\dot{L}' = \left(\left(\frac{\bar{\varepsilon}}{\bar{\varepsilon}_{std}}\right)^2 - 1\right)\left(\frac{E_{std}}{E_d} - 1\right)\frac{\sin 2\theta_2}{\cos^2\theta_{2d}}\dot{\theta}_2$$

Though, there will occur a larger problem in the case for $\theta_{2d} = \pm\frac{\pi}{2}$. As θ_2 gets closer to θ_{2d}, $\dot{L}'$ becomes almost infinity since $\dfrac{\sin 2\theta_2}{\cos^2\theta_d}$ gets close to $2\tan\theta_{2d}$.

5.7 Experiments

5.7.1 Experimental system

Table 5.1: Dynamic parameters

link	first	mid	end
length [m]	0.200	0.200	0.200
gravity center (GC) [m]	0.016	0.100	0.100
mass [kg]	2.500(3.345)	2.310	1.700
inertia about GC [kg·m^2]	0.0243	0.0230	0.0132
inertia about joint [kg·m^2]	0.0309(0.0312)	0.0461	0.0302

An experimental free-joint manipulator system was newly developed to verify the validity of the proposed methods. Figures 5.33 and 5.34 are the plan and

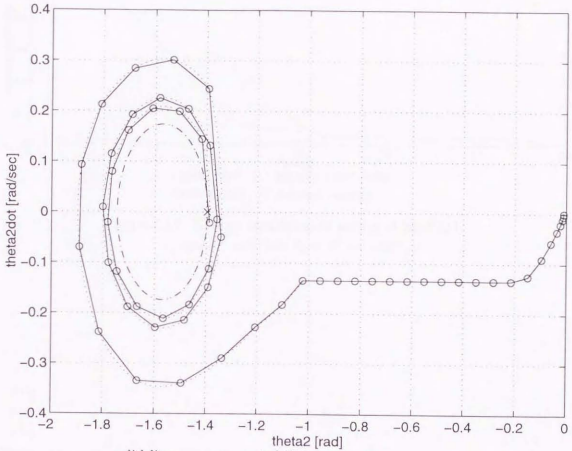

solid line	: connected Poincaré map
dotted line	: whole trajectory of averaged system
chained line	: desired elliptic manifold
○	: Poincaré map
×	: desired point

Figure 5.27: Trajectory of averaged 2R-FJM on 2nd joint's phase plane
Lyapunov control: $\theta_2 = 0° \mapsto -80°$

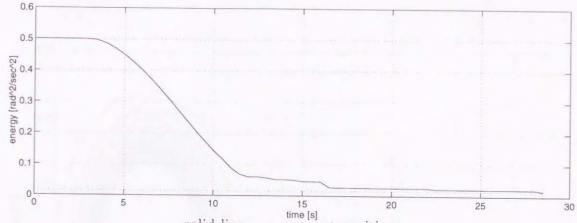

solid line : energy transition
dotted line : desired energy

Figure 5.28: Energy transition of averaged 2R-FJM
Lyapunov control: $\theta_2 = 0° \mapsto -80°$

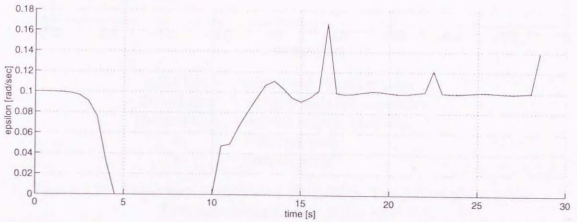

Figure 5.29: Input-amplitude transition for the averaged 2R-FJM
Lyapunov control: $\theta_2 = 0° \mapsto -80°$

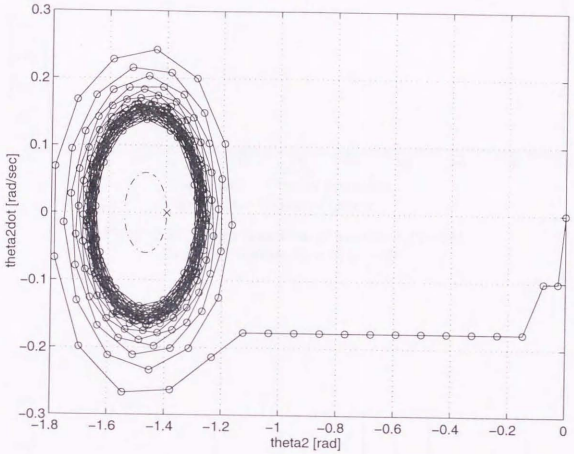

solid line	: connected Poincaré map
dotted line	: whole simulated trajectory
chained line	: desired elliptic manifold
○	: Poincaré map
×	: desired point

Figure 5.30: Trajectory of simulated 2R-FJM on 2nd joint's phase plane
Lyapunov control: $\theta_2 = 0° \mapsto -80°$

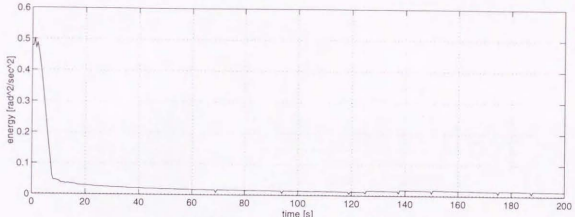

solid line : energy transition
dotted line : desired energy

Figure 5.31: Energy transition of simulated 2R-FJM
Lyapunov control: $\theta_2 = 0° \mapsto -80°$

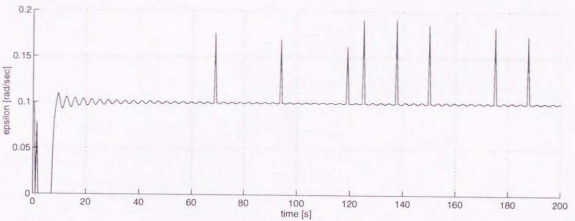

Figure 5.32: Input-amplitude transition for the simulated 2R-FJM
Lyapunov control: $\theta_2 = 0° \mapsto -80°$

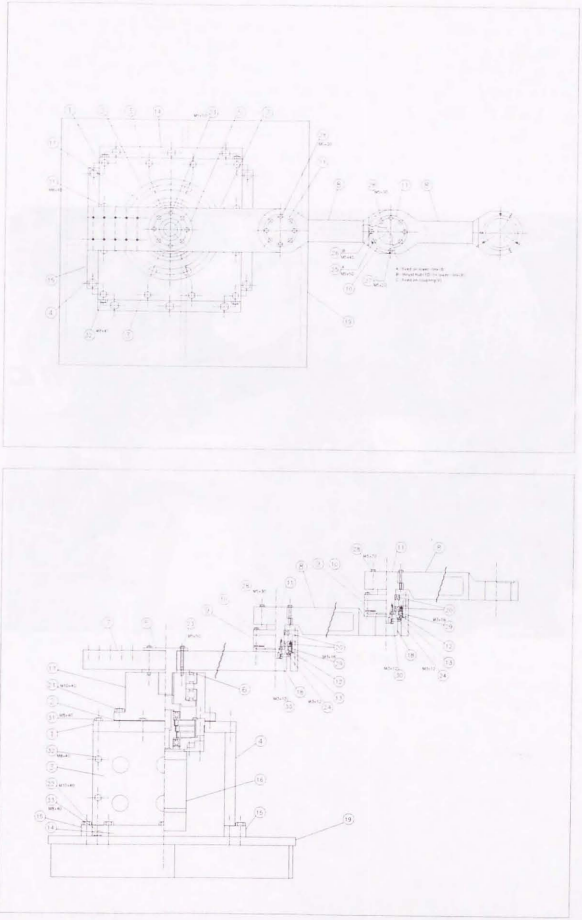

Figure 5.33: Plan of the free-joint manipulator

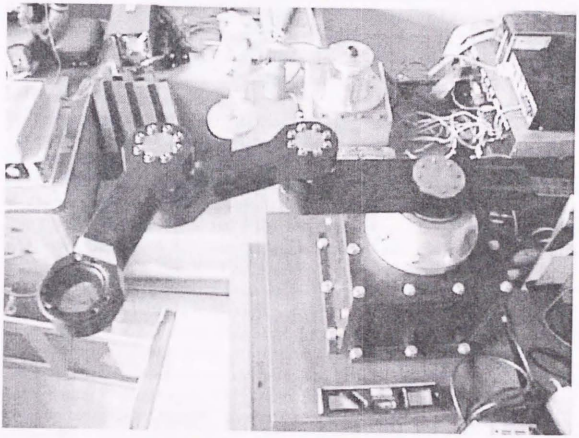

Figure 5.34: Photo of the free-joint manipulator

photograph of the manipulator established as a 3R free-joint manipulator, respectively. All the joints of the manipulator are planar and revolute. The first joint is only actuated and the other joints are free to move. The actuator is composed of a YASKAWA AC servo motor SGM-08A314 and a SUMITOMO transmission FA25 with the gear ratio 1:59. Pictures of the actuator component are shown in Fig. 5.35.

The links are made of aluminum with black coating and the axes are made of stainless. The size of the manipulator is approximately 85 cm long × 45 cm wide × 57 cm tall including a cast iron platform. The first link is approximately 39.0 cm long × 8.0 cm wide × 3.5 cm thick, and the middle and end links are 28.0 cm long × 8.0 cm wide × 5.0 cm thick. The other important dynamic parameters of the manipulator are shown in Table 5.1. In the table, the parameters of the first link are those only of the link itself. The parameters in parentheses for the mass and inertia about joint denote the values when those of the first axis are included. Each of the free joints other than the first joint is equipped with a special coupling part with four cuts on the side from every direction at right angles each other as shown in Fig. 5.36. Tightening or loosening three in six bolts in the picture bends the cuts a little and can precisely adjust the perpendicular of the axes.

The manipulator is controlled by an IBM-PC/AT compatible PC, GATEWAY 2000 P5-166 with a Pentium 166 MHz chip. The motor has its own servopack, YASKAWA SGD-08AS. Its power supply is AC200V and has a rated power of 750W, a maximum torque of 7.1[N·m], and a maximum speed of 4500 rpm. The motor is controlled by velocity feedback and the velocity is specified by analog voltage commands in the ±10 V range, sent from a D/A board, CONTEC DA12-8L in the PC. An incremental encoder with 2048 P/R is equipped to the motor and it feeds back 120832 pulses per a revolution of the first joint. Each of the free joints has an incremental encoder with 3600 P/R, OMRON E6h-CWZ3E. The sensor data is obtained to the PC by a counter board, CONTEC CNT24-4(PC), with four channels for encoders. Electrical setup for control of the motor is shown in Fig.5.37.

This experimental manipulator has a very simple mechanism. Although the free-joint parts are a little complex and heavy, it will be simpler and lighter in the case without gravity, e.g. space manipulators.

5.7.2 Preliminary experiments

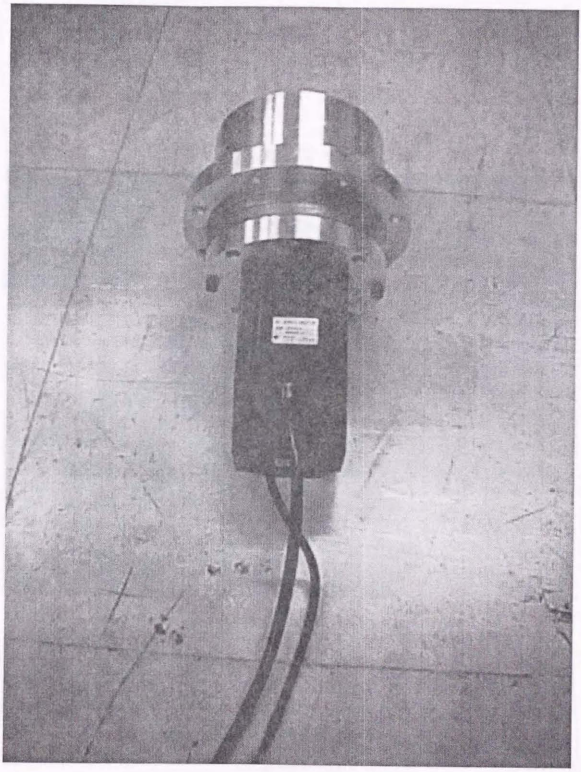

Figure 5.35: Picture of actuator component

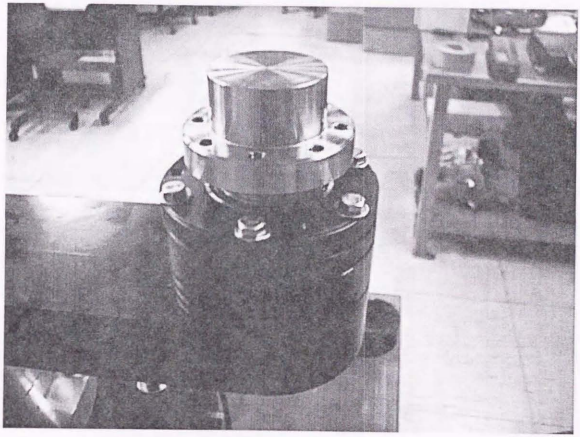

Figure 5.36: Picture of free-joint part

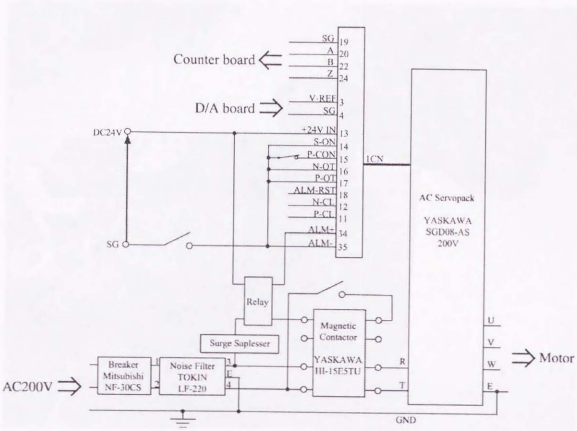

Figure 5.37: Electrical setup for motor

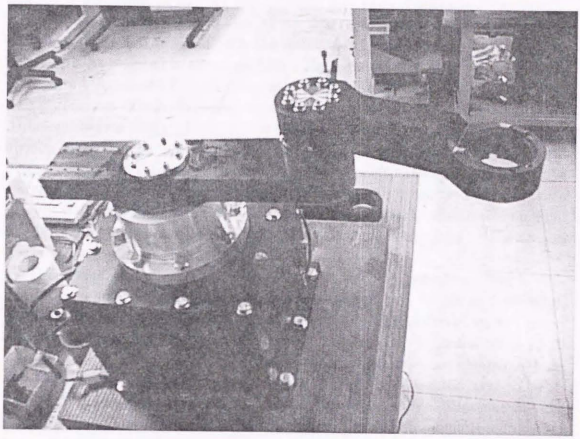

Figure 5.38: Experimental 2R free-joint manipulator

The experimental manipulator system was set up in experiments for 2R free-joint manipulators as shown in Fig. 5.38. The dynamical constants in the case are:

$$A_1 = m_1 {s_1}^2 + m_2 {l_1}^2 + I_1 = 3.36 \times 10^{-2}[\mathrm{kg{\cdot}m^2}]$$
$$A_2 = m_2 {s_2}^2 + I_2 = m_2 {s_2}^2 + I_2 = 3.02 \times 10^{-2}[\mathrm{kg{\cdot}m^2}]$$
$$B = m_2 l_1 s_2 = 3.40 \times 10^{-2}[\mathrm{kg{\cdot}m^2}]$$

and, then, $\mu = \dfrac{B}{A_2} = 1.1258$. Note that mass and inertia constants of the second link agree with those of the end link in Table 5.1. First, behaviors of the manipulator under a sinusoidal actuation of the first joint with a constant amplitude were investigated. The result with the initial setting is shown in Fig. 5.39. The behavior is represented in the second joint phase plane. The solid line in Fig.5.39 represents a connected Poincaré map of the whole trajectory of the second joint. The parameters of the sinusoidal input are: $\omega = 4\pi$[rad/sec] and $\varepsilon = 0.1$[rad]. Although friction exists and dissipates the momentum of the second joint, the influence of the friction is enough small and the phase trajectory doesn't stop and follows a swirl-like trajectory. However they were constructed upon a conservative system without dissipation, the proposed control methods can be applied to such systems with small enough friction and can stabilize them to an elliptic manifold. In addition, appropriate values of input parameters are determined as $\omega = 4\pi$ and $\varepsilon = 0.1$ from preliminary experiments.

There were several other problems precedent to the experiments. One is difficulty to take finer Poincaré map from discrete data of joint angles and velocities. Although the sampling time to measure the counts of encoders was set at 1[msec] by timer interruption, the sampling time of program loop is estimated at 12 to 17[msec] chiefly to write data to a file. Since the velocities are computed from differences of the counts of encoders, the errors in the velocities too large to be ignored and those for the Poincaré sections become further large. Consequently, the computed energy of the elliptic manifold oscillates extremely which is represented by a solid line in Fig. 5.40. Another reason can be considered that the velocity $\dot{\theta}_2$ is dissipated by friction when it is comparatively large to E_p. It explains periodical reduction of the energy in Fig. 5.40. However there is some oscillation, there can be seen the tendency of exponential-like convergence in the figure. Then, the energy was determined to compute as an average of the current value and the value in the previous period. The broken line denotes the transition of the averaged energy and is smoother variation of the energy.

5.7.3 Experiments of positioning the 2R-FJM

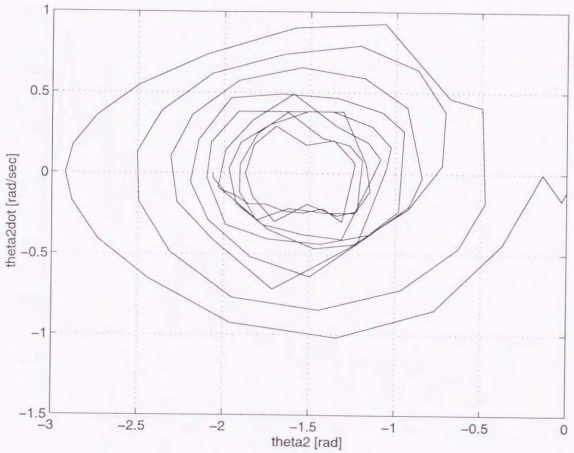

Figure 5.39: Poincaré map under constant input-amplitude

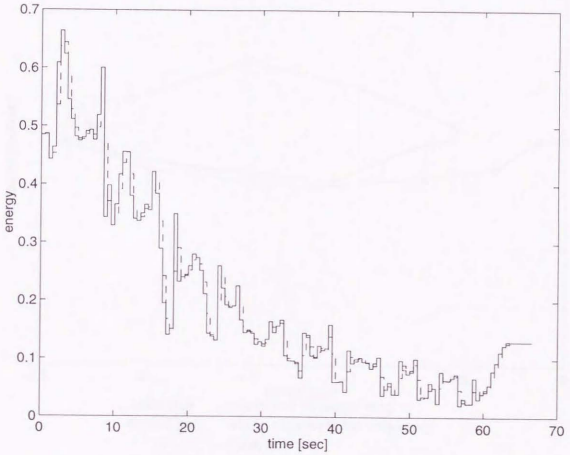

Figure 5.40: Standard energy under constant input-amplitude

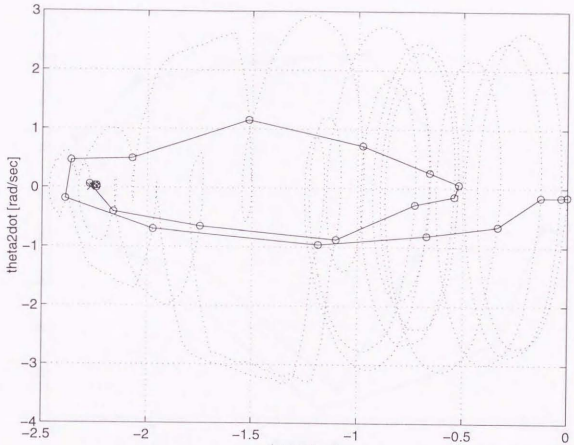

solid line	: connected Poincaré map
dotted line	: whole experimental trajectory
∘	: Poincaré map
×	: desired point

Figure 5.41: Experimental trajectory on 2nd-joint's phase plane
Control by amp-normalized energy: $\theta_2 = 0° \mapsto -130°$

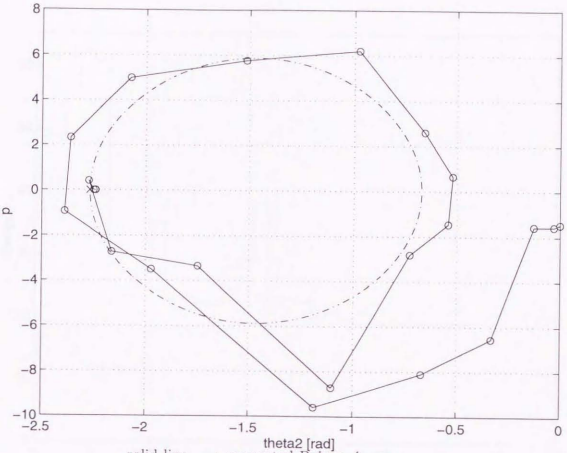

solid line	: connected Poincaré map
dotted line	: whole experimental trajectory
chained line	: desired elliptic manifold
o	: Poincaré map
×	: desired point

Figure 5.42: Experimental trajectory on amp-normalized phase plane
Control by amp-normalized energy: $\theta_2 = 0° \mapsto -130°$

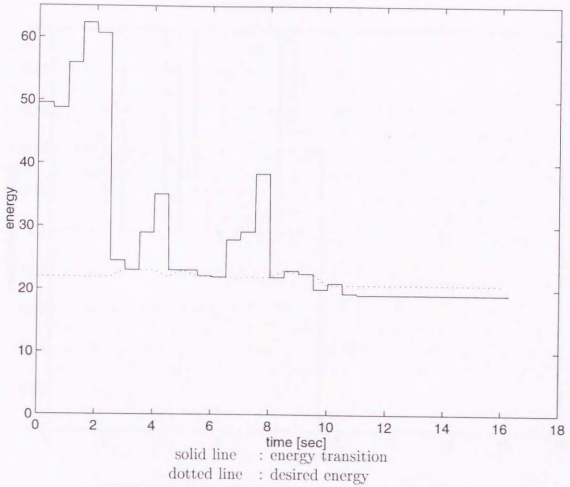

Figure 5.43: Experimental amp-normalized energy transition
Control by amp-normalized energy: $\theta_2 = 0° \mapsto -130°$

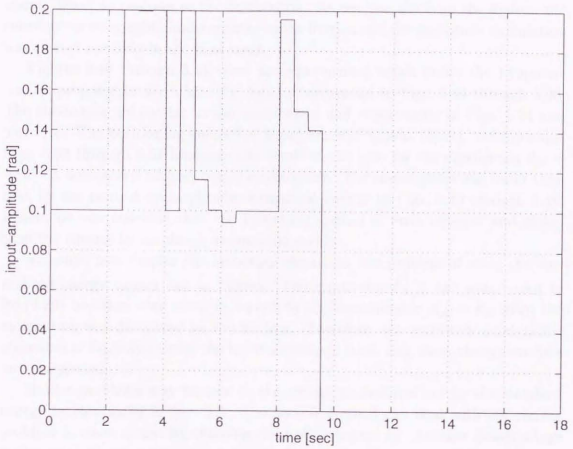

Figure 5.44: Experimental input-amplitude transition
Control by amp-normalized energy: $\theta_2 = 0° \mapsto -130°$

Figures 5.41 through 5.44 show an experimental result under the control by amplitude-normalized energy proposed in Sec.5.5.1. The figures correspond to Figs. 5.8 through 5.11. The initial configuration and destination are $(\theta_2, \dot{\theta}_2) = (0, 0)$ and $(-130[\text{deg}], 0) = (-2.2689[\text{rad}], 0)$. The accuracy of positioning is set at $|\theta_2 - \theta_{2d}| < 2.0[\text{deg}] = 0.0349[\text{rad}]$ and $|\dot{\theta}_2| < 4.0[\text{deg/sec}] = 0.0698[\text{rad/sec}]$. The positioning succeeded within 10[sec]. It is much better than those by the heuristic control method developed in Chap.4. Figures 5.45 through 5.48 are the experimental result for the destination $(-80[\text{deg}], 0) = (-1.396[\text{rad}]. 0)$. It took about 76[sec] to position to the destination. As one can see from the figures, the convergence was ought almost entirely to the friction and the amplitude modulation was carried out only in the final stage.

Figures 5.49 through 5.51 show an experimental result under the Lyapunov control proposed in Sec.5.5.2. The figures correspond to Figs. 5.24 through 5.26. The conditions are similar to the simulations and experiments of Figs. 5.24 and 5.41, etc. The positioning succeeded approximately within 16[sec]. Additionally, Figs. 5.52 through 5.54 illustrate the result in the case for the destination $\theta_{2d} = -80°$. It took about 51 [sec] before convergence. The convergence was faster than that by the control by amplitude-normalized energy in Figs. 5.45 through 5.48. Hence, we can conclude that the Lyapunov control is more efficient and global than the control by amplitude-normalized energy.

Although it is simpler and smoother algorithm, the problem of using the normalized energy turned out as follows: The numerator $\dot{\theta}_2^2$ in the square-root in Eq.(5.29) becomes very small in regard to the denominator $E_{pd} - E_p$ when the momentum was dissipated by the friction. Therefore, the amplitude modulation algorithm of Eq.(5.29) makes the input-amplitude small and, then, the system falls into stagnation.

Similar problems may happen to the second control method by the standard energy as mentioned in Sec. 5.6. The second method can deal with the similar problem to some extent by choosing the feedback gain k_3. Another disadvantage is that the algorithm with "no-control" phase makes the input efficient in energy but results in steep acceleration at when switching the control phase.

5.8 Conclusion

The results in this chapter are as follows:

1. First-order periodic averaging was applied to analyze the behaviors of manipulators with one actuator and several free joints in response to a periodic input. The averaged motion was determined independently of the input-amplitude.

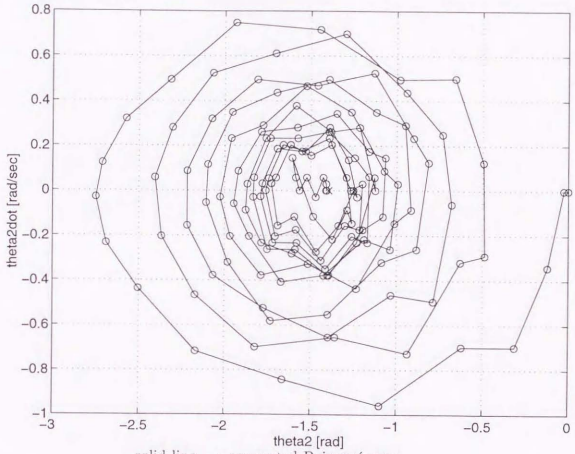

solid line : connected Poincaré map
dotted line : whole experimental trajectory
○ : Poincaré map
× : desired point

Figure 5.45: Experimental trajectory on 2nd-joint's phase plane
Control by amp-normalized energy: $\theta_2 = 0° \mapsto -80°$

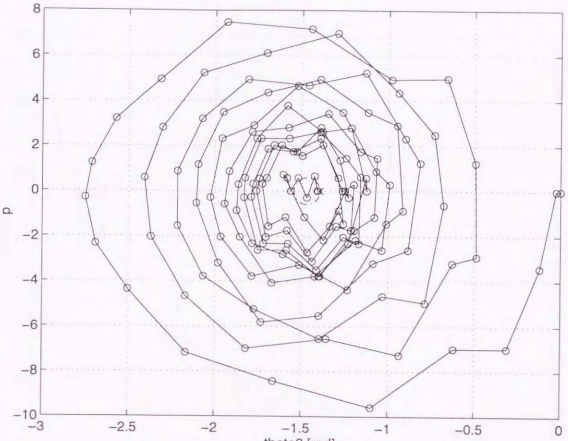

solid line	: connected Poincaré map
dotted line	: whole experimental trajectory
chained line	: desired elliptic manifold
∘	: Poincaré map
×	: desired point

Figure 5.46: Experimental trajectory on amp-normalized phase plane
Control by amp-normalized energy: $\theta_2 = 0° \mapsto -80°$

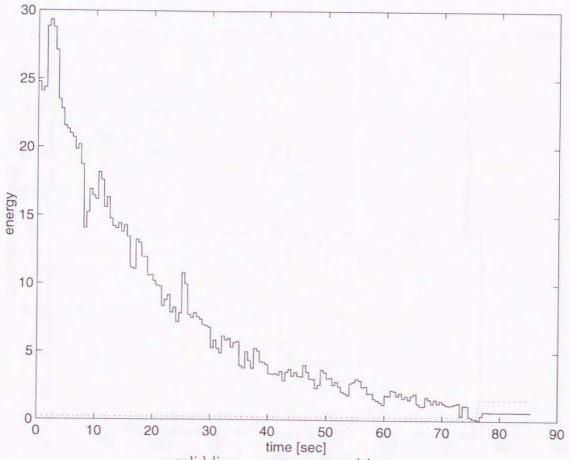

Figure 5.47: Experimental amp-normalized energy transition
Control by amp-normalized energy: $\theta_2 = 0° \mapsto -80°$

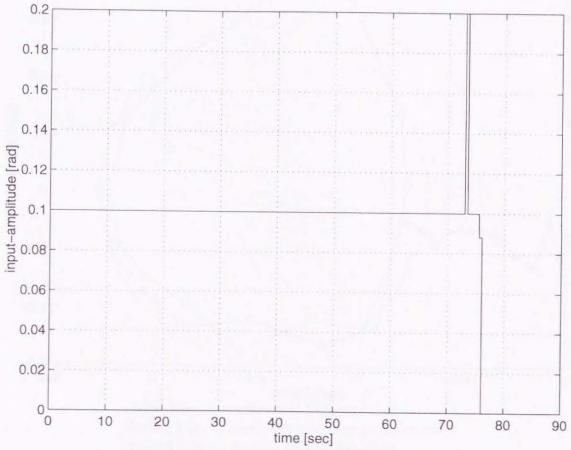

Figure 5.48: Experimental input-amplitude transition
Control by amp-normalized energy: $\theta_2 = 0° \mapsto -80°$

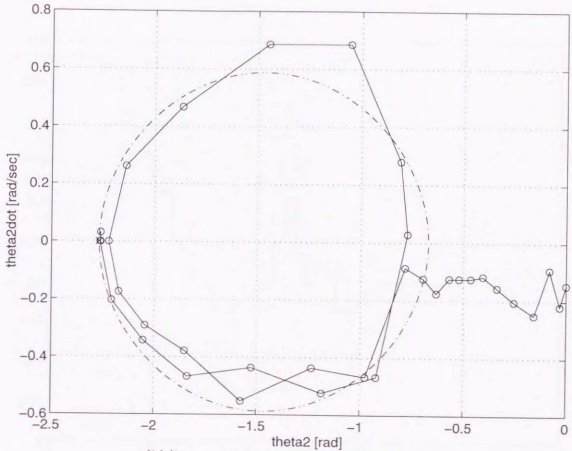

solid line	: connected Poincaré map
dotted line	: whole experimental trajectory
chained line	: desired elliptic manifold
∘	: Poincaré map
×	: desired point

Figure 5.49: Experimental trajectory on 2nd-joint's phase plane
Lyapunov control: $\theta_2 = 0° \mapsto -130°$

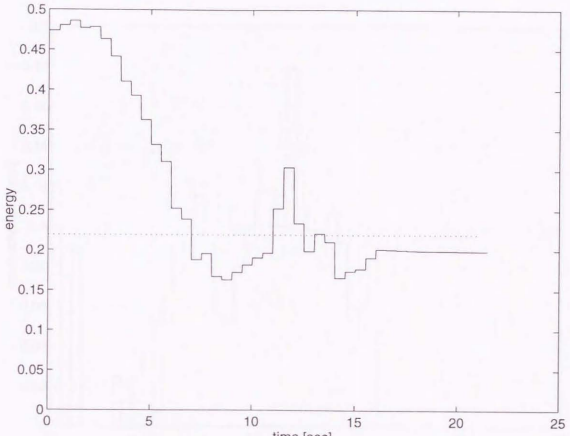

solid line : energy transition
dotted line : desired energy

Figure 5.50: Experimental energy transition
Lyapunov control: $\theta_2 = 0° \mapsto -130°$

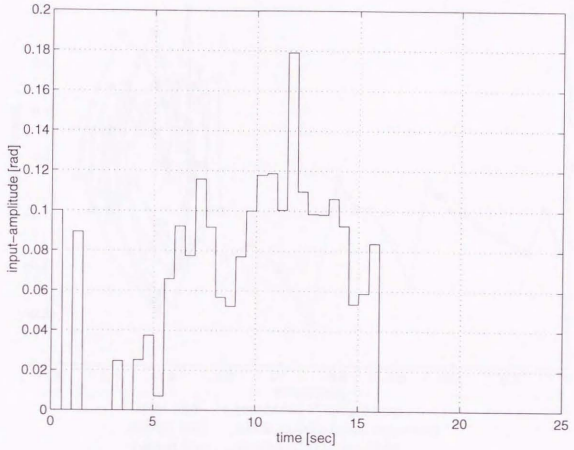

Figure 5.51: Experimental input-amplitude transition
Lyapunov control: $\theta_2 = 0° \mapsto -130°$

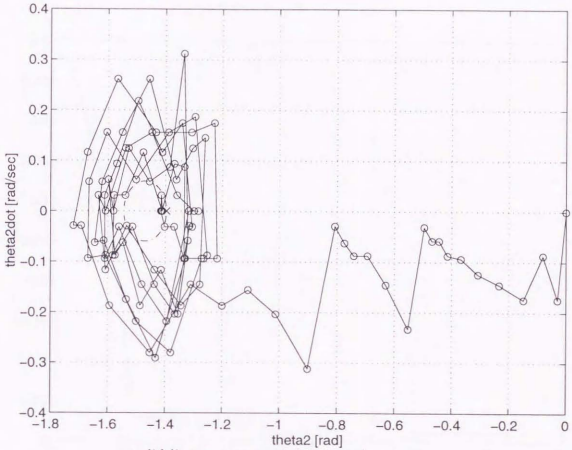

solid line	: connected Poincaré map
dotted line	: whole experimental trajectory
chained line	: desired elliptic manifold
○	: Poincaré map
×	: desired point

Figure 5.52: Experimental trajectory on 2nd-joint's phase plane
Lyapunov control: $\theta_2 = 0° \mapsto -80°$

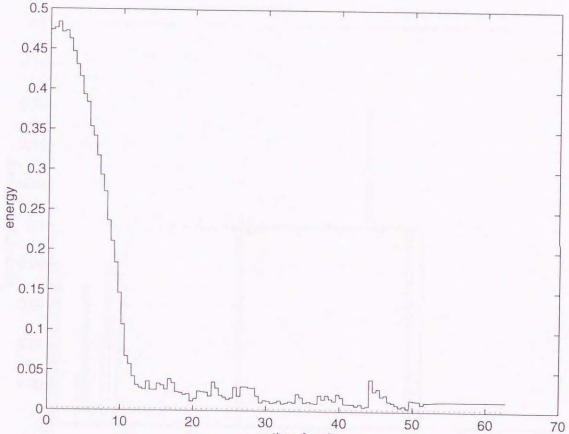

Figure 5.53: Experimental energy transition
Lyapunov control: $\theta_2 = 0° \mapsto -80°$

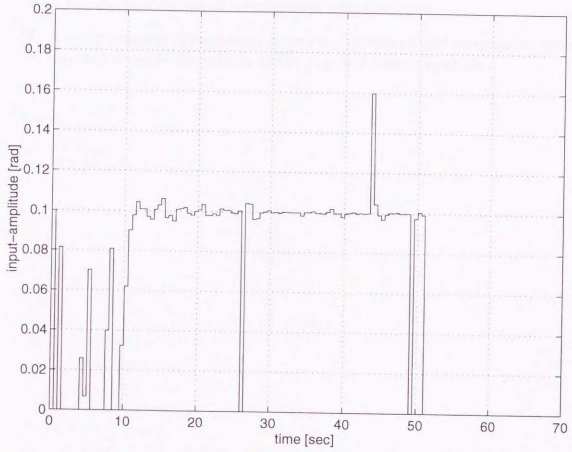

Figure 5.54: Experimental input-amplitude transition
Lyapunov control: $\theta_2 = 0° \mapsto -80°$

2. The invariant manifolds of 2R free-joint manipulators were shown and their conservation was formulated by use of a Hamiltonian.

3. Two control methods to an invariant manifold of the Hamiltonian were proposed via modulation of the input amplitude.

4. Second-order averaging analysis was developed to obtain a better approximation.

5. A method to terminate at a destination were developed.

6. A newly designed experimental system was developed and experiments were executed to verify the validity of the proposed control methods.

Chapter 6

Analysis and Control of 3R Free-Joint Manipulators with One Motor

6.1 Nomenclature

$A_1 \stackrel{\text{def}}{=} I_1 + m_1 {l_{c1}}^2 + m_2 {l_1}^2 + m_3 {l_1}^2$; dynamical coefficient
$A_2 \stackrel{\text{def}}{=} I_2 + m_2 {l_{c2}}^2 + m_3 {l_2}^2$; dynamical coefficient
$A_3 \stackrel{\text{def}}{=} I_3 + m_3 {l_{c3}}^2$; dynamical coefficient
$\bar{A}_2 \stackrel{\text{def}}{=} A_2 / B_{32}$; normalized dynamical coefficient
$\bar{A}_3 \stackrel{\text{def}}{=} A_3 / B_{32}$; normalized dynamialc coefficient
$B_{21} \stackrel{\text{def}}{=} m_3 l_1 l_2 + m_2 l_1 l_{c2}$; dynamical coefficient
$B_{31} \stackrel{\text{def}}{=} m_3 l_1 l_{c3}$; dynamical coefficient
$B_{32} \stackrel{\text{def}}{=} m_3 l_2 l_{c3}$; dynamical coefficient
$c_{ji} \stackrel{\text{def}}{=} \cos(\theta_j - \theta_i)$; abbreviation for cosine
$\tilde{c}_{ji} \stackrel{\text{def}}{=} B_{ji} c_{ji} / B_{32}$; normalized cosine
$s_{ji} \stackrel{\text{def}}{=} \sin(\theta_j - \theta_i)$; abbreviation for sine
$\tilde{s}_{ji} \stackrel{\text{def}}{=} B_{ji} s_{ji} / B_{32}$; normalized sine
$\Delta \stackrel{\text{def}}{=} \bar{A}_2 \bar{A}_3 - {c_{32}}^2$; determinant of reduced inertia matrix

Notations of the other variables and constants conform to those in Chaps. 4 and 5.

6.2 3R Free-Joint Manipulators with Only One Motor

6.2.1 Averaging the manipulator

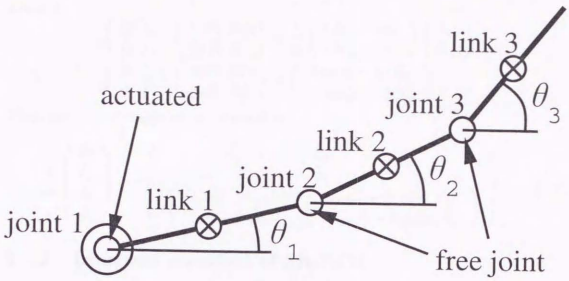

Figure 6.1: 3R free-joint manipulator

Consider a 3R free-joint manipulator whose first joint is only actuated and others are free as shown in Fig. 6.1. Assume that the manipulator resides in the horizontal plane. The dynamics is given by

$$\begin{pmatrix} A_1 & B_{21}c_{21} & B_{31}c_{31} \\ B_{21}c_{21} & A_2 & B_{32}c_{32} \\ B_{31}c_{31} & B_{32}c_{32} & A_3 \end{pmatrix} \begin{pmatrix} \ddot{\theta}_1 \\ \ddot{\theta}_2 \\ \ddot{\theta}_3 \end{pmatrix} + \begin{pmatrix} -B_{21}s_{21}\dot{\theta}_2^2 - B_{31}s_{31}\dot{\theta}_3^2 \\ B_{21}s_{21}\dot{\theta}_1^2 - B_{32}s_{32}\dot{\theta}_3^2 \\ B_{31}s_{31}\dot{\theta}_1^2 + B_{32}s_{32}\dot{\theta}_2^2 \end{pmatrix} = \begin{pmatrix} \tau \\ 0 \\ 0 \end{pmatrix} \quad (6.1)$$

where θ_i is defined as the absolute angle for simplification of the equation. With the periodic input to the first joint such as $\theta_1 = \theta_{10} + \varepsilon f_T(t)$ and the substitution as $(\dot{\theta}_2, \dot{\theta}_3) = (\varepsilon p_2, \varepsilon p_3)$, Eq.(6.1) yields

$$\begin{pmatrix} \dot{p}_2 \\ \dot{p}_3 \end{pmatrix} = \frac{1}{\Delta} \begin{pmatrix} \tilde{A}_3 & -c_{32} \\ -c_{32} & \tilde{A}_2 \end{pmatrix} \cdot \begin{pmatrix} -\tilde{c}_{21} f_T'' + \varepsilon \left(s_{32} {p_3}^2 - \tilde{s}_{21} f_T'^2 \right) \\ -\tilde{c}_{31} f_T'' - \varepsilon \left(s_{32} {p_2}^2 + \tilde{s}_{31} f_T'^2 \right) \end{pmatrix} \quad (6.2)$$

The standard form for Eq.(6.2) is given by

$$\begin{aligned} \begin{pmatrix} \dot{\theta}_2 \\ \dot{\theta}_3 \end{pmatrix} &= \varepsilon \left\{ \begin{pmatrix} \phi_2 \\ \phi_3 \end{pmatrix} - \begin{pmatrix} \zeta_2 \\ \zeta_3 \end{pmatrix} f_T' \right\} \\ \begin{pmatrix} \dot{\phi}_2 \\ \dot{\phi}_3 \end{pmatrix} &= \varepsilon \frac{1}{\Delta} \begin{pmatrix} \tilde{A}_3 & -c_{32} \\ -c_{32} & \tilde{A}_2 \end{pmatrix} \cdot \left\{ \begin{pmatrix} s_{32} {\phi_3}^2 \\ -s_{32} {\phi_2}^2 \end{pmatrix} + \begin{pmatrix} g_2 \\ g_3 \end{pmatrix} {f_T'}^2 \right. \\ &\quad \left. + \begin{pmatrix} -(s_{32}\zeta_3 + \tilde{s}_{21})\phi_2 - s_{32}\zeta_3\phi_3 \\ (s_{32}\zeta_2 - \tilde{s}_{31})\phi_3 + s_{32}\zeta_2\phi_2 \end{pmatrix} f_T' \right\} \end{aligned} \quad (6.3)$$

where

$$\begin{pmatrix} \zeta_2 \\ \zeta_3 \end{pmatrix} = \begin{pmatrix} \zeta_2(\theta_2, \theta_3) \\ \zeta_3(\theta_2, \theta_3) \end{pmatrix} = \frac{1}{\Delta} \begin{pmatrix} \tilde{A}_3 & -c_{32} \\ -c_{32} & \tilde{A}_2 \end{pmatrix} \begin{pmatrix} \tilde{c}_{21} \\ \tilde{c}_{31} \end{pmatrix}$$
$$\begin{pmatrix} g_2 \\ g_3 \end{pmatrix} = \begin{pmatrix} g_2(\theta_2, \theta_3) \\ g_3(\theta_2, \theta_3) \end{pmatrix} = \begin{pmatrix} (s_{32}\zeta_3 + \tilde{s}_{21})\zeta_2 \\ -(s_{32}\zeta_2 - \tilde{s}_{31})\zeta_3 \end{pmatrix}$$

Then the averaged system is obtained as

$$\frac{d}{dt} \begin{pmatrix} \bar{\theta}_2 \\ \bar{\theta}_3 \\ \bar{\phi}_2 \\ \bar{\phi}_3 \end{pmatrix} = \varepsilon \begin{pmatrix} \bar{\phi}_2 \\ \bar{\phi}_3 \\ \dfrac{1}{\Delta} \begin{pmatrix} \tilde{A}_3 & -c_{32} \\ -c_{32} & \tilde{A}_2 \end{pmatrix} \cdot \begin{pmatrix} s_{32}\bar{\phi}_3^2 + Kg_2(\bar{\theta}_2, \bar{\theta}_3) \\ -s_{32}\bar{\phi}_2^2 + Kg_3(\bar{\theta}_2, \bar{\theta}_3) \end{pmatrix} \end{pmatrix} \tag{6.4}$$

6.2.2 Invariant manifold of 3R-FJM

The phase space of the 3R free-joint manipulator is six-dimensional and its Poincaré map being cut at the period of the first joint is four-dimensional, that is, $(\theta_2, \theta_3, \dot{\theta}_2, \dot{\theta}_3)$. Figures 6.2 through 6.4 illustrate the behavior of the 3R free-joint manipulator in response to a periodic input, $f_T = 1 - \cos \omega t$ with the amplitude $\varepsilon = 0.01$ and the frequency $\omega = 2\pi$. The dynamic parameters of the manipulator for simulations were determined symmetrically as $m_i = 1.0$, $l_i = 0.2$, $l_{ci} = 0.1$ and $I_i = \dfrac{1}{12} m_i {l_i}^2$. The initial configuration is given by $(\theta_2, \theta_3) = (1.0, 1.0)$[rad]. Figures 6.2 through 6.4 are the Poincaré map projected onto the 3-dimensional space of $(\theta_2, \theta_3, \dot{\theta}_3)$, the phase plane of the third joint, and the plane of the second and third joints, respectively. The dots denote Poincaré sections with the period T. The empty circles denote the 'second' Poincaré sections of the 'first' Poincaré map cut at $\dot{\theta}_2 = 0$. In Fig. 6.2, the projection of the first Poincaré map onto the 3D space of $(\theta_2, \theta_3, \dot{\theta}_3)$ formed a closed surface with a hole in the center. In Fig. 6.3, the projection onto the 3rd joint's phase plane became an ellipse-like shape. In Fig. 6.4, the projection onto the 2nd and 3rd joints' plane took a shape like a rectangle.

Although it is difficult to see the shape in the whole 4-dimensional phase space of $(\theta_2, \theta_3, \dot{\theta}_2, \dot{\theta}_3)$, it can be concluded from the figures that it forms an two-dimensional invariant manifold like a two-dimensional torus in the 4D phase space. The reason why the manifold is two dimensional is as follows: The second Poincaré map forms a pair of closed curves, as seen from Figs. 6.2 and 6.3. The curves are only one dimensional, since their projections were one-dimensional in each figure. The curves intersected the plane of $\dot{\theta}_2 = \dot{\theta}_3 = 0$ at four points. The points located in the corners of the rectangle in the plane of (θ_2, θ_3) in Fig. 6.4. Since a point is zero-dimensional, the invariant manifold is two-dimensional at the most.

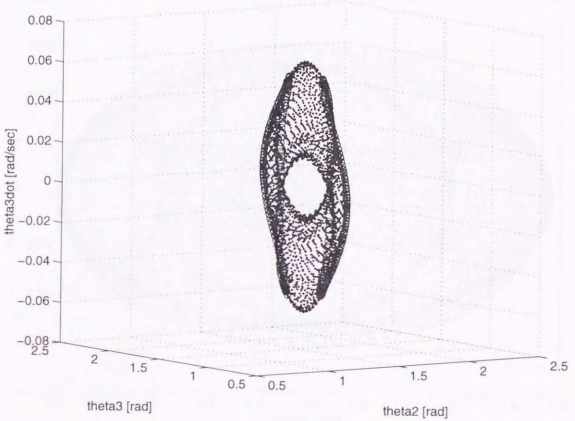

Figure 6.2: Poincaré map projected onto 3D space $(\theta_2, \theta_3, \dot{\theta}_3)$

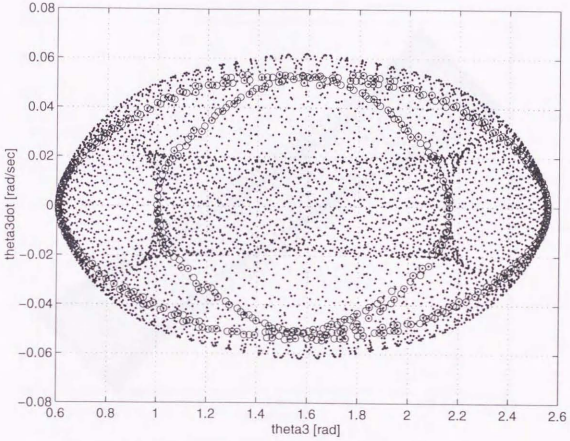

Figure 6.3: Poincaré map projected onto 3rd joint's phase plane

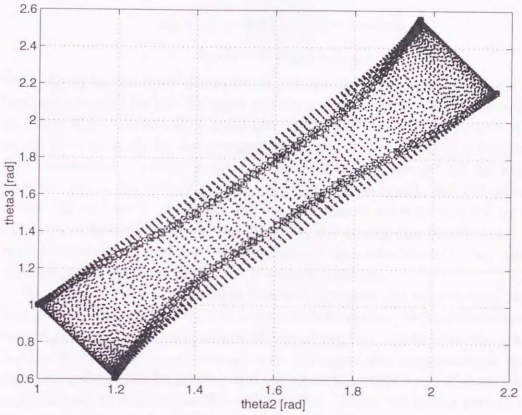

Figure 6.4: Behavior of 3R-FJM in 2nd and 3rd joints' plane

6.2.3 Conserved quantities of 3R-FJM

As in the previous subsection, a conserved energy-like quantity can be found for the averaged 3R-FJM. The conservation restricts the trajectory within a subspace with a reduced dimension, namely, three or less. One of conserved quantities can be obtained from the averaged Lagrangian similarly to the discussion in Sec.5.4.2. The conserved energy-like quantity is represented by

$$E(\bar{\boldsymbol{\theta}}, \bar{\boldsymbol{\phi}}) = E_k(\bar{\boldsymbol{\theta}}, \bar{\boldsymbol{\phi}}) + E_p(\bar{\boldsymbol{\theta}}) \tag{6.5}$$

where E_k and E_p denote the kinetic and potential components, respectively, as

$$E_k(\bar{\boldsymbol{\theta}}, \bar{\boldsymbol{\phi}}) = \tilde{A}_2\bar{\phi}_2^2 + \tilde{A}_3\bar{\phi}_3^2 + 2\tilde{c}_{32}\bar{\phi}_2\bar{\phi}_3$$

$$E_p(\bar{\boldsymbol{\phi}}) = K\,(\tilde{c}_{21}\zeta_2 + \tilde{c}_{31}\zeta_3)$$

From Eq.(6.4), the time derivative of the kinetic component E_k yields $\dot{E}_k = 2\varepsilon K(g_2\phi_2 + g_3\phi_3)$ for the averaged system and that of the potential component E_p yields $\dot{E}_p = -2\varepsilon K(g_2\phi_2 + g_3\phi_3)$ and, therefore, $\dot{E} = 0$ and E is proved to be a conserved quantity for the averaged dynamics. The quantity is a Hamiltonian for the averaged dynamics and we simply call it the "energy" for 3R free-joint manipulators in the followings. The above simulation maintained the value of E at 19.7568[rad^2/sec^2]. Although the conservation is never proved for the original non-averaged dynamics of the 3R-FJM, the energy can be concluded to be approximately conserved for the non-averaged dynamics from the fact that the approximation is guaranteed by the averaging theorems.

As stated above, each invariant manifold intersects the velocity-zero plane at four isolated points. Namely, the system stabilized onto the two-dimensional invariant manifold can be terminated at one of the four points when the velocities exactly become zero at the Poincaré map. It implies that positioning the 3R free-joint manipulator can be divided into two phases, namely, control to an invariant manifold and termination at the desired point. Then, the former control to the invariant manifold is developed using the conserved quantity. Note that the above conservation is nothing but one-dimensional constraints in the four-dimensional phase space, while the simulations imply that the manifold is two-dimensional and, therefore, it must have another conserved quantity. However there are several methods to find the other conserved quantity in Hamiltonian analysis in nonlinear dynamics, the 3R free-joint manipulator has no cyclic coordinates in its averaged dynamics and is not a separable system. If the other conserved quantity is identified, the two conserved quantities can be controlled by modulation of the amplitude and the frequency of the input. The modulation of the input frequency alters the second-order moment K in Eq.(6.4) independently of the input amplitude ε. Although the other conserved quantity has not been found yet, a control that restricts

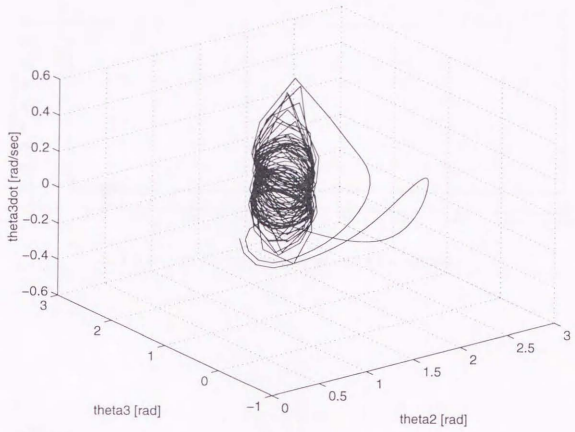

Figure 6.5: Poincaré trajectory of the averaged 3R-FJM under the control

to at most three-dimensional space can be applied and, subsequently, a feedback law that restricts to the desired manifold will be developed by the other conservation. A feedback control by the conserved quantity is proposed in the next subsection.

6.2.4 Feedback control by the conserved quantity

The isolated velocity-zero points of the invariant manifold can be moved by modulation of the input amplitude since they are determined by $\boldsymbol{\phi} = \frac{\dot{q}}{\tilde{c}}$ and not by $\dot{q}$. Therefore, the proposed method of Eq.(5.29) were applied to the 3R free-joint manipulator.

Figure 6.5 shows a simulation result of the averaged 3R free-joint manipulator under the proposed control method. The figure is represented by a connected Poincaré map projected onto a 3-dimensional phase plane of $(\theta_2, \theta_3, \dot{\theta}_3)$. The initial

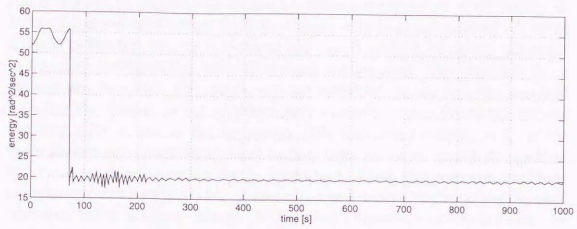

Figure 6.6: Energy transitions under the control

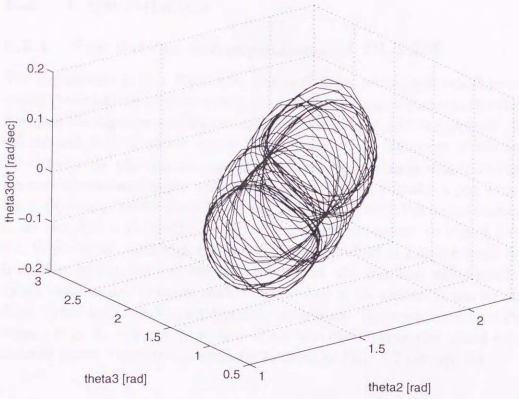

Figure 6.7: Poincaré trajectory after $t = 300$[sec]

and desired configurations are $(\theta_2, \theta_3, \dot{\theta}_2, \dot{\theta}_3)$=(0.5[rad], 0.5[rad], 0[rad/sec], 0[rad/sec]) and $(1.0, 1.0, 0, 0)$, respectively. Figure 6.6 shows the transitions of the energy E. Figure 6.7 shows the Poincaré trajectory from $t = 300$[sec] to $t = 1000$[sec], which is a part of Fig. 6.5. Thanks to the proposed control method, the energy converges to the value corresponding with the desired configuration. The trajectory is on an invariant manifold. The system was not stabilized exactly onto the manifold including the destination but stabilized onto a manifold where the energy became the same value as that at the destination. The stabilized trajectory in the phase space forms a two dimensional closed surface, since the input amplitude is settled in a constant value when the energy is constant. Then, the proposed amplitude modulation control stabilizes the system onto a two-dimensional invariant manifold corresponding to a desired energy. If the other conserved quantity is found, the stabilized manifold is identified and the system can be stabilized onto a manifold which passes through a desired point. In addition, simulations were carried out for the exact non-averaged system which showed similar results as those for the averaged system.

6.3 Experiments

6.3.1 Simulations for experimental 3R-FJM

The simulations in Sec. 6.2.2 were executed for a provisional model in order to clarify the behaviors of 3R free-joint manipulators. Thus, simulations for the model based on the experimental 3R free-joint manipulator should be executed. Figures 6.8 through 6.10 illustrate a simulation result of the behaviors of the averaged 3R-FJM for the experimental model in response to a periodic input. The dynamic parameters conform to the values in Table 5.1. The periodic input is as: $\theta_1 = \theta_{10} + \varepsilon(1 - \cos\omega t)$ with $\varepsilon = 0.1$[rad] and $\omega = 4\pi$[rad/sec]. The initial configuration is as: $(\theta_{20}, \theta_{30}) = (1.0\text{[rad]}, 1.0\text{[rad]})$. The figures correspond to Figs. 6.2 through 6.4, respectively. Although the shape of the manifold in Fig. 6.8 looks different from that in Fig. 6.2 and has a twisted form, the manifold still formed a two-dimensional torus-like closed surface with a hall in the center. It can be said that these torus-like manifold is topologically equivalent. The second and third Poincaré maps cut at $\dot{\theta}_2 = 0$ and $\ddot{\theta}_2 = \dot{\theta}_3 = 0$ are also one-dimensional closed curve and isolated points, respectively, similarly to those in Figs. 6.2 through 6.4.

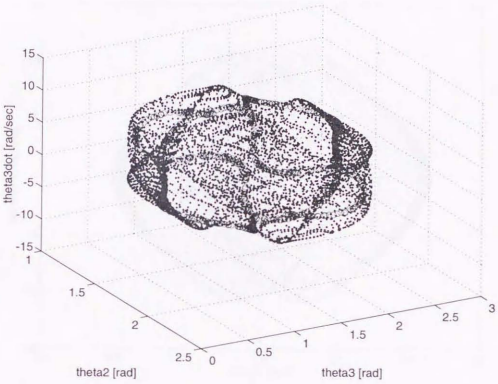

Figure 6.8: Poincaré map projected onto 3D space $(\theta_2, \theta_3, \dot{\theta}_3)$
Simulation for experimental 3R-FJM: $(\theta_{20}, \theta_{30}) = (1.0[\text{rad}], 1.0[\text{rad}])$

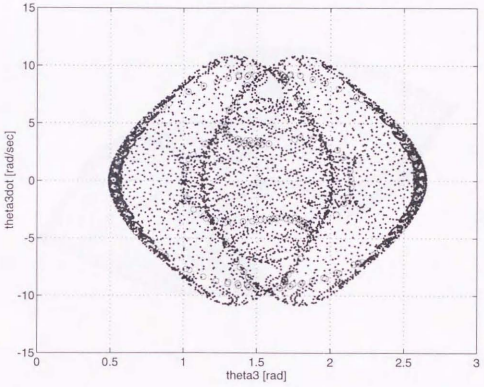

Figure 6.9: Poincaré map projected onto 3rd joint's phase plane
Simulation for experimental 3R-FJM: $(\theta_{20}, \theta_{30}) = (1.0[\text{rad}], 1.0[\text{rad}])$

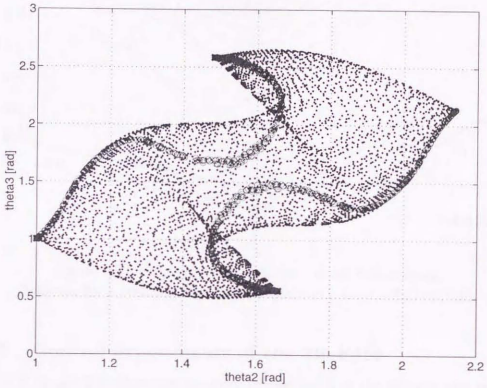

Figure 6.10: Behavior of 3R-FJM in 2nd and 3rd joints' plane
Simulation for experimental 3R-FJM: $(\theta_{20}, \theta_{30}) = (1.0[\text{rad}], 1.0[\text{rad}])$

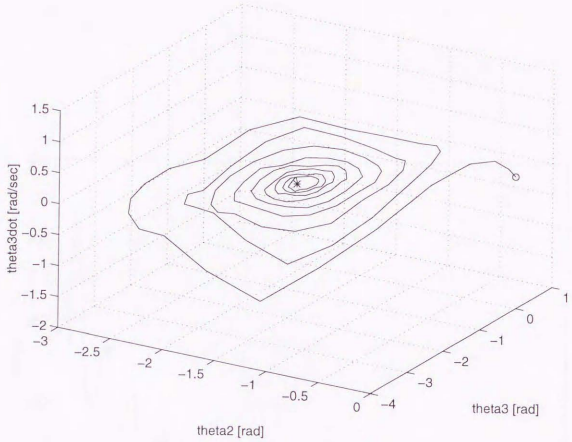

Figure 6.11: Experimental trajectory in 3D phase space
Behavior for a constant input amplitude $\varepsilon = 0.1$: $(\theta_{20}, \theta_{30}) = (0, 0)$

6.3.2 Control experiments of the 3R-FJM

Figures 6.11 and 6.12 illustrate an experimental result of the 3R free-joint manipulator in response to a periodic actuation with a constant input-amplitude. The periodic input is as: $\theta_1 = \theta_{10} + \varepsilon(1 - \cos\omega t)$ with $\varepsilon = 0.1$[rad] and $\omega = 4\pi$[rad/sec]. The initial configuration is $\theta_2 = \theta_3 = 0$[rad]. Figure 6.11 represents the trajectory in 3D phase space of θ_2, θ_3 and $\dot{\theta}_3$. Solid line in the figure denotes a connected curve of Poincaré map, and an empty circle and an asterisk denotes the initial point and the final point, respectively. Figure 6.12 represents the transition of the energy E. The system showed a swirl-like trajectory drawn into the center point $(\theta_2, \theta_3) = \left(\frac{\pi}{2}, \frac{\pi}{2}\right)$. Note that since θ_i was defined as a absolute angle, the third joint becomes straight relatively to the second link at the center point. The energy fluctuated and converged to zero similarly to that of the 2R free-joint manipulator.

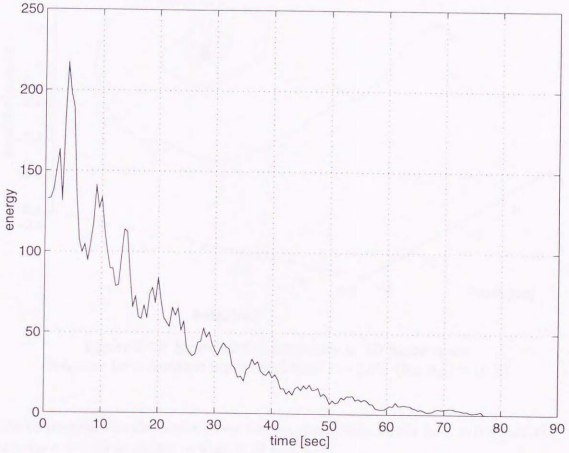

Figure 6.12: Experimental energy transition
Behavior for a constant input amplitude $\varepsilon = 0.1$: $(\theta_{20}, \theta_{30}) = (0, 0)$

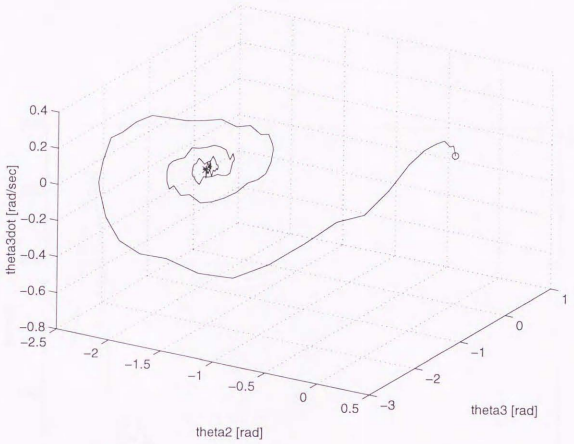

Figure 6.13: Experimental trajectory in 3D phase space
Behavior for a constant input amplitude $\varepsilon = 0.05$: $(\theta_{20}, \theta_{30}) = (0, 0)$

The convergence to the center point was comparatively slower for $\varepsilon = 0.1$ than the case for $\varepsilon = 0.05$ as shown in Figs. 6.13 and 6.14.

Figures 6.15 through 6.17 illustrate an experimental result of stabilization of the energy by the amplitude modulation. The initial point was about $(\theta_2, \theta_3) \simeq (30[\text{deg}], 0)$ and the desired energy corresponded with $(\theta_2, \theta_3) = (60[\text{deg}], 0)$. Although the control failed as a result from a viewpoint of positioning, it made efforts to stabilize the energy which can be seen in Fig. 6.17 compared to Fig. 6.12 and the system was converged not to the center point but to a small manifold. Although of course frictional term was quite large to disturb the stabilization of the energy, it should be noted the periodical errors of the energy by inaccuracy to take Poincaré map. If the error of Poincaré map is fixed in future researches, the control might show better results.

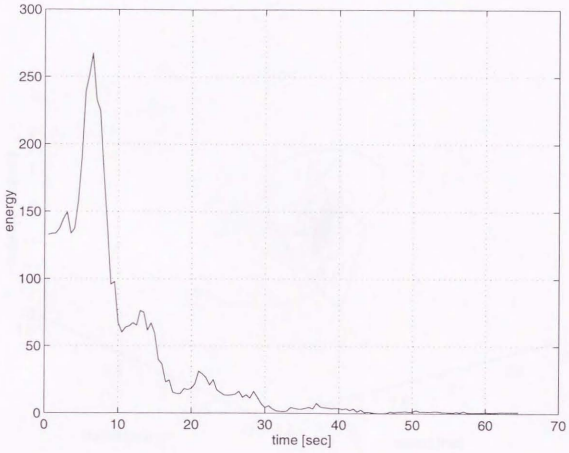

Figure 6.14: Experimental energy transition
Behavior for a constant input amplitude $\varepsilon = 0.05$: $(\theta_{20}, \theta_{30}) = (0, 0)$

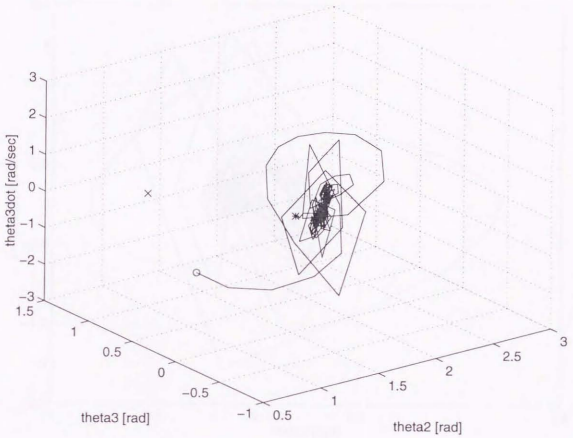

Figure 6.15: Exp.5-5: Trajectory in 3D phase space

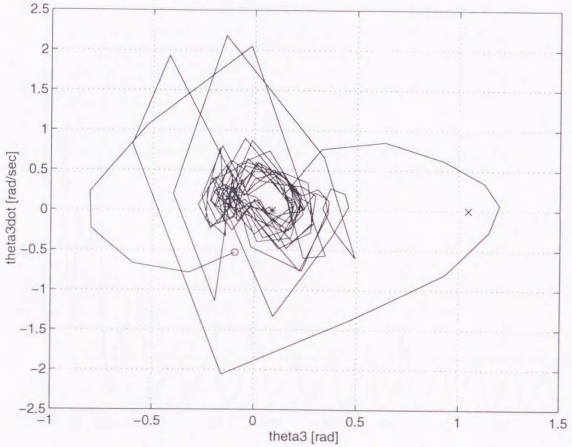

Figure 6.16: Exp.5-5: Trajectory in phase plane of the third joint

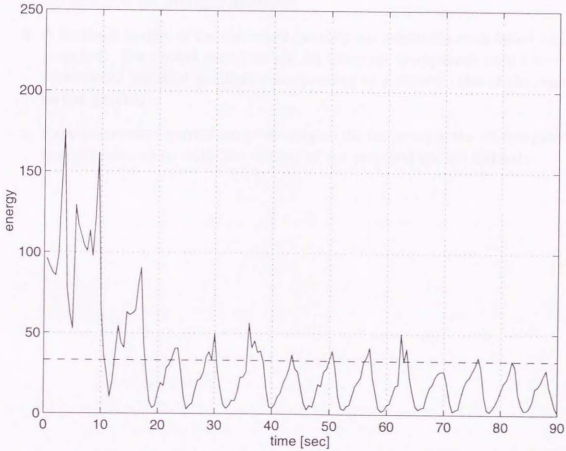

Figure 6.17: Exp.5-5: Energy transition

6.4 Conclusion

The results in this chapter are as follows:

1. For 3R free-joint manipulators, invariant manifolds of the averaged dynamics were shown to be two-dimensional torus-like closed surface from simulations, where identification of the manifold requires two conserved quantities.

2. A conserved quantity was identified as a Hamiltonian from consideration of the energy of the averaged dynamics.

3. A feedback control of the conserved quantity via amplitude modulation was proposed. The control stabilized the 3R free-joint manipulator onto a two-dimensional invariant manifold corresponding to a desired value of the conserved quantity.

4. Experiments were carried out to investigate the behaviors of the 3R free-joint manipulator and to verify the validity of the proposed control method.

Chapter 7

Conclusion

7.1 Contributions

This thesis discussed dynamical features of nonholonomic mechanical systems and control of underactuated systems. The main results are summarized as follows:

1. In Chap.3, a motion planning of free-flying space robots was discussed as a first-order nonholonomic problem under dynamical constraints.

   (a) Nonholonomic motions of space robots were formulated with Euler parameters. The variation of satellite orientations was represented by Lie brackets for a cyclic motion and constant coefficient vectors. The constant coefficient vectors imply the radius of cyclic motion.

   (b) A motion planning method for space robots was proposed. The method simplifies path planning by dividing it into two steps:

      i. Holonomic planning of a nominal motion disregarding the nonholonomic constraints.

      ii. Computation of a feasible motion approximating the infeasible nominal motion by spiral-like motion around it.

   This strategy enables to apply many conventional path-planning methods developed for holonomic robots to nonholonomic motion planning.

2. In Chap.4, nonlinear behaviors of free-joint manipulators were analyzed and its control was discussed as a second-order nonholonomic problem.

   (a) Nonlinear behaviors of 2R free-joint manipulators with a periodic input were investigated by computer simulations. For a sufficiently small input-amplitude, the Poincaré map of the trajectory forms an ellipse-like closed curve in the phase space. Chaotic behaviors of 2R free-joint manipulators for a larger input amplitude were clarified.

(b) A control strategy of free-joint manipulators with a periodic input was proposed. The control strategy was composed of two subgoals:

i. Simple positioning of the actuated joint to its destination regardless of free joints, which can be easily achieved.

ii. Control of the free joints by periodic actuation of the actuated joint.

Control to an invariant manifold passing through the destination and termination control at the destination were proposed to meet the second subgoal. Composition of these two controls was heuristically established for 2R manipulators with one motor and a free joint.

3. In Chap.5, the averaging method was applied to formulate a theoretical investigation of the behaviors of 2R free-joint manipulators. Control methods were developed via averaging analyses.

   (a) The averaged dynamics of 2R free-joint manipulators was found to form an invariant manifold. The invariant manifold was characterized by a Hamiltonian conservation.

   (b) Control methods to a desired invariant manifold using the Hamiltonian via amplitude modulation were proposed.

   (c) Second-order averaging analysis was investigated to obtain a better approximation and to develop a control to terminate at the destination.

   (d) Experiments were carried out to verify the effectiveness of the proposed control methods.

4. In Chap.6, the averaging analysis adopted in Chap.5 was extended to 3R free-joint manipulators.

   (a) The averaged dynamics of 3R free-joint manipulators was found to form a two dimensional torus-like invariant manifold in the four dimensional phase space, which implies the existence of two conserved quantities. One of conserved quantities was found to be a Hamiltonian of the averaged dynamics.

   (b) A control via amplitude modulation was applied to 3R free-joint manipulators to stabilize its 'energy.' The control stabilized it to a two dimensional manifold corresponding the energy.

   (c) Experiments were executed to show the nonlinear behaviors of 3R free-joint manipulators and verify the proposed control.

This research showed general nonlinear features of robot dynamics and its potentiality to minimize robot mechanisms in exchange for difficulty to control under nonholonomy. New advantageous minimal mechanisms were proposed as free-joint manipulators with only one motor through the above studies on control of nonholonomic robots. Although several systems were proposed as minimal systems by other researchers [AHLM95, Lyn96, BG+96], they utilized other circumstantial forces of a conveyor, friction, or gravity as extra actuators or geometric constraints. The mechanisms proposed here without circumstantial forces are definitely discriminated from those in the existence of such extra forces.

Several analysis and control concepts introduced in this dissertation can be generalized to other nonholonomic systems, e.g. higher-dimensional or more complex systems. Especially, theories and methods for chaotic systems were found to be powerful and useful tool to analyze dynamical nonlinear mechanisms.

7.2 Prospects

There are left lots of open problems:

1. Stability of free-joint manipulators was never shown in a strict sense.
2. Positioning control method was developed only for 2R free-joint manipulators.
3. Characterization of manifolds of higher dimensional systems is still difficult.
4. Input parameters to be modulated are only the amplitude and the frequency, where higher dimensional systems will require more parameters to be controlled.
5. The averaging analysis was based on friction-free systems, where there is very few practical systems with no friction in a strict sense.

Although exact proof of controllability of free-joint manipulators was never presented, composition of global attraction to a manifold and termination at a destination on the manifold possibly implies a constructive way to find a trajectory connecting any initial point to any destination via a manifold. The problems are that the control methods proposed in this dissertation were based upon an approximation and that the stabilizability is still quite difficult to be shown.

When friction is taken into account, the system will be not conserved as in Chap.5 but dissipative. Dynamical analysis and modeling of the manifold will be difficult since the dynamical structure turns into quite different. However, appropriate control may allow to deal with a system as friction-less as in the experiments

in Sec.5.7. The works on control of free-joint manipulators with friction has currently been done.